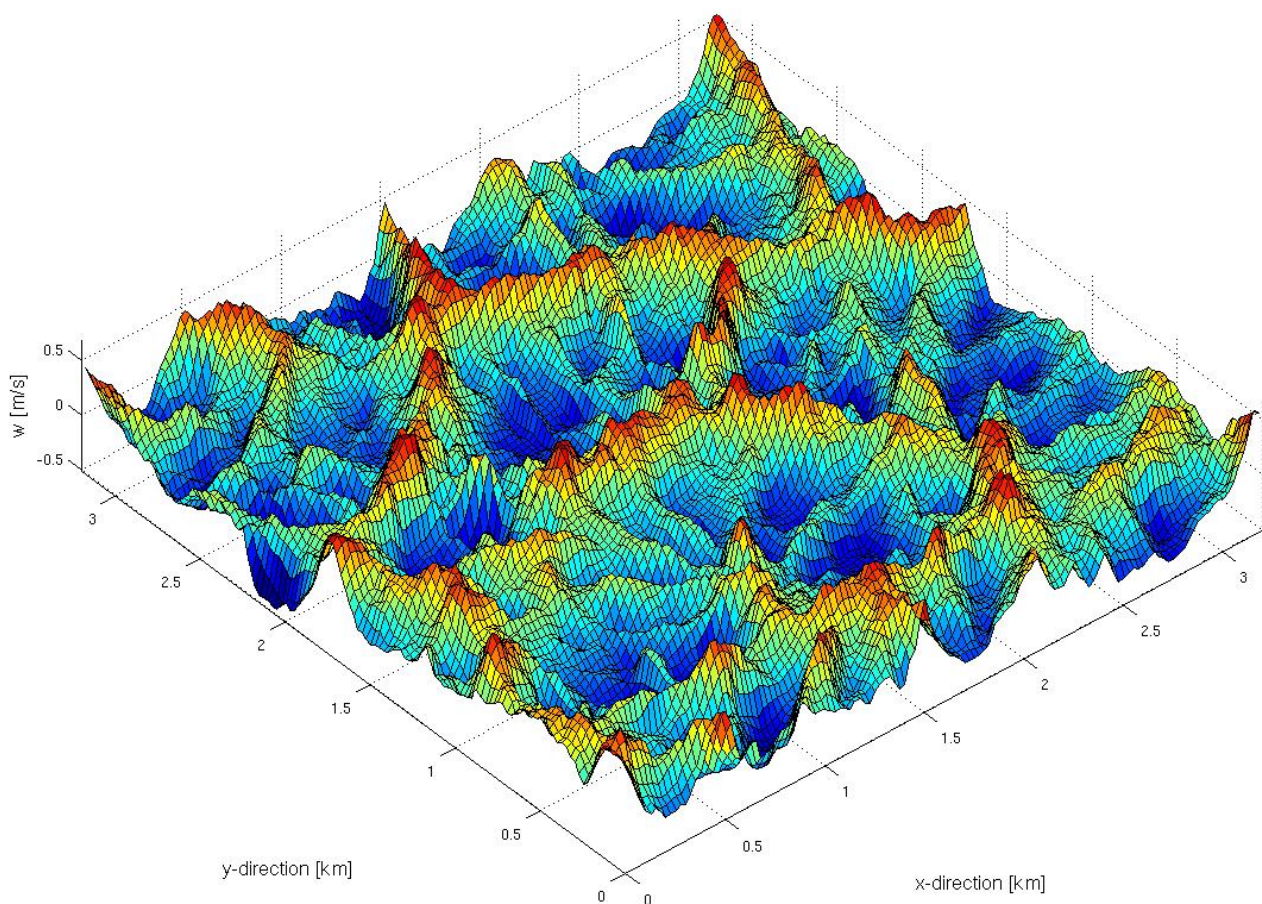# Study of the Flux Imbalance Problem in Cabauw Tower Observations

Master thesis

Huug Ouwersloot

Mean w over an hour at 100 m height

Supervisors:
Dr. F.C. Bosveld (KNMI)
Ir. P.S. Kroon
Dr. S.R. de Roode

30th September 2009

TUDelft
Delft University of Technology

Clouds, Climate and Air Quality
Department of Multi-Scale Physics
Faculty of Applied Sciences

Challenge the future

The figure at the cover page represents the vertical wind velocities averaged over an hour at a height of 100 m. Data is collected from Large Eddy Simulations of the BOMEX case performed by Steven de Boer. The horizontal domain has a size of 3.2 km x 3.2 km and consists of 128 x 128 grid boxes. The resolution of the performed simulation is 25 m in the horizontal directions and 40 m in the vertical direction. The prescribed surface buoyancy flux is 21 W m^{-2} and the horizontal wind velocity is near 0 m s^{-1}. Wind velocities are sampled every minute.

Study of the Flux Imbalance Problem in Cabauw Tower Observations

H.G. Ouwersloot BSc.

Master thesis

Supervisors:
Dr. F.C. Bosveld
Ir. P.S. Kroon
Dr. S.R. de Roode

Clouds, Climate and Air Quality
Department of Multi-Scale Physics
Faculty of Applied Sciences
Delft University of Technology

30th September 2009

Abstract

Emissions of heat and greenhouse gases from the earth's surface are often quantified by measuring their vertical turbulent fluxes just above the earth's surface using the Eddy Covariance technique. These observations are performed at one fixed position. This technique uses the assumption that the mean vertical wind velocity for sufficiently long time scales (10 minutes or longer) is 0 m s^{-1}. However, research using Large Eddy Simulations has shown that this assumption is generally not valid. This causes a systematic bias in the measured fluxes. On average the absolute value of the measured flux will be too low. The ratio of the emission that is not measured versus the total emission is called the flux imbalance. The magnitude of this effect is dependent on the height. The effects at a height of about 3 m are negligible, but at heights of 60 m or higher the flux imbalance can be of the order of 20 % in extreme cases.

In this thesis, high frequency observations collected from the 200 m tall tower at Cabauw are analysed to assess the impact of the flux imbalance problem. In addition to a typical measurement height of 3 m, data at 60 m, 100 m and 180 m height is examined as well.

In order to determine the total flux, the wind velocities have to be determined precisely. First of all, a wind tilt correction algorithm is applied to account for a possible tilt in the sonic anemometer and wind distortion due to measurement equipment. It is concluded that the wind tilt correction should be calculated based on data obtained over a year. The reason is that the wind tilt correction based on data obtained over a month is not accurate, since it varies from month to month.

A flux imbalance effect is theoretically derived using the assumption of periodic scalar concentration and vertical wind velocity profiles. Also the temporal averaged vertical wind velocity in observations is investigated. Even over a month, it is not equal to 0 m s^{-1}. This implies that a flux imbalance effect is present. Furthermore, it is determined that the standard deviation of temporal averaged vertical wind velocities over a long time is of the order of tenths m s^{-1}. The standard deviation decreases with averaging time and increases with height. At 3 m height, the spread is relatively small compared to the greater heights. This behaviour indicates that the same effects are present in nature as Large Eddy Simulations predict.

Since the temporal averaged vertical wind velocities at 3 m height are small, observations performed at that height do not have to be corrected for the flux imbalance. However, Eddy Covariance fluxes measured at heights of about 60 m or higher should be corrected.

The imbalance error in Eddy Covariance measurements can be minimized by using long enough averaging times. It is found that at 3m height measurements over 10 minutes are adequate. Above 60 m height, measurements should be performed over at least 30 minutes, but an hour would give noticeable better results. However, one should take into account that over longer periods the situation is not stationary anymore.

Contents

CONTENTS

List of Figures

LIST OF FIGURES

List of Tables

LIST OF TABLES

x

Chapter 1

Introduction

From the earth's surface, heat and scalars, like concentrations of the greenhouse gases carbon dioxide, methane and nitrous oxide, are emitted into the lower layer of the atmosphere. This layer is called the atmospheric boundary layer and is the part of the troposphere that is directly influenced by the presence of the earth's surface (Stull, 1988). In the boundary layer, energy and particles are transported by swirls of air, called eddies. The largest eddies are as high as the boundary layer; the smallest have a size of a few millimeter. Knowing the actual emission values for different types of landscape is very important for society, since based on this, policy can be made to make sure that the emissions of greenhouse gases remain limited to acceptable levels. This is necessary to limit the greenhouse effect.

Since the emitted quantities are transported through the boundary layer, the emissions can be determined by measuring the fluxes through the air. In order to measure the turbulent fluxes of scalars, temperature and momentum from the earth's surface to the atmosphere, the Eddy Covariance (EC) technique is used often. This EC technique involves measuring both the emitted quantity and the vertical wind velocity at high frequency. The temperature and wind velocities are typically measured with a sonic anemometer. Measurements at the humidity and CO_2 concentration are performed with a LICOR CO_2/H_2O gas analyzer. A big advantage of this technology is its temporal coverage. Under the assumption of homogeneous surface conditions it also has a high spatial resolution.

Unfortunately, according to recent Large Eddy Simulations (LES) studies, (Kanda et al., 2004; Steinfeld et al., 2007; Huang et al., 2008; Schalkwijk, 2008), which are high resolution numerical turbulence models, the Eddy Covariance technique does not measure the complete flux because of a systematic bias. This occurs if locally there is on average a non-zero vertical wind velocity during the measurement. On average the flux measured will be less than the actual emission. This effect is called the flux imbalance (Kanda et al., 2004). So far, the flux imbalance is only shown in simulations and not yet for observations. In this thesis the importance of the imbalance problem in the calculation of the turbulent fluxes from high frequency field observations is investigated. This is done for several measuring heights, ranging from 3 m to 180 m.

First, the theory behind the flux imbalance and LES results concerning the flux imbalance are examined. A summary is given in Chapter 2. After that, the observations are processed. These are discussed in Chapter 3. In the first part, the wind tilt effects and corrections for those are treated. The behaviour of the vertical wind velocities in observations is discussed thereafter. Finally, time scales are calculated. The time scales are indications for the measurement time needed to determine representative Eddy Covariance fluxes. Also these are calculated both at low height (3m) and at 60 m height and higher. The results are summa-

rized in Chapter 4.

Chapter 2

Theory

It is often assumed that the mean vertical wind velocity over a sufficiently long time interval (10 minutes or longer) is equal to 0 m s^{-1}. In this research the error in the measured vertical flux due to this assumption is studied. Fluxes express the transport of quantities in the air. The general explanation about turbulent transport in the air is given in Paragraph 2.1. Information about spatial and temporal averaging and fluxes is discussed in Paragraph 2.2. The theory of the imbalance is explained in Paragraph 2.4. In Paragraph 2.4.3 the differences between the simulations and the measurements are explained.

2.1 Turbulent transport

The boundary layer is the part of the atmosphere that is directly influenced by the presence of the earth's surface and responds to surface forcings with a time scale of about an hour or less (Stull, 1988). The remainder of the troposphere is called the free atmosphere. The boundary layer experiences a diurnal cycle and changes in height over a day, as can be seen in Figure 2.1. Its height, called the inversion height, is typically between 100 m (at night) and 3000 m (in the afternoon). It grows by convection. Within the boundary layer transport of energy and particles occurs. Turbulence is one of the important transport processes. It mixes the air and therefore the scalars and heat in the air are mixed throughout the entire boundary layer. The turbulence consists of swirls of air, called eddies. These eddies exist in different sizes, ranging in diameter from millimeters to the height of the boundary layer, and are superimposed. In time, large eddies break down to smaller eddies. The transport by eddies is illustrated in Figure 2.2. Much of the turbulence is driven from the earth's surface. Solar heating of the earth's surface causes the neighbouring air to heat up. Because of buoyancy this results in thermals. These thermals are just large eddies. Another process generating turbulence is frictional drag on the air from the ground, which causes wind shears. In case the turbulence in the boundary layer is generated by buoyancy, it is generated convectively and the boundary layer is therefore called a convective boundary layer (CBL).

Transport is expressed in flux density, which expresses the amount of the scalar that passes per second through a plane per unit surface. The flux density is often referred to as flux. If it is assumed that the emissions and the turbulence intensity in a domain are horizontally homogeneous, a measurement at one location is representative for the whole domain. The continuity equation for an arbitrary scalar, ϕ, reads

$$\frac{\partial \phi}{\partial t} + \frac{\partial (u\phi)}{\partial x} + \frac{\partial (v\phi)}{\partial y} + \frac{\partial (w\phi)}{\partial z} = s_\phi \qquad (2.1)$$
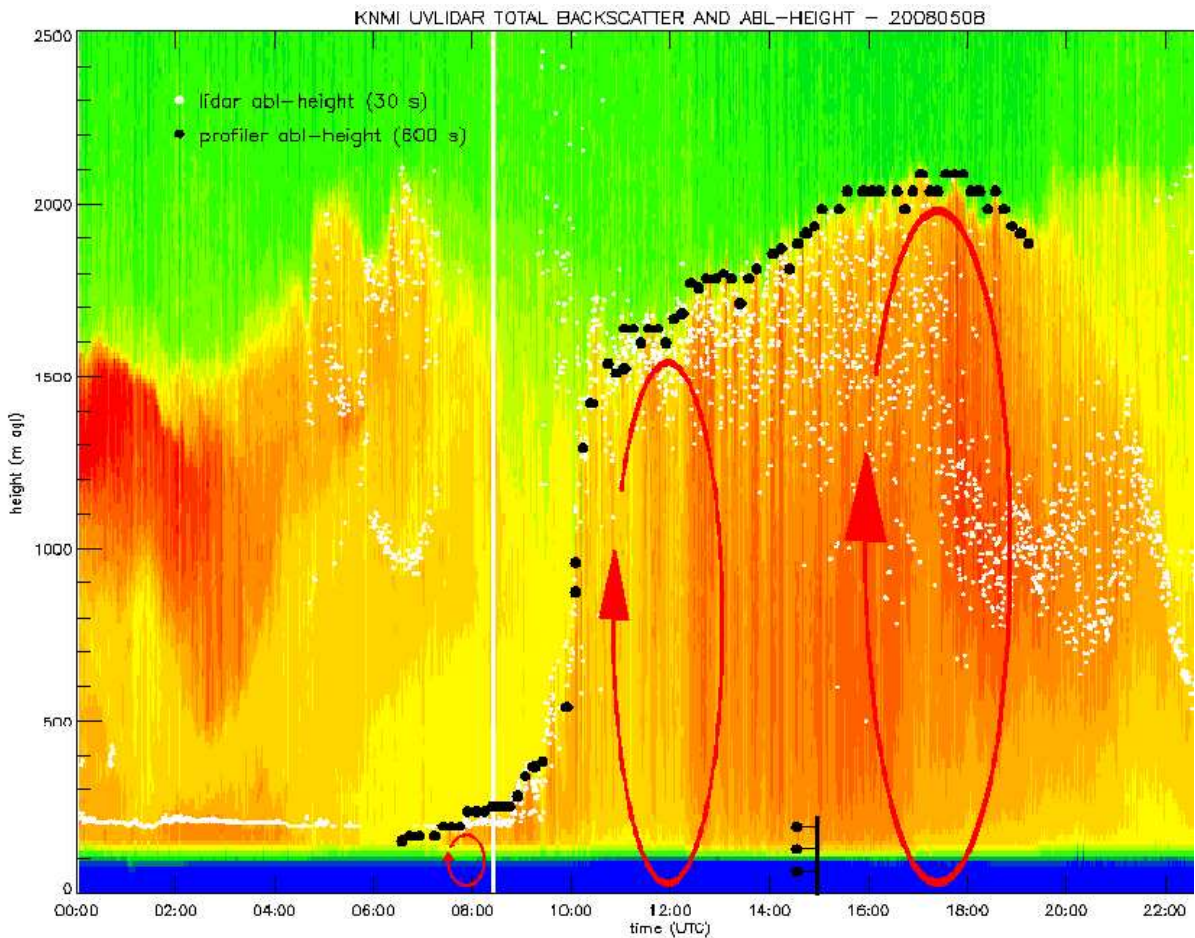
Figure 2.1: Boundary layer heights during 8 May 2008. Black dots represent boundary layer heights determined using a wind profiler. White dots represent measurements from a lidar. In the afternoon the boundary layer is capped by the free atmosphere (green colours). This figure is kindly provided by Henk Klein Baltink of the KNMI. In the figure the largest eddies that can exist are drawn. Their height is limited by the boundary layer height. A representation of the measurement tower is drawn at 15:00 h UTC.

In this equation s_ϕ is a source or sink. This can be caused by local emissions from vegetation or factories, rain, radiation or chemical reactions. If no sources or sinks are present, $s_\phi = 0$. In this thesis no sources or sinks are assumed to be present.

2.2 Fluxes

2.2.1 Averaging

If measuring over a time period and at multiple locations the average can be determined (Kanda et al., 2004; Schalkwijk, 2008; Steinfeld et al., 2007). The average in time of any
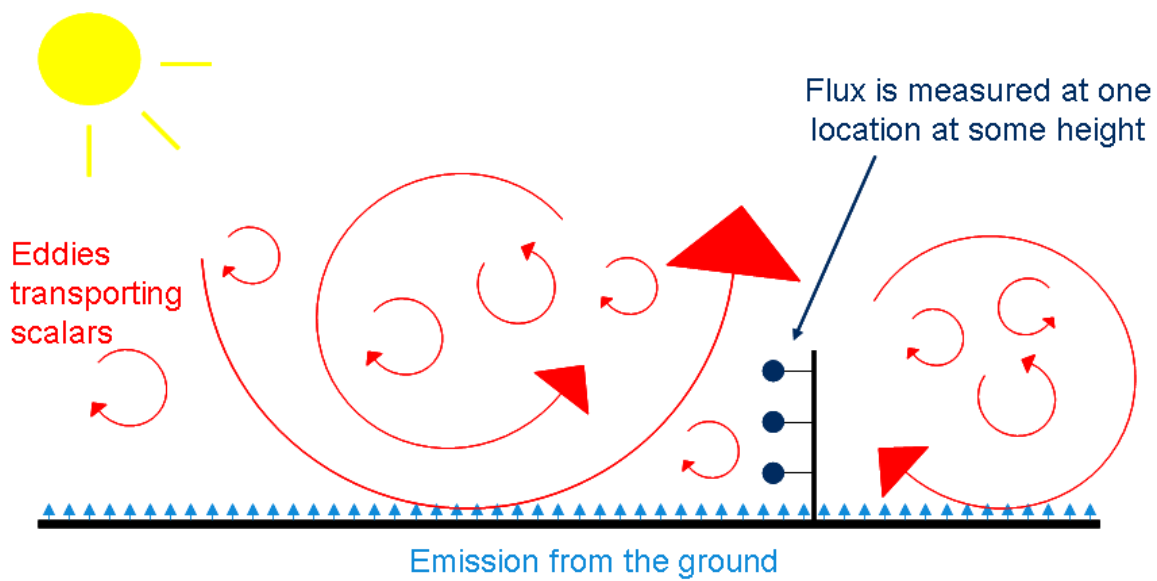
Figure 2.2: Turbulent transport in the convective boundary layer. The sun heats up the earth which in turn heats up the adjoining air. The heated air has a lower density and therefore rises. This causes the formation of eddies. The eddies transport scalars like heat and substances through the air. These include the scalars emitted by the earth's surface. At a specific point the transport is measured. When the location is representative for the whole investigated domain , the measured transport gives information about the scalar emission.

arbitrary quantity χ is given by $\overline{\chi}$, which is defined by

$$\overline{\chi}\left(x,y,z\right)=\frac{1}{T_{av}}\int_{0}^{T_{av}}\chi\left(x,y,z,t\right)\mathrm{d}t \tag{2.2}$$

in which T_{av} is the averaging time. The deviation from the temporal average is denoted as χ' which leads to

$$\chi\left(x,y,z,t\right)=\overline{\chi}\left(x,y,z\right)+\chi'\left(x,y,z,t\right) \tag{2.3}$$

and

$$\overline{\chi'\left(x,y,z,t\right)}=0 \tag{2.4}$$

In these equations x, y and z indicate the position of the scalar and t indicates the time. All four variables are independent of each other.
Similar to the temporal average, the spatial average is given by $\langle\chi\rangle$, which is defined by

$$\langle\chi\rangle\left(z,t\right)=\frac{1}{A_{av}}\iint_{0}^{A_{av}}\chi\left(x,y,z,t\right)\mathrm{d}x\mathrm{d}y \tag{2.5}$$

in which A_{av} is the averaging area. The deviation from the spatial average is denoted as χ'', so

$$\chi\left(x,y,z,t\right)=\langle\chi\rangle\left(z,t\right)+\chi''\left(x,y,z,t\right) \tag{2.6}$$

and

$$\langle \chi'' (x, y, z, t) \rangle = 0 \tag{2.7}$$

Since the horizontal positions and time are independent variables, integrals can be interchanged and

$$\overline{\langle \chi \rangle} (z) = \langle \overline{\chi} \rangle (z) \tag{2.8}$$

$$\overline{\chi''} (x, y, z) = \overline{\chi}'' (x, y, z) \tag{2.9}$$

$$\langle \chi \rangle' (z, t) = \langle \chi' \rangle (z, t) \tag{2.10}$$

$$(\chi'')' (x, y, z, t) = (\chi')'' (x, y, z, t) \tag{2.11}$$

If considering the spatial average in one dimension, the averaging area becomes the averaging length, L_{av}, and equation (2.5) becomes

$$\langle \chi \rangle_{1D} (y, z, t) = \frac{1}{L_{av}} \int_0^{L_{av}} \chi (x, y, z, t) \, \mathrm{d}x \tag{2.12}$$

2.2.2 Representations of the flux

In LES experiments, the spatial averaged flux is of interest. Assuming that no sources or sinks are present, a spatial average of equation (2.1) results in

$$\left\langle \frac{\partial \phi}{\partial t} \right\rangle + \left\langle \frac{\partial (u\phi)}{\partial x} \right\rangle + \left\langle \frac{\partial (v\phi)}{\partial y} \right\rangle + \left\langle \frac{\partial (w\phi)}{\partial z} \right\rangle = 0 \tag{2.13}$$

in which u, v, w and ϕ are functions of x, y, z and t. Because of the periodic boundary conditions, the second and third terms on the left hand side of this equation are equal to 0. When integrating from the ground to a measurement height, z, this results in

$$\int_0^z \frac{\partial \langle \phi \rangle}{\partial t} \mathrm{d}z' + \langle w\phi \rangle |_z - \langle w\phi \rangle |_0 = 0 \tag{2.14}$$

The vertical flux of a scalar at a given point and time is expressed by

$$F (x, y, z, t) = w (x, y, z, t) \, \phi (x, y, z, t) \tag{2.15}$$

Since $\langle w\phi \rangle |_0$ is the surface flux, the emission, E, is given by

$$E = \underbrace{\langle w\phi \rangle |_z}_{\text{Vertical flux}} + \underbrace{\int_0^z \frac{\partial \langle \phi \rangle}{\partial t} \mathrm{d}z'}_{\text{Storage}} \tag{2.16}$$

In this research, the vertical flux term is investigated.

It is not possible to measure the flux at many locations because of the costs, so a spatially averaged flux can not be determined from observations. Therefore measurements of the vertical flux at one location are averaged over some time. This is founded on Taylor's frozen turbulence hypothesis (Stull, 1988; Garratt, 1992). This states that turbulence might be considered to be frozen as it advects past a sensor if the turbulence intensity is small relative to the mean horizontal wind speed. In that case measurements in time can be transformed

to measurements in space. Under this condition, space, time and ensemble averages should all be equal. This is called the ergodic condition. In the Large Eddy Simulations, the periodic boundary conditions make sure that there is no mean net horizontal transport. Experimentalists assume local horizontal homogeneity and therefore they examine only vertical fluxes too. The measured emission in single location measurements is therefore equal to $\overline{w\phi}|_z + \int_0^z \frac{\Delta\phi}{\Delta t}\mathrm{d}z'$.

The temporal averaged flux, $\bar{F}$, of equation (2.15) can be represented by

$$
\begin{aligned}
\bar{F} &= \overline{(\overline{w} + w')(\overline{\phi} + \phi')} \\
&= \overline{\overline{w}\overline{\phi}} + \overline{\overline{w}\phi'} + \overline{w'\overline{\phi}} + \overline{w'\phi'} \\
&= \overline{w}\,\overline{\phi} + \overline{\overline{w}\phi'} + \overline{w'\,\overline{\phi}} + \overline{w'\phi'}
\end{aligned}
\tag{2.17}
$$

Since for every quantity, χ, it is known that $\overline{\chi'} = 0$, this results in

$$
\bar{F} = \overline{w}\,\overline{\phi} + \overline{w'\phi'}
\tag{2.18}
$$

$\overline{w}\,\overline{\phi}$ is called the vertical kinematic advective flux of ϕ and $\overline{w'\phi'}$ is called the vertical kinematic turbulent flux of ϕ.

Likewise, the spatial averaged flux, $\langle F \rangle$, can be represented by

$$
\langle F \rangle = \langle w \rangle \langle \phi \rangle + \langle w''\phi'' \rangle
\tag{2.19}
$$

The spatial average of equation (2.18) results in

$$
\langle \bar{F} \rangle = \langle \overline{w}\,\overline{\phi} \rangle + \langle \overline{w'\phi'} \rangle
\tag{2.20}
$$

and since $\langle \bar{F} \rangle = \overline{\langle F \rangle}$, the temporal average of equation (2.19) results in

$$
\langle \bar{F} \rangle = \overline{\langle w \rangle \langle \phi \rangle} + \overline{\langle w''\phi'' \rangle}
\tag{2.21}
$$

If there is no large-scale vertical motion, $\langle w \rangle = 0$, so equation (2.21) becomes

$$
\langle \bar{F} \rangle = \overline{\langle w''\phi'' \rangle}
\tag{2.22}
$$

According to equation (2.22) averaging the product of the spatial deviations of w and ϕ both spatially and temporally results in the total averaged flux. The flux that is obtained with the Eddy Covariance (EC) technique is defined as

$$
F_{\mathrm{EC}} = \overline{w'\phi'}
\tag{2.23}
$$

These fluxes are typically calculated over half an hour (Kroon et al., 2007; Vickers and Mahrt, 2003) or one hour (Huang et al., 2008). However, other durations, like 10 minutes (Bosveld, 2008 - 2009), are used as well. In Eddy Covariance measurements, it is assumed that $\overline{w} = 0$ during the period over which one flux is calculated and that therefore $\bar{F} = F_{\mathrm{EC}}$. The spatial and temporal average of the product of the temporal deviations of w and ϕ, $\langle \overline{w'\phi'} \rangle$, is the value measured by the Eddy Covariance technique averaged in space. However, according to equation (2.20), it is only equal to the total averaged flux if $\langle \overline{w}\,\overline{\phi} \rangle = 0$. Large Eddy Simulations (LES) have been performed to verify this. These are computer simulations that calculate the Navier-Stokes equations for an incompressible flow for the large turbulent scales explicitly. Scales smaller than the grid size are parameterized. Density

effects are used in the Boussinesq approximation in order to calculate the buoyancy. However, the expansion or shrinking of air parcels due to temperature changes is not taken into consideration. The LES model is based on the ideas of Lilly (1967). For more information about the LES model, the reader is referred to other literature (e.g., Nieuwstadt and Brost, 1986; Cuijpers and Duynkerke, 1993; van Zanten, 2000; Heus, 2008). The simulations used in flux imbalance research have the following boundary conditions and forcings (Kanda et al., 2004):

(1) No synoptic descending/ascending motion through the whole domain.
(2) The ground surface is flat.
(3) A constant surface heat flux.

LES results show that in general $\langle \overline{w}\,\overline{\phi} \rangle$ is not 0 (Kanda et al., 2004; Steinfeld et al., 2007; Huang et al., 2008; Schalkwijk, 2008). The effect that a part of the total vertical flux is not measured due to the neglection of the contribution of $\overline{w}$ is called the flux imbalance. This effect is predicted by Mahrt (1998) and demonstrated by Kanda et al. (2004). The reason given is that if a stationary eddy is present at the measurement site that dominates the time series, the average of the vertical wind velocity will be the mean vertical wind velocity of that eddy at that site and therefore $\overline{w} \neq 0$. This is caused by Turbulent Organized Structures (TOS), of which examples can be seen in Figure 2.3 originating from Steinfeld et al. (2007). TOS are structures in which the air rises at specific positions and goes down at other specific positions, even if averaged over a longer time. These structures are confirmed by Huang et al. (2008). According to this paper the concept of single tower measurements fails in the presence of roll convection, since the mean imbalance increases when the TOS changes from cell-like to roll-like convection. For visualisation, these averages are calculated over a period of typically an hour.

The heat flux is not expressed in w and T, but is slightly more complicated. The sensible heat flux, Q_H is (Wyngaard, 1973)

$$Q_H = \rho c_p w T \tag{2.24}$$

in which ρ is the density of the air in kg m^{-3} and c_p is the specific heat of 1004.67 J kg^{-1} K^{-1} for dry air.

2.3 Superposition of concentrations and fluxes

The flux of a scalar has a vertical profile that is determined by the surface flux and the flux at the top of the boundary layer. It can be expressed as a linear superposition of two different processes, called top-down and bottom-up, (Wyngaard and Brost, 1984; Jonker et al., 1999) as will be shown in this paragraph. The concentration of the scalar in the top-down process is expressed as c_t and there is a top-down flux due to entrainment, wc_t. There is no top-down surface flux present. The concentration of the scalar in the bottom-up process is expressed as c_b and a bottom-up flux, wc_b, is present due to the surface flux. There is no entrainment flux for this process. The profiles as a function of the height relative to the inversion height are displayed in Figure 2.4. These profiles are representative for convective boundary layers.
Flux profiles of the bottom-up tracers can be studied separately from those of the top-down
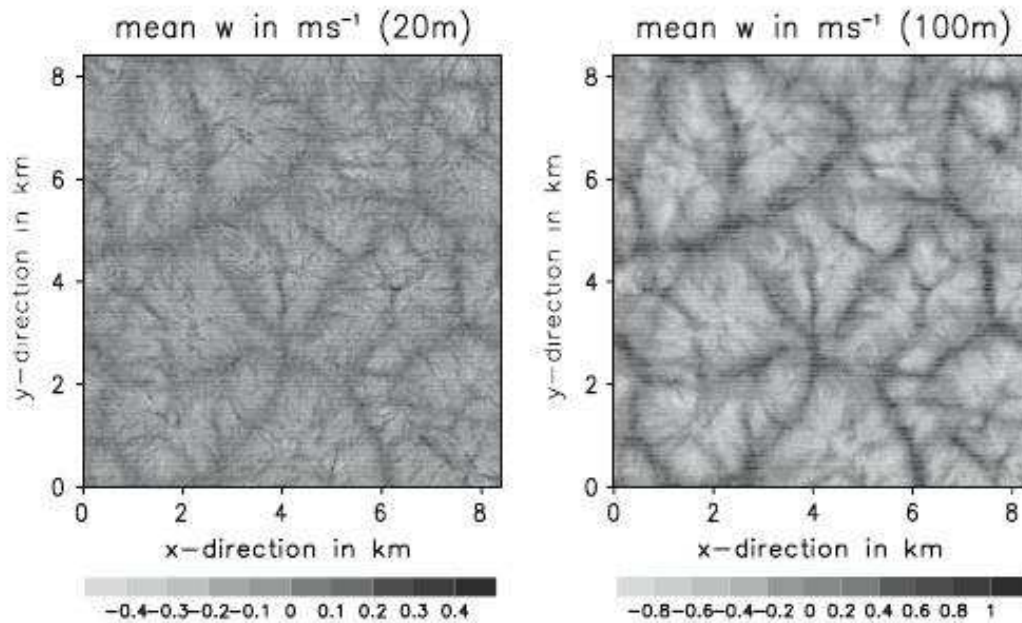
Figure 2.3: Vertical velocity maps for a geostrophic wind, u_g, of 0 m s^{-1} with 1-h averaging (period: 4-5 h) obtained at heights of 20 m (left) and 100 m (right) from Steinfeld et al. (2007).

tracers. The top-down flux is studied in simulations by prescribing an initial scalar concentration profile which is constant in the convective boundary layer and jumps to a lower concentration at the inversion height (Jonker et al., 1999; Schalkwijk, 2008). No surface flux is prescribed in the model, so all flux is caused by entrainment. The bottom-up flux is studied in simulations by prescribing a surface flux and preventing that an entrainment flux is present by making sure there is no concentration difference across the inversion.

The governing equation of a passive scalar for advection is the continuity equation (Jonker et al., 1999). An adaptation of equation (2.1) is used which is equal to (Nieuwstadt, 1992)

$$\frac{\partial c}{\partial t} + \mathbf{u} \cdot \nabla c + c \left(\nabla \cdot \mathbf{u}\right) = 0 \tag{2.25}$$

in which c is the scalar concentration. Solving equation (2.25) for the top-down case, c_t, and bottom-up case, c_b, separately, results in respectively

$$\frac{\partial c_t}{\partial t} + \mathbf{u} \cdot \nabla c_t + c_t \left(\nabla \cdot \mathbf{u}\right) = 0 \tag{2.26}$$

$$\frac{\partial c_b}{\partial t} + \mathbf{u} \cdot \nabla c_b + c_b \left(\nabla \cdot \mathbf{u}\right) = 0 \tag{2.27}$$

If taking

$$c_{\text{joined}} = A c_t + B c_b \tag{2.28}$$

and adding equations (2.26) times A and (2.27) times B, the result is

$$\frac{\partial \left(A c_t + B c_b\right)}{\partial t} + \mathbf{u} \cdot \nabla \left(A c_t + B c_b\right) + \left(A c_t + B c_b\right) \left(\nabla \cdot \mathbf{u}\right) = 0 \tag{2.29}$$
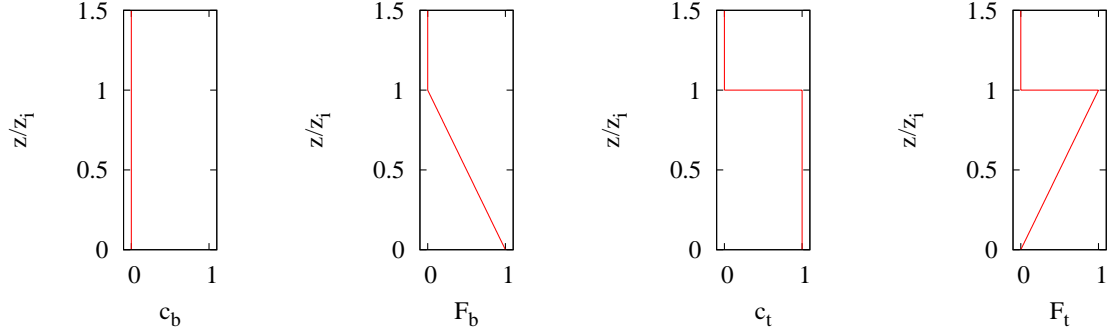
Figure 2.4: Profiles of the normalized concentrations and fluxes of a scalar. c_b is the concentration of the bottom-up tracer, F_b is the flux of the bottom-up tracer, c_t is the concentration of the top-down tracer and F_t is the flux of the top-down tracer. z is the height and z_i is the inversion height.

so

$$\frac{\partial c_{\text{joined}}}{\partial t} + \mathbf{u} \cdot \nabla c_{\text{joined}} + c_{\text{joined}} \left(\nabla \cdot \mathbf{u} \right) = 0 \tag{2.30}$$

This shows that the joined concentration profile also complies to the conservation equation because of linearity. Also the other equations that describe the profiles are linear. Therefore, all cases with a bottom-up flux and a top-down flux under certain conditions can be examined by adding the solution under those conditions for the case with only a bottom-up flux to that of the case with only a top-down flux with the proper weight factors.

2.4 The imbalance

The ratio of the flux that is not measured using Eddy Covariance measurements versus the spatially averaged total flux is called the flux imbalance. It is defined (Kanda et al., 2004) as

$$I = \frac{\overline{w'\phi'} - \langle \overline{F} \rangle}{\langle \overline{F} \rangle} \tag{2.31}$$

Using equation (2.20), equation (2.31) becomes

$$I = \frac{\left(\overline{w'\phi'} - \langle \overline{w'\phi'} \rangle \right) - \langle \overline{w}\,\overline{\phi} \rangle}{\langle \overline{F} \rangle} \tag{2.32}$$

$$\langle I \rangle = \frac{- \langle \overline{w}\,\overline{\phi} \rangle}{\langle \overline{F} \rangle} \tag{2.33}$$

Equation (2.33) shows that if $\overline{w}$ would be 0 or if the spatial correlation between $\overline{w}$ and $\overline{\phi}$ would be 0, $\langle I \rangle$ would be 0. However, figures generated by Kanda et al. (2004), Schalkwijk (2008) and others show that $\langle I \rangle \neq 0$ and actually $\langle I \rangle < 0$. I can still be greater than 0 at a specific location. According to Kanda et al. (2004), the magnitude of the local terms $\overline{w'\theta'}$ are much larger than their spatial average, so $\left| \overline{w'\theta'} \right| >> \left| \langle \overline{w'\theta'} \rangle \right|$. This causes the graph of the numbers of occurrence of I-values for heat flux, as shown in Figure 2.5, to lack a very sharp peak. He did not examine this behaviour of I in the case that ϕ is the concentration of a substance.
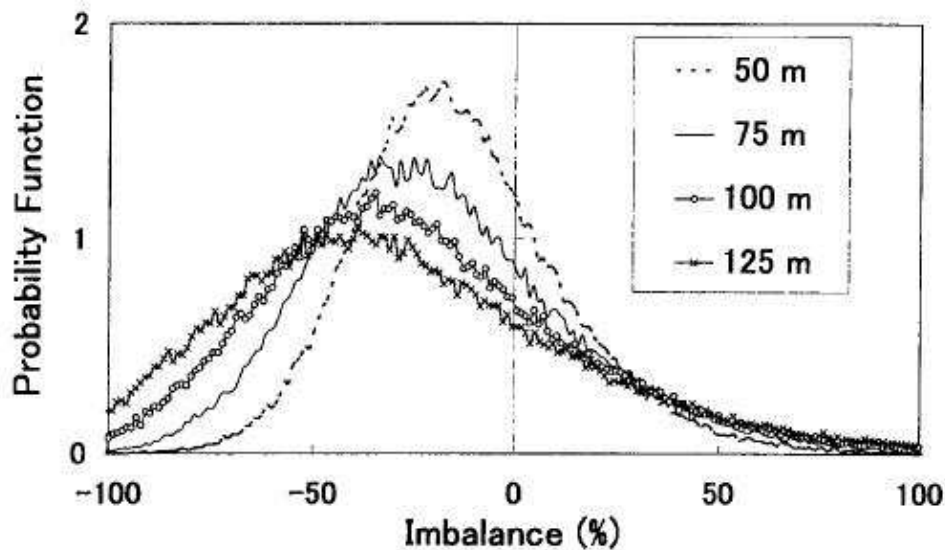
Figure 2.5: Probability density functions of the imbalance for heat at different heights according to the number of occurences in simulations with a high resolution grid. The geostrophic wind is set at $U_g = 0\ \mathrm{m\ s^{-1}}$, the averaging time is $t_a = 1$ hour and the measurement period starts after 2 simulated hours. This graph originates from Kanda et al. (2004) where it is denoted as Figure 7.

In general, slight inhomogeneous ground fluxes cause the $\langle I \rangle$ to be nearer to 0 (Kanda et al., 2004), as do higher geostrophic velocities (Kanda et al., 2004; Lee, 1998; Mahrt, 1998) (or higher friction velocities as used by Huang et al. (2008)) and lower altitudes (Kanda et al., 2004; Lee, 1998; Steinfeld et al., 2007). The two latter are contained in the Imbalance predicting equation (2.51), which will be discussed later. Also other inhomogeneities could influence the imbalance, like inhomogeneous shaped surfaces, wind velocities or temperature profiles.

The variance of the local values of I, σ_I^2, increases if the magnitude of $\langle I \rangle$ increases. However, according to Schalkwijk (2008), this is not always the case when I_S is considered. I_S is defined by $I_S = -\langle \overline{w}\,\overline{\phi} \rangle$ and can be seen as the absolute difference between the EC-flux and the real flux instead of the relative difference. Even if $\langle I_S \rangle \approx 0$, $\sigma_{I_S}^2$ could be very big. This indicates that even when the observer does not on average expect an offset in his flux measurement, the spread in the results of measurements relative to the real flux can be big. However, according to the behaviour of the variance of I, this is only the case for small fluxes.

2.4.1 The reason of a negative averaged imbalance

Using equations (2.15) and (2.31), the spatially averaged flux imbalance can be expressed as

$$\langle I \rangle = -\frac{\langle \overline{w}\,\overline{\phi} \rangle}{\langle \overline{w\phi} \rangle} \tag{2.34}$$

There are a few hypotheses why $\frac{\langle \overline{w}\,\overline{\phi} \rangle}{\langle \overline{w\phi} \rangle} > 0$.

(1) It could be that $\overline{w}$ is correlated to $\overline{\phi}$ at every position.
(2) It could be that $\overline{\phi}$ is almost constant in a horizontal plane.

(3) It could be that it is caused by calculating the flux over a time interval that is not a multiple of the time with which w and ϕ are periodic.

If hypothesis (1) is true, $\langle \overline{w}\,\overline{\phi} \rangle$ can be calculated by measuring the spatial behaviour of $\overline{w}$ and $\overline{\phi}$. The nature of the relation might be different for different ϕ's. Huang et al. (2008) define the linear correlation of $\overline{w}$ with $\overline{\phi}$ as

$$r = \frac{\langle \overline{w}\,\overline{\phi} \rangle}{\sqrt{\langle \overline{w}''^2 \rangle \langle \overline{\phi}''^2 \rangle}} \tag{2.35}$$

which results in

$$\langle \overline{w}\,\overline{\phi} \rangle = r \sqrt{\langle \overline{w}''^2 \rangle \langle \overline{\phi}''^2 \rangle} \tag{2.36}$$

They found that r remains almost constant for increasing geostrophic wind, but is dependent on the height of measurement. For heat the calculated linear correlation is about 0.87 and for bottom-up tracers it is about 0.79. Top-down tracers are less correlated with the temporal averaged vertical wind velocity, having a linear correlation of about 0.40. These results show that a correlation exists for all scalars and that knowing the spatial variances of the temporal averaged values of w and ϕ and knowing the function of r is enough to make an estimate for $\langle \overline{w}\,\overline{\phi} \rangle$. However, since real measurements are performed at a single location only, this can not be accomplished from observations.

If hypothesis (2) would be true, $\langle \overline{w}\,\overline{\phi} \rangle \approx \langle \overline{w} \rangle \langle \overline{\phi} \rangle$. Since $\langle \overline{\phi} \rangle$ is a constant larger than 0 for concentrations as well as temperature, the result is that $\langle \overline{w}\,\overline{\phi} \rangle \propto \langle \overline{w} \rangle$. In practice this results in a positive value for $\langle \overline{w}\,\overline{\phi} \rangle$. This is due to the fact that in case of an upward heat flux, rising air has a higher temperature and therefore a lower density than descending air. Because of this, a larger volume of air should rise than descend, so the average of w should be larger than 0 (Webb et al., 1980). Therefore, in experimental data the flux is corrected by the Webb correction (Liebethal and Foken, 2003). However, in LES experiments this effect should be non-existent, since the spatial average of the vertical wind speed is forced to be 0 m s^{-1} at any point in time and the air parcels do not shrink or expand. Hypothesis (2) is therefore not a possible reason for simulated imbalances. However, it should be noted that in practice the density does play a role. This leads to the conclusion that boundary condition (1) of the research using LES models, which states that there is no synoptic descending or ascending motion through the whole domain, is not entirely consistent with practice.

Hypothesis (3) is explained in Appendix A. It considers a vertical wind velocity, w, and a scalar, ϕ, that can be described with a periodic signal and are given by equations (A.8) and (A.9)

$$w = w_0 \sin\left(2\pi \frac{x - \overline{u}t}{L} + \theta_1 \right) \tag{2.37}$$

$$\phi = \phi_0 \sin\left(2\pi \frac{x - \overline{u}t}{L} + \theta_1 + \theta_2 \right) + \phi_1 \tag{2.38}$$

w_0 and ϕ_0 are their respective amplitudes. The coordinate system is chosen such that the horizontal wind points to the positive x-direction. The average value of the horizontal wind speed is $\overline{u}$. The vertical wind speed and magnitude of the scalar are periodic with distance L. θ_1 is a general phase shift of the two variables and θ_2 is the phase shift of ϕ with respect
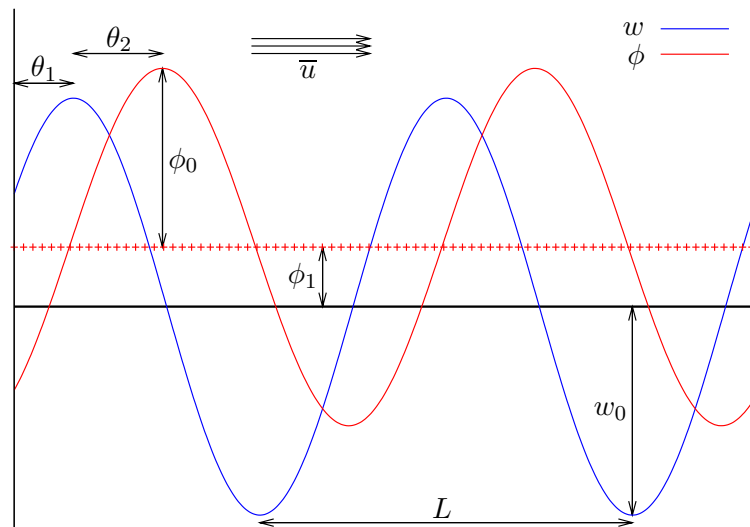
Figure 2.6: Schematic overview of the profiles of the vertical wind velocity, w, and the investigated scalar, ϕ, that are assumed in the derivation of a theoretical imbalance. The profile of the vertical wind velocity is a sinusoid and the profile of the scalar is a sinusoid plus a constant, ϕ_1. Both profiles are periodic over a distance L. The profiles are assumed to be constant and are advected past the sensors with a horizontal velocity $\overline{u}$. The profiles have a general phase shift of θ_1 and ϕ has an extra phase shift of θ_2 with respect to w. The amplitude of the periodic w signal is w_0 and the amplitude of the periodic ϕ signal is ϕ_0.

to w. In this calculation the assumption is made that w and ϕ both are periodic with the same period. Another assumption is that this periodicity is both in space and in time and that those two periodicities are coupled. The second of these two assumptions is based on the aforementioned Taylor's frozen turbulence hypothesis. A schematic representation is shown in Figure 2.6. Under these assumptions equations (A.19), (A.24) and (A.26) are derived. They are presented here for convenience

$$\langle \overline{w\phi} \rangle = \frac{w_o \phi_0}{2} \cos\left(\theta_2\right) \tag{2.39}$$

$$\langle \overline{w}\,\overline{\phi} \rangle = \frac{L^2 w_0 \phi_0}{4\pi^2 \overline{u}^2 T^2} \cos\left(\theta_2\right) \left[1 - \cos\left(2\pi \frac{\overline{u}T}{L}\right)\right] \tag{2.40}$$

$$\langle I \rangle = -\frac{\langle \overline{w\phi} \rangle}{\langle \overline{w}\,\overline{\phi} \rangle} = -\frac{L^2}{2\pi^2 \overline{u}^2 T^2} \left[1 - \cos\left(2\pi \frac{\overline{u}T}{L}\right)\right] \tag{2.41}$$

In these equations T is the period of measurement. Equation (A.19) represents the total vertical flux and equation (A.24) is the part of the vertical flux that the EC technique does not measure. It is clear that $\frac{\langle \overline{w}\,\overline{\phi} \rangle}{\langle \overline{w\phi} \rangle}$ is always positive and therefore the spatially averaged flux imbalance is always negative. Defining the dimensionless measurement time

$$T^{\dagger} = \frac{\overline{u}T}{L} \tag{2.42}$$

equation (A.26) is rewritten into equation (A.28)

$$\langle I \rangle = \frac{\cos\left(2\pi T^{\dagger}\right) - 1}{2\pi^2 T^{\dagger 2}} \tag{2.43}$$

In this equation $\langle I \rangle$ is always negative, like expected. For large $T^\dagger$, $\langle I \rangle$ goes to 0. This means that if $\overline{u}$ is large or L is small, $\langle I \rangle$ will become small. In that case eddies are advected past the sensors fast. For a large measurement time, the flux imbalance also becomes small, because in that case also many eddies are advected past the sensors during a flux measurement.

In order to derive equation (A.28), it is assumed that w and ϕ are periodic signals with the same periodicity. However each quantity can be described by more than one sinusoid. For example

$$w = \sum_k w_k \sin\left(2\pi\frac{x - \overline{u}t}{L_k} + \theta_k\right) \tag{2.44}$$

The periodic distance seems of the order of a kilometre according to Figure 2.3. The spread in L_k looks very small for a measurement height of 100 m , but at a measurement height of 20 m, the structures are less sharp which indicates a larger spread in length scales. The contribution to $\langle I \rangle$ from a w-term times a ϕ-term with another periodicity can not be predicted by equation (A.28).

2.4.2 Functions to correct for the imbalance

Being able to predict the imbalance as a function of several conditions results in more accurate measurements. The dependence of I on the horizontal wind velocity, U, and stability is important. A possible dimensionless indicator of stability is $\frac{z}{L}$. z is the measurement height in m and L is the Monin-Obukhov length in m. The Monin-Obukhov length is the height at which the turbulence generated by shear is in balance with the dissipation by buoyancy. It is a good indicator of stability as long as $z \lesssim 0.1z_i$ (Wyngaard, 1973). z_i is the mixing-layer height in m. The Monin-Obukhov length is expressed as (Wyngaard, 1973; Vickers and Mahrt, 2003)

$$L = -\frac{u_*^3}{Q_0\left(\frac{g}{\theta}\right)\kappa} \tag{2.45}$$

in which u_* is the friction velocity in m s^{-1}, defined by

$$u_* = \sqrt[4]{\overline{\langle u''w''\rangle}_0^2 + \overline{\langle v''w''\rangle}_0^2} \tag{2.46}$$

κ is the dimensionless von Kármán's constant and $\kappa \cong 0.4$. θ is the potential temperature in K, which is defined as (Panofsky and Dutton, 1984)

$$\theta = T\left(\frac{p_0}{p}\right)^{\left(\frac{R}{c_p}\right)} \tag{2.47}$$

in which p_0 is a reference pressure of 10^5 Pa and $R = 287.04$ J K^{-1} kg^{-1}. Using the gas law, the hydrostatic equation and a Taylor expansion, equation (2.47) results in (Stull, 1988)

$$\theta \cong T + \frac{gz}{c_p} \tag{2.48}$$

in which $g = 9.8$ m s^{-2}. Equation (2.48) is valid if $p_0 - p \ll p$.

Q_0 is the virtual heat flux near the ground in K m s^{-1}. It is given by (Vickers and Mahrt, 2003)

$$Q_0 = \overline{w'\theta'_{v0}} \tag{2.49}$$

Table 2.1: The coefficients of equations (2.52) and (2.53) in case of heat, bottom-up tracers and top-down tracers as published by Huang et al. (2008). The averaging time is 1 hour.

Coefficient	Heat	Bottom-up tracers	Top-down tracers
d_1	4.2	4.3	4.7
d_2	-16.0	-16.0	-16.0
d_3	2.1	3.5	6.7
d_4	-8.0	-6.2	-4.5
d_5	-0.38	-0.45	-0.4

The virtual potential temperature, θ_v, measured in K, is given by (Kaimal, 1993; Stull, 1988)

$$\theta_v = \theta \cdot (1 + 0.61 \cdot r) \tag{2.50}$$

in which r is the dimensionless mixing ratio of water vapor in the air.

If $\frac{z}{L} < 0$, the flow is unstable and if $\frac{z}{L} > 0$, the flow is stable (Stull, 1988; Nieuwstadt, 1992). If $\frac{z}{L} = 0$, the flow is neutral. If $\left|\frac{z}{L}\right| > 1$, the buoyancy effects dominate and if $\left|\frac{z}{L}\right| < 1$, the turbulence production by shear dominates.

Huang et al. (2008) found from LES results a function that predicts $\langle I \rangle$ for an averaging time of 1 hour as a function of different parameters. Instead of $\frac{z}{L}$, he used the height normalized by the inversion height as indicator.

$$\langle I \rangle = -f_1 \left(\frac{u_*}{w_*} \right) f_2 \left(\frac{z}{z_i} \right) \tag{2.51}$$

In this equation

$$f_1 \left(\frac{u_*}{w_*} \right) = e^{d_1 + d_2 \frac{u_*}{w_*}} + d_3 \tag{2.52}$$

$$f_2 \left(\frac{z}{z_i} \right) = \sqrt{1.1 + d_4 \left(\frac{z}{z_i} + d_5 \right)^2} \tag{2.53}$$

$$w_* = \sqrt[3]{\frac{g \overline{w\theta}_0 z_i}{T_0}} \tag{2.54}$$

$\overline{w\theta}_0$ is the surface heat flux and T_0 is the surface temperature (Panofsky and Dutton, 1984). Please note that the convective velocity, w_*, is defined locally and only averaged in time, whereas the friction velocity in equation (2.46) is defined using averages in both space and time. The values for d_x are determined for heat flux and particle fluxes of bottom up tracers and top down tracers. This is done for flux measurements of 1 hour. Although the values are not equal for the three cases, the solutions lie near to each other and the functions behave very similar. All values for d_2, d_4 and d_5 are negative and all values for d_1 and d_3 are positive. The values are listed in Table 2.1. The functions $f_1 \left(\frac{u_*}{w_*} \right)$ and $f_2 \left(\frac{z}{z_i} \right)$ are plotted in Figure 2.7 using these values. Equation (2.53) is restricted to $\frac{z}{z_i} \leq 0.5$. This is done to avoid the zero-crossing of the heat flux (Huang et al., 2008).

2.4.3 Flux observations from real measurements

It is not straightforward to compare the data obtained by simulations to observations. For example, in practice only single-tower measurements are performed. The local imbalance

Dependency of the imbalance prediction function on the scaled friction velocity
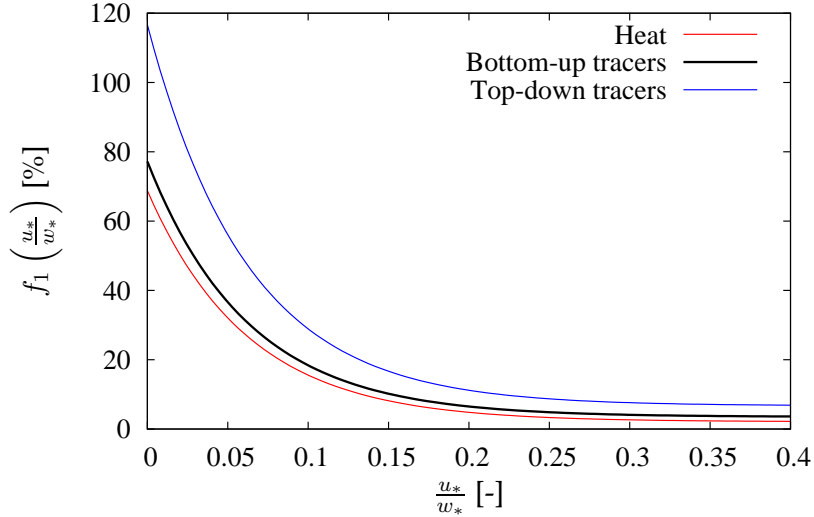
Dependency of the imbalance prediction function on the scaled height
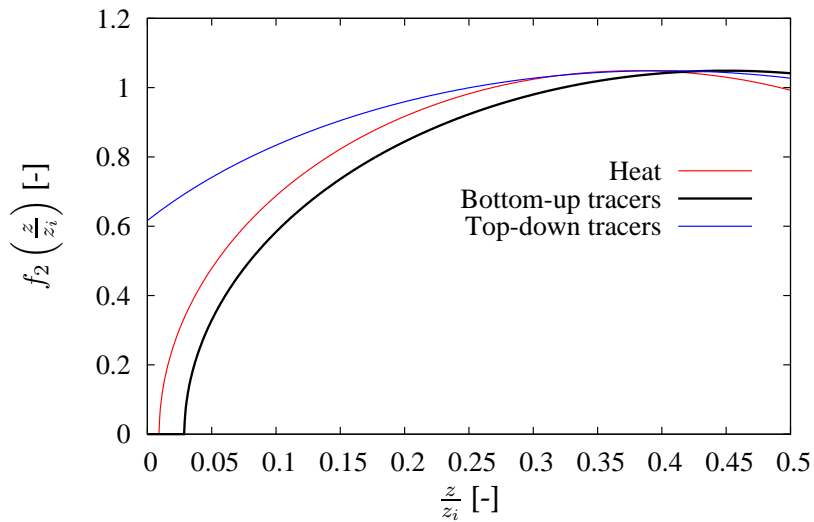
Figure 2.7: In these two graphs the functions to predict the imbalance, as used in equation (2.51), are shown. In the upper graph f_1 in %, as defined by equation (2.52), is plotted. This graph shows the dependence of the imbalance on the friction velocity, u_*, scaled by the convective velocity w_*. In the lower graph the dimensionless f_2, as defined by equation (2.53), is plotted. This graph shows the dependence of the imbalance on the height, z, scaled by the inversion height z_i. The constants used in equations (2.52) and (2.53) originate from Table 2.1 and are valid for fluxes determined over an hour. The equations and constants are given by Huang et al. (2008).

behaves like the found probability density functions (Huang et al., 2008; Kanda et al., 2004; Schalkwijk, 2008; Steinfeld et al., 2007) as shown in Figure 2.5. Since in observations no spatial average can be taken, the imbalance is not equal to the spatially averaged imbalance. A random distortion due to the spread in the imbalance probability density function is present in the imbalance of the determined flux. Because of this distortion, local EC measurements corrected with the known imbalance functions from Paragraph 2.4.2 are not necessarily equal to the spatially averaged total vertical flux.

Another difference between LES and observation that should not be ignored, is the diurnal cycle. This is not taken into account in the simulations. Since this cycle influences the large turbulent cycles in the air, it is of importance. An example of the influence of the diurnal cycle can be seen in Figure 2.8. It shows how the standard deviation of the vertical wind velocities varies during a day. Also the heat flux is a function of the hour at which the measurement takes place. The temperature is highly affected by the diurnal cycle. This is troublesome if measurements are performed in which stationary problems are investigated. In order to compensate for that, the trend in the temperature data can be determined and then be deducted from the temperature measurements during that period.

The influence of surface flux inhomogeneity is of importance too. The inhomogeneous part of the surface flux is the surface flux minus the average surface flux over the measurement area. In simulations the surface flux is almost always assumed to be homogeneous, but in practice this is never the case. According to Kanda et al. (2004) the imbalance is least when the inhomogeneous term of the surface flux is about 5% relative to the homogeneous term. Also Inagaki et al. (2006) performed research on the influence of surface flux inhomogeneity. They concluded that a heterogeneous ground flux has influence on the imbalance and that a strong mesoscale circulation leads to a small imbalance. According to simulations from Steinfeld et al. (2007), $\langle I \rangle$ is next to 0 in a stable boundary layer and in a convective boundary layer the magnitude of $\langle I \rangle$ only decreases for higher geostrophic winds if the TOS does not change from cell-like to roll-like convection.
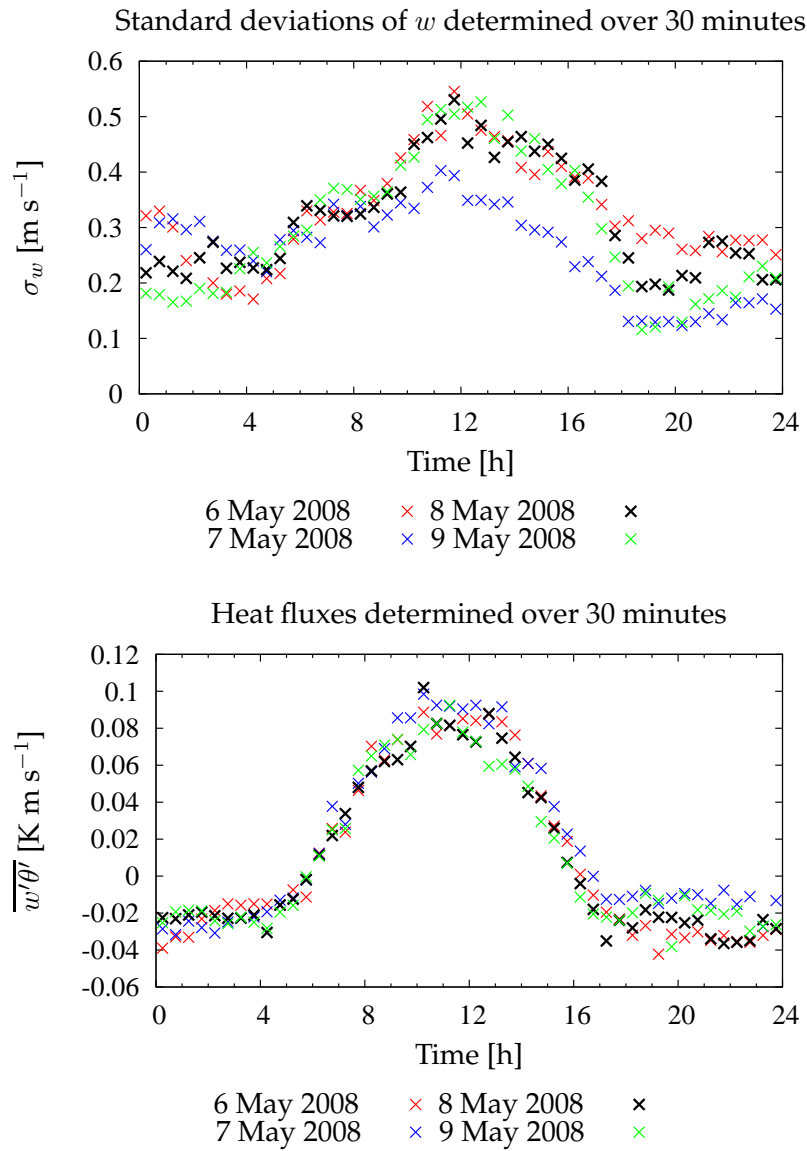
Figure 2.8: In these plots the influence of the diurnal cycle on σ_w (upper graph) and the turbulent kinetic heat flux (lower graph) is shown. The heat fluxes and the standard deviations of the vertical wind velocities are determined over periods of 30 minutes. The results are plotted as a function of the time (in UTC). The data originates from the Cabauw site (Paragraph 3.1) with a frequency of 10 Hz from a sonic anemometer at a height of 3 m. Data from 6 May until 9 May 2008 is used.

Chapter 3

Measurements

In Paragraph 3.1 the measurement site and method of measuring are described. The measured wind velocities are corrected for distortions by the measurement devices. This correction and its influence on flux measurements is discussed in Paragraph 3.2. In Paragraph 3.3 the behaviour of the vertical wind velocities in observations is examined.

3.1 Measurement setup

The measurement data originates from the KNMI. Wind velocities and temperatures are measured by Gill R3 sonic anemometers at 3 m, 60 m, 100 m and 180 m height. The specific humidity and carbon dioxide concentrations are measured at the same heights by LICOR 7500 Open path H_2O/CO_2 sensors (Bosveld, 2008 - 2009). The measurement site is located near the village Cabauw. Its geographical location is at 0.7 m below sea level at 51°58′ N latitude and 4°54′ E longitude. The measurements at 3 m height are conducted 200 m north of the 200 m high measurement tower of the KNMI, shown in Figure 3.1. This sonic anemometer is placed on a small mast. The measurements at 60 m, 100 m and 180 m height are conducted at the tower. These anemometers are placed on beams pointing south east. Unfortunately because of this, wind coming from a north westerly direction is distorted. This happens if the wind direction is about 290°, as can be seen by the peaks in Figure E.1. Because of this, measurements during periods in which the wind direction is near 290° should be neglected. The sonic anemometer at 3 m height is placed at some distance from the tall tower and the measured wind is therefore not distorted by the tower. Under the sonic anemometers at 3 m height and those placed on the measurement tower at 60 m and 180 m height, spirit levels are placed in order to check whether the sonic anemometers are aligned with a fixed angle with respect to the earth's surface. Measurements at these spirit levels are shown in Appendix D.

Three data sets are used. The data sets differ in the period that is investigated and in the way the data is treated. In one set raw measurement data is provided. In the other two sets, data averaged over 10 minutes is provided and a correction to the velocity data to compensate for wind tilt is applied. This correction is treated in Paragraph 3.2. Also fluxes over 10 minutes are given in those sets. The three data sets are:

(1) **Original processed data set**: This data set consists of 10 minute averaged data covering the period from 1 January to 31 December 2007. This data is corrected using the original wind tilt correction angles. The average horizontal and vertical wind velocities and concentrations of water and carbon dioxide as well as the eddy-covariance

Figure 3.1: On the left a picture of the tall measurement tower of the KNMI at Cabauw is shown. This site is located on a height of 0.7 m below sea level at the coordinates 51°58′ N latitude and 4°54′ E longitude. The sonic anemometers at 60 m, 100 m and 180 m are placed on beams pointing south east from the tower. The sonic anemometer at 3 m height is placed 200 m north of the main tower. All sonic anemometers are of the type Gill R3 (Bosveld, 2008 - 2009). On the right a Gill R3 sonic anemometer is shown.

fluxes of heat, water and carbon dioxide during 10 minutes are given.

(2) **Raw data set**: This data set consists of raw measurement data at 10 Hz covering the period from 3 May to 13 May 2008. This data is not corrected for wind tilt. All three velocity components, the temperature, the humidity and the amount of carbon dioxide are given.

(3) **Revised processed data set**: This data set consists of 10 minute averaged data covering the period from 1 May to 31 May 2008. This data is corrected using the corrected wind tilt correction angles as given in Appendix E. Similar to data set (1), the average horizontal and vertical wind velocities and concentrations of water and carbon dioxide as well as the eddy-covariance fluxes of heat, water and carbon dioxide during 10 minutes are given.

3.2 The tilt correction

3.2.1 Background of the tilt correction

In present day measurement data processing, the sonic anemometer has to be placed perpendicular to the earth's surface (Wilczak et al., 2001). However, this is almost never the case. It is assumed that the time averaged vertical wind velocity, $\overline{w}$, should be 0 and that if $\overline{w} \neq 0$ this means that the anemometer is not aligned correctly. Even if the anemometer is standing perpendicular, one should correct for the coordinate system of the measurements.

If the sonic anemometer is placed upon a platform, the wind is tilted around that platform when it reaches the anemometer. Also the sonic anemometer itself tilts the wind. In order to correct for this a few methods exists. Frequently used methods are the double rotation (DR), triple rotation (TR), the planar fit (PF) and the wind tilt correction (WTC). In all of these the non-zero $\overline{w}$ is corrected for by virtually rotating the anemometer in such a way that $\overline{w}$ becomes 0 again.

A big difference between the wind tilt correction (WTC) or planar fit (PF) and the rotation methods like double rotation (DR) and triple rotation (TR) is the amount of calculated correcting rotations (Slager, 2001). In the DR and TR methods the data is rotated separately in each block-average period, such that $\overline{w} = 0$ in every period and other conditions are fullfilled. After calculating the needed rotation, it is applied to the data in that time frame. In general, the average is calculated over 30 minutes (Vickers and Mahrt, 2003; Kroon et al., 2007) but 10 minutes or an hour are common too. Too frequent coordinate rotations can lead to faulty EC flux results, because of too low wind speeds or a too high variation in the wind direction during the averaging period (Twine et al., 2000). The planar fit and wind tilt correction methods calculate a rotation once. This is done using a relatively large data set which is obtained over a month or a longer period. That calculated rotation is used to evaluate all further data. The planar fit is based on a tilted sonic anemometer only. Therefore the calculated rotation lies in a plane; the coordinate rotation for data obtained at a certain wind direction is the negative of the rotation for data obtained at the opposite wind direction. The wind tilt correction also compensates for the tilt of the wind due to the supporting platform and the sonic anemometer itself. To realise this the wind directions are binned into sectors and the coordinate rotation is calculated for each sector separately. Due to the temperature dependent density of air as described in Paragraph 2.4.1, an average vertical wind velocity is present during day and during night. During day this velocity is upwards while during night this velocity is downwards. Both averaged vertical wind velocities are of the order of tenths of mm s^{-1} (Liebethal and Foken, 2003). Therefore the vertical wind velocity averaged over twenty-four hours is of that same order or even smaller. Because of this, the assumption that the vertical wind velocity is 0 m s^{-1} over a very long period seems valid for homogeneous terrain. The characteristics of the double and triple rotations, the planar fit and the wind tilt correction are (Lee et al., 2004):

Rotation is determined per single flux measurement	Rotation is determined once over a long period (e.g., a month or a year)
DR: $\overline{w} = 0$ $\overline{v} = 0$	PF: $\overline{w} = 0$ The correcting rotation is defined on a plane.
TR: $\overline{w} = 0$ $\overline{v} = 0$ $\overline{v'w'} = 0$	WTC: $\overline{w} = 0$ The correcting rotation is defined for every wind direction sector separately.

Another method to determine the rotation angle was considered during the project. Since the standard deviation of the vertical wind velocity is generally smaller than that of the horizontal wind velocity, it came to mind that evaluating the variance of the vertical wind velocity, σ_w, as a function of the rotation angle, β, might show the needed rotation angle. If no horizontal wind velocities would distort the data, the standard deviation would be at its minimum. However, in Appendix B it is shown that this is not the case.

LES experiments show that locally $\overline{w}$ is not equal to 0 if averaged over an hour or less and Chapter 2 shows that the spatially averaged imbalance is caused because of this. By using

the assumption that over a short period $\overline{w} = 0$ in the coordinate rotation method, one would not be able to research this effect. Consequently the double rotation and the triple rotation methods can not be used in this research. Since the sonic anemometers and the beams on which they are placed tilt the wind, the wind tilt correction method is better suited to correct the data than the planar fit method. Therefore, the wind tilt correction method is used to correct the coordinate system in this thesis. The rotation should be determined once in a period in which the position of the anemometer is not changed. A new rotation should only be made after a storm, a collision with a cow or something similar. After determining the standard rotation, non-rotated data should only be rotated using this standard.

3.2.2   The planar fit

The wind tilt correction method is based on the planar fit. The methods are used to correct for the fact that the anemometer and the streamlines of the wind are not oriented perpendicular to each other. It is assumed that this correction is only dependent on the wind direction and not on other parameters like the horizontal wind velocity, stability or time of the year. First the planar fit is treated. According to Lee (1998) and Paw U et al. (2000)

$$\overline{w}_{\text{measured}} = \overline{w} - a\left(\theta\right) - b\left(\theta\right)\overline{u}_{\text{measured}} \tag{3.1}$$

In this equation $\overline{w}_{\text{measured}}$ and $\overline{u}_{\text{measured}}$ are the measured time averaged vertical and horizontal velocity respectively. $\overline{w}$ is the actual time averaged vertical velocity and $a\left(\theta\right)$ and $b\left(\theta\right)$ are coefficients dependent on the wind direction, θ. Determining the coefficients can be tricky. Rotating the measurement values using equation (3.1), gives rise to a systematic bias to $\overline{w}$ if the air at the site locally has a preferred direction of time averaged vertical motion (Lee, 1998). Wilczak et al. (2001) state that in general the sonic anemometer also gives a bias in the wind velocities which should be subtracted from the measured wind speeds and is hard to determine. This bias is of the order of tens of cm s^{-1}. In addition to that, the sonic anemometer distorts the flow by its presence.
Equation (3.1) is adapted by Lee et al. (2004) such that the dependency of the wind direction angle is absent. Instead of that, the vertical wind velocity, $\overline{w}$, is linear dependent on both horizontal wind directions, $\overline{u}$ and $\overline{v}$. This is possible because the correcting rotation is defined on a plane.

$$\overline{w}_{\text{measured}} = \overline{w} - a\overline{u}_{\text{measured}} - b\overline{v}_{\text{measured}} \tag{3.2}$$

Likewise, the true horizontal wind velocities, u and v, are dependent on the measured vertical wind velocity, w_{measured}. The real velocity vector, $\boldsymbol{u}_{\text{real}}$, is calculated by rotating the measured velocity vector, $\boldsymbol{u}_{\text{measured}}$ by three matrices (Finnigan, 2004). One rotation matrix, $\boldsymbol{R1}^{-1}\left(\alpha\right)$ describes the rotation around the z-axis with an angle α. The second rotation matrix, $\boldsymbol{R2}^{-1}\left(\beta\right)$ describes the rotation around the y-axis with an angle β. The last matrix, $\boldsymbol{R3}^{-1}\left(\gamma\right)$ describes the rotation around the x-axis with an angle γ. These matrices are used in

$$\left\{\begin{matrix} u \\ v \\ w \end{matrix}\right\}_{\text{real}} = \boldsymbol{R1}^{-1}\left(\alpha\right) \cdot \boldsymbol{R3}^{-1}\left(\gamma\right) \cdot \boldsymbol{R2}^{-1}\left(\beta\right) \cdot \left\{\begin{matrix} u \\ v \\ w \end{matrix}\right\}_{\text{measured}} \tag{3.3}$$

3.2.3 The wind tilt correction

The wind tilt correction method is similar to the planar fit method, but instead of a correcting rotation defined on a plane, the correcting rotation is determined as a function of the wind direction. This makes it possible to compensate for the wind tilt due to the supporting platform and the sonic anemometer. The wind directions are binned into 18 sectors with a range of $20°$ and for each sector the rotation is calculated that is needed to let $\overline{w} = 0$ over a long time. During the time period from which data is used to calculate the rotations, there should not be any interruptions. It is assumed that $\overline{w} = 0$, independent on the direction of the wind. Another assumption is that the tilt for each wind direction is independent of the wind velocity. In case of the KNMI, a wind tilt correction was calculated over a month (Bosveld, 2008). This will be discussed in paragraph 3.2.4.

In data sets 1 and 3 of the KNMI (Paragraph 3.1), u is already defined as the wind velocity in the direction in which the average horizontal wind velocity points and this direction is given. Therefore rotations $\boldsymbol{R1}^{-1}(\alpha)$ and $\boldsymbol{R3}^{-1}(\gamma)$ are not necessary anymore for the processed data. For the raw data of data set 2 this is not the case and the two horizontal wind velocities have to be used to determine the wind direction and horizontal wind speed. Different from the planar fit method the rotation angle, β, of the wind tilt correction is dependent on the angle from which the wind arrives. Equation (3.3) results in

$$\left\{\begin{array}{c} u \\ v \\ w \end{array}\right\}_{\text{real}} = \boldsymbol{R}\left(\beta\left(\theta\right)\right) \cdot \left\{\begin{array}{c} u \\ v \\ w \end{array}\right\}_{\text{measured}} \tag{3.4}$$

in which θ is the angle from which the wind arrives, β is the angle of rotation from the z-axis to the x-axis and

$$\boldsymbol{R} = \left(\begin{array}{ccc} \cos\left(\beta\left(\theta\right)\right) & 0 & \sin\left(\beta\left(\theta\right)\right) \\ 0 & 1 & 0 \\ -\sin\left(\beta\left(\theta\right)\right) & 0 & \cos\left(\beta\left(\theta\right)\right) \end{array}\right) \tag{3.5}$$

Equation (3.4) can be written as

$$\begin{aligned} u_{\text{real}} &= \cos\left(\beta\left(\theta\right)\right) u_{\text{measured}} + \sin\left(\beta\left(\theta\right)\right) w_{\text{measured}} \\ v_{\text{real}} &= v_{\text{measured}} \\ w_{\text{real}} &= \cos\left(\beta\left(\theta\right)\right) w_{\text{measured}} - \sin\left(\beta\left(\theta\right)\right) u_{\text{measured}} \end{aligned} \tag{3.6}$$

$\beta\left(\theta\right)$ is dependent on the surroundings of the sonic anemometer and there is no function that is continuous dependent on the wind direction, that can predict it. Therefore it is determined experimentally. The wind directions are binned into 18 sectors and the rotation angle is determined for each sector. This results in

$$\beta\left(\theta\right) = \beta_N \quad , \quad N = \text{round}\left(\frac{\theta + 10}{20}\right) \tag{3.7}$$

in which N is the number of the sector. For each section the temporal averages of the vertical wind velocity, $\overline{w}_N$, and the horizontal wind velocity, $\overline{u}_N$, are calculated. The corresponding rotation angle for each section is then given by

$$\beta_N = \arctan\frac{\overline{w}_N}{\overline{u}_N} \tag{3.8}$$

$\overline{w}$ and β at 180 m between 3 May and 13 May 2008 from 10 h to 18 h
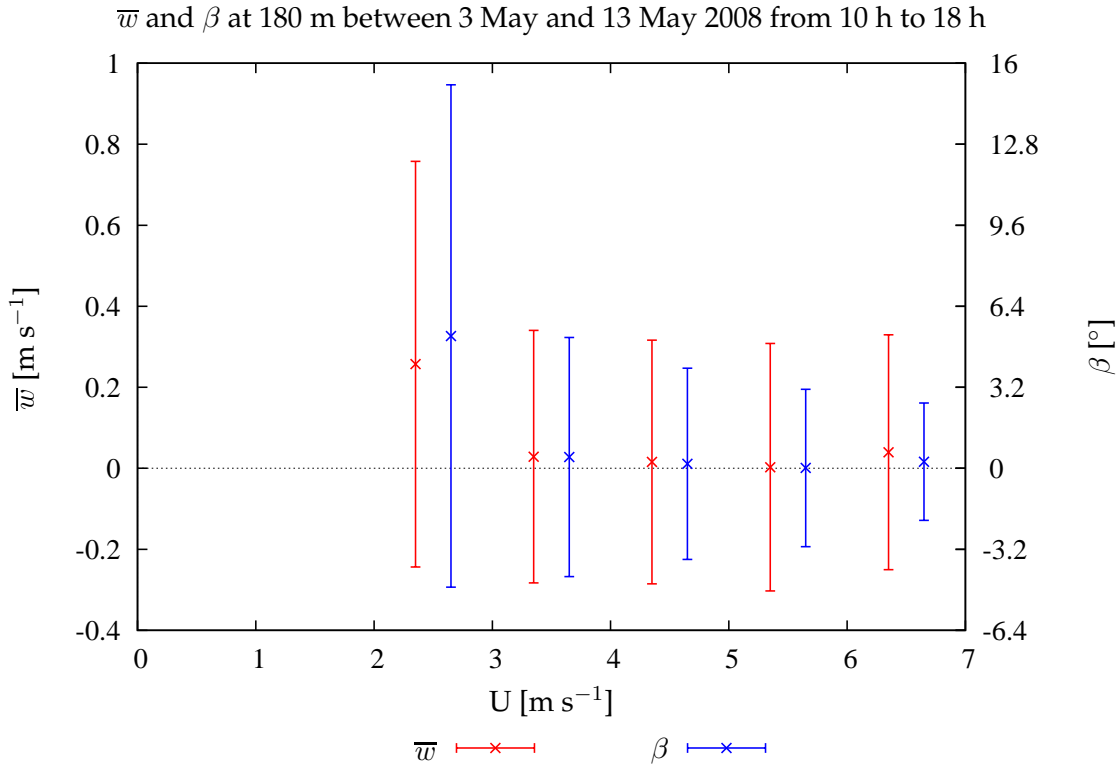
Figure 3.2: In this graph measurement data at 180 m height from the raw data set (Paragraph 3.1) is used. Data is selected from 3rd May until 13th May 2008 and only between 10 h and 18 h local time. For every 10 minutes the average vertical wind velocity, w, horizontal wind velocity, U, and accompanying rotation angle to get zero vertical wind velocity, β, are calculated. The data is sorted into bins by the average horizontal wind velocity. Every bin covers $1\,\mathrm{m\,s^{-1}}$. For each bin, the average and standard deviation of the 10 minute average values of the vertical wind velocity and the rotation angle, are calculated. The standard deviation of the rotation angles is lower for higher horizontal wind velocities.

If data containing low horizontal wind velocities is used to determine β_N, random fluctuations can cause big distortions. This is also indicated by Figure 3.2. The average and standard deviation of the 10 minute averaged vertical wind velocity and rotation are plotted versus the corresponding horizontal wind velocities, binned per $1\,\mathrm{m\,s^{-1}}$. The standard deviation of the rotation angle decreases for increasing horizontal wind velocities. Because of this, only data is considered for which $u \geq 3\,\mathrm{m\,s^{-1}}$ while determining the rotation angles (Bosveld, 2008 - 2009).

3.2.4 The wind tilt correction in practice

In paragraph 3.2.1 the theory of the wind tilt correction is described. However, in practice it is not obvious what the right rotation value is. At the start of this research, it was practice at the KNMI that the rotation angles were calculated over one month (Bosveld, 2008).
In order to check whether rotation angles calculated over one month are trustworthy, the rotation angles are calculated for each month of 2007. Data set (1) (Paragraph 3.1) is used. This data set contains averages over 10 minutes. This data is sorted by wind direction in bins of $20°$. For each bin, the average horizontal and vertical wind velocities are calculated

Monthly wind tilt correction angles at 60 m height in 2007
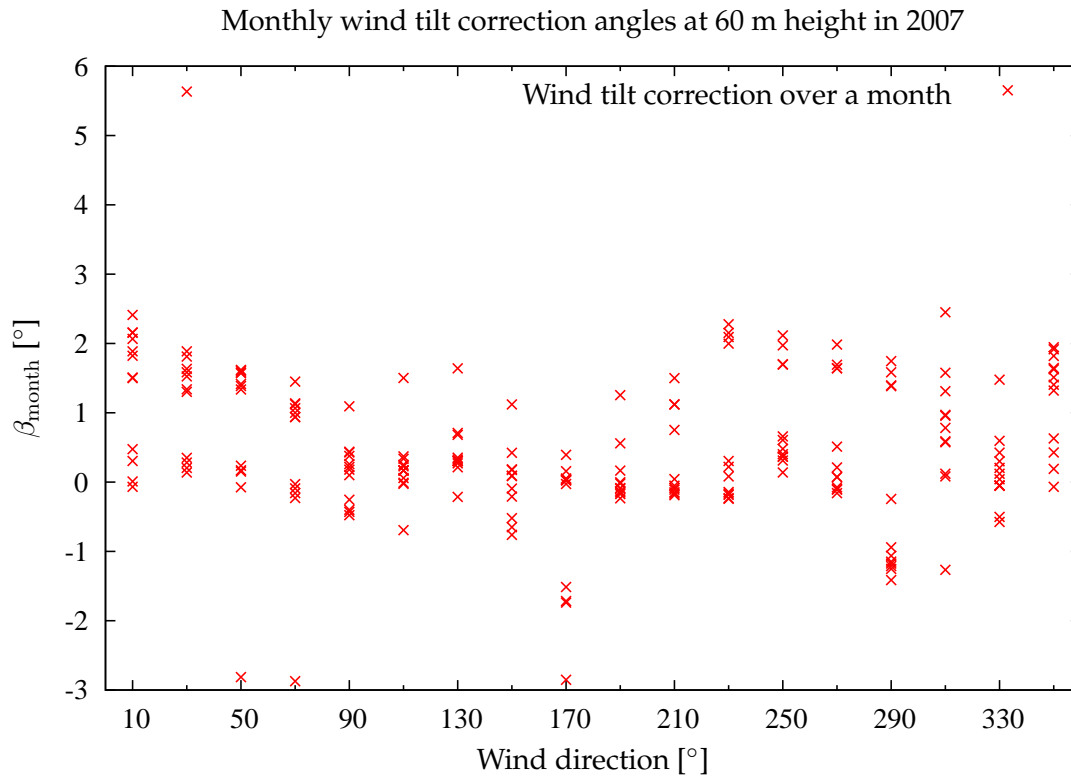
Figure 3.3: For each month in 2007, the calculated rotation angle, β_{month}, for the wind tilt correction is plotted for every wind direction section. Every section has a range of $20°$ and the first one covers $0° - 20°$.

for each month. To calculate the rotation angles, equation (3.8) is used. In Figure 3.3 the resulting angles are plotted for a height of 60 m. The outliers in this figure are not that extreme, but for 100 m and 180 m outliers are present which are many times larger than the average value. This indicates that some months are not suited to be used to determine the rotation angles of the wind tilt correction. The rotation angles calculated for the different months are averaged and their standard deviation as well as the uncertainties of the averages are calculated. These values are plotted in Figure 3.4 for 60 m, 100 m and 180 m height. It can be seen that generally the standard deviations and uncertainties of the rotation angles are of the same order of magnitude as the rotation angles themselves. The magnitude of the annual averaged rotation angles is always lower than $2°$. The magnitude of the maximum rotation angle is $1.5°$ at 60 m, $1.6°$ at 100 m height and $1.4°$ at 180 m height. Because of the spread in monthly calculated rotation angles a wind tilt correction is calculated over a year, from 1st June 2007 to 31st May 2008. This correction is used by the KNMI from now on and can be found in Appendix E.

The variation in monthly rotation angles indicates that if a data set is corrected using a wind tilt correction that is calculated using a year of data, the average vertical wind velocity over a specific month will not be 0. This is checked for May 2008. The data set used is the third data set from the KNMI (Paragraph 3.1). This concerns 10 minute averaged data from May 2008. The aforementioned wind tilt correction calculated over a year is applied in this data. The averages of the vertical wind velocities over May 2008 are given in Table 3.1. The magnitudes of these averages are far greater than the tenths of mm s^{-1} that can be explained
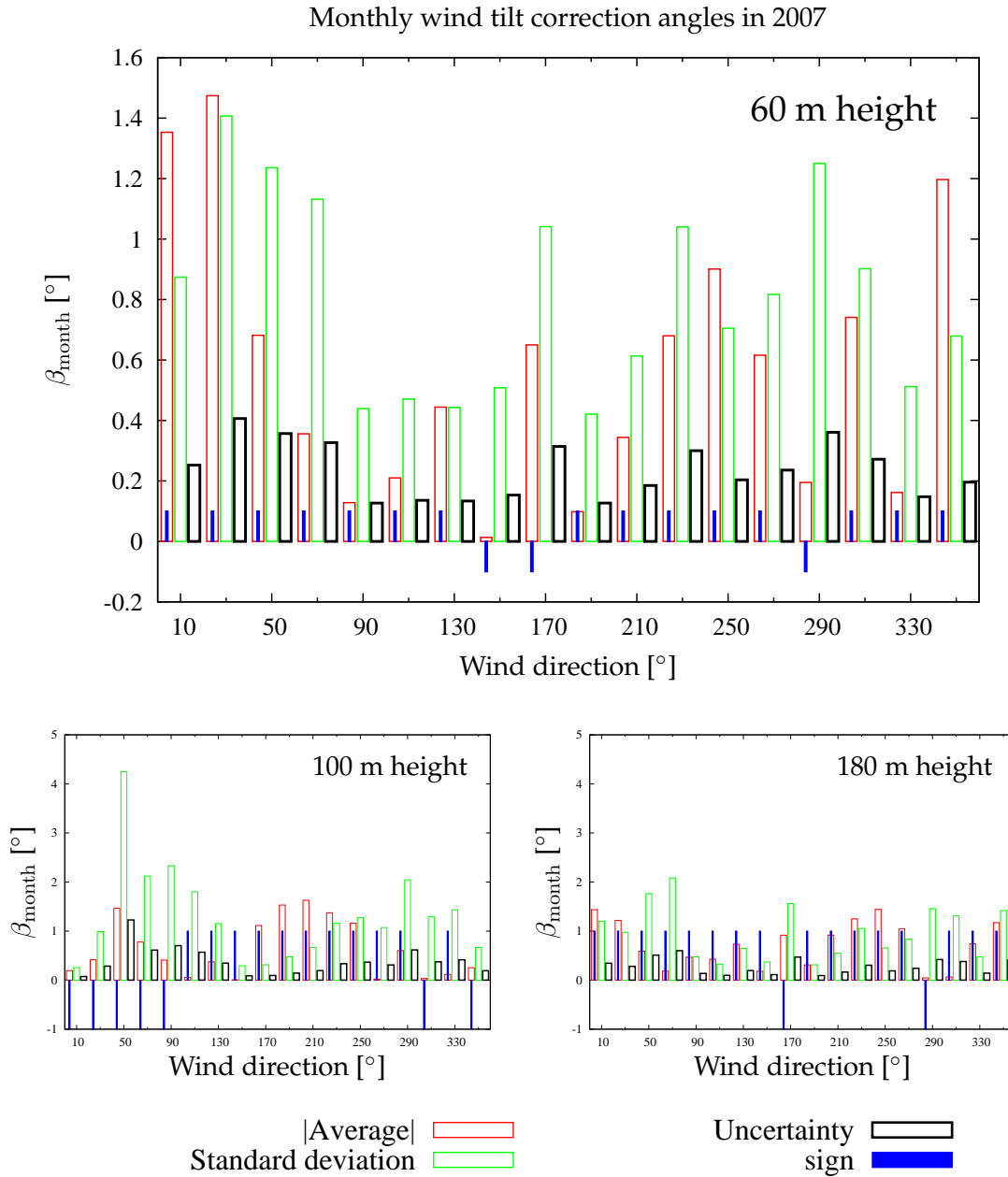
Figure 3.4: The monthly calculated rotation angles for the wind tilt correction in 2007, as displayed in Figure 3.3, are averaged for each wind direction section. The magnitudes of those averages are plotted in red. The blue bars indicate whether the rotation angle is positive or negative. The standard deviation of the monthly rotation angles and the uncertainty of the averages are plotted in green and black, respectively. Results at 60 m height are plotted in the upper graph, results at 100 m height are plotted in the bottom left graph and results at 180 m height are plotted in the bottom right graph.

by the temperature dependent density of air (Webb et al., 1980; Liebethal and Foken, 2003). Considering that the averages of the scalars (for example 300 K) are much higher than the deviations of the scalars (less than 1 K), the advective part of the flux, $\overline{w}\,\overline{\phi}$, will be much larger than the Eddy Covariance flux, $\overline{w'\phi'}$. Therefore it will not be possible to do research on the relation between the Eddy Covariance flux and the total vertical flux using the current measurement setup. The imbalance can not be measured in the field.

3.2.5 The accuracy of flux measurements

In addition to the values of the rotation angles, their influence on the flux measurements has been examined. For eleven days in 2008 (3th May to 13th May) the EC fluxes of CO_2 are examined at 60 m, 100 m and 180 m height in 8 subsequent time periods of half an hour between 12:00 h and 16:00 h local time. These fluxes are calculated for several values of the rotation angle, β. For this examination, the rotation angle is assumed to be equal for all wind directions, because the sonic anemometers are aligned almost perpendicular to the ground. This is checked with the help of spirit levels. Data set (2) from the KNMI (Paragraph 3.1) is used. This contains raw data, which is sampled at 10 Hz. In Figure 3.5 these fluxes are plotted for 4th May 2008 and 12th May 2008. The EC fluxes are normalized by their unrotated values. The outliers are due to very small unrotated EC fluxes. In these graphs and those of the other nine days, it is clear that the EC fluxes are linear dependent on the rotation angle. The averages of the eight fluxes (the black lines) are examined for all days. The average gradient of these fluxes over the eleven days is determined for all 3 heights. Now define

$$f = \frac{\partial \frac{F_{\mathrm{EC},\beta}}{F_{\mathrm{EC},0}}}{\partial \beta} = \frac{1}{F_{\mathrm{EC},0}} \frac{\partial F_{\mathrm{EC},\beta}}{\partial \beta} \tag{3.9}$$

Taking $\mu_{f,\,\mathrm{height}}$, $\sigma_{f,\,\mathrm{height}}$ and $u_{f,\,\mathrm{height}}$ as respectively the average, the standard deviation and the uncertainty of the average of $\frac{\partial F_{\mathrm{EC}}}{\partial \beta}$ at a certain height, it is found that

$$\begin{aligned}
\mu_{f,\,60\,\mathrm{m}} &= 0.024 & \sigma_{f,\,60\,\mathrm{m}} &= 0.007 & u_{f,\,60\,\mathrm{m}} &= 0.002 \\
\mu_{f,\,100\,\mathrm{m}} &= 0.019 & \sigma_{f,\,100\,\mathrm{m}} &= 0.008 & u_{f,\,100\,\mathrm{m}} &= 0.002 \\
\mu_{f,\,180\,\mathrm{m}} &= 0.010 & \sigma_{f,\,180\,\mathrm{m}} &= 0.009 & u_{f,\,180\,\mathrm{m}} &= 0.003
\end{aligned}$$

These results can be used to calculate the EC-flux after rotation relative to the EC-flux without rotation. If $F_{\mathrm{EC},\beta}$ is the EC-flux of CO_2 for a rotation angle β, then

$$F_{\mathrm{EC},\beta} = F_{\mathrm{EC},0} + \frac{\partial F_{\mathrm{EC}}}{\partial \beta} \beta \tag{3.10}$$

Table 3.1: The average vertical wind velocities during May 2008. These results are based on data set (3) from the KNMI (Paragraph 3.1). This consists of 10 minute averaged data which is corrected by the wind tilt correction as given in Appendix E. The average is determined over three selections: all data, data obtained between 8 h and 16 h UTC and data obtained between 0 h and 4 h UTC.

Measurement height	All data	8 h - 16 h UTC	0 h - 4 h UTC
3 m	-0.5 cm s^{-1}	-0.3 cm s^{-1}	-0.5 cm s^{-1}
60 m	-0.9 cm s^{-1}	-1.0 cm s^{-1}	-1.0 cm s^{-1}
100 m	-2.7 cm s^{-1}	-4.0 cm s^{-1}	-2.3 cm s^{-1}
180 m	-0.1 cm s^{-1}	-2.8 cm s^{-1}	1.9 cm s^{-1}

4th May 2008   12th May 2008

Normalized EC flux of CO_2 at 60 m as a function of rotation   Normalized EC flux of CO_2 at 60 m as a function of rotation

Normalized EC flux of CO_2 at 100 m as a function of rotation   Normalized EC flux of CO_2 at 100 m as a function of rotation

Normalized EC flux of CO_2 at 180 m as a function of rotation   Normalized EC flux of CO_2 at 180 m as a function of rotation
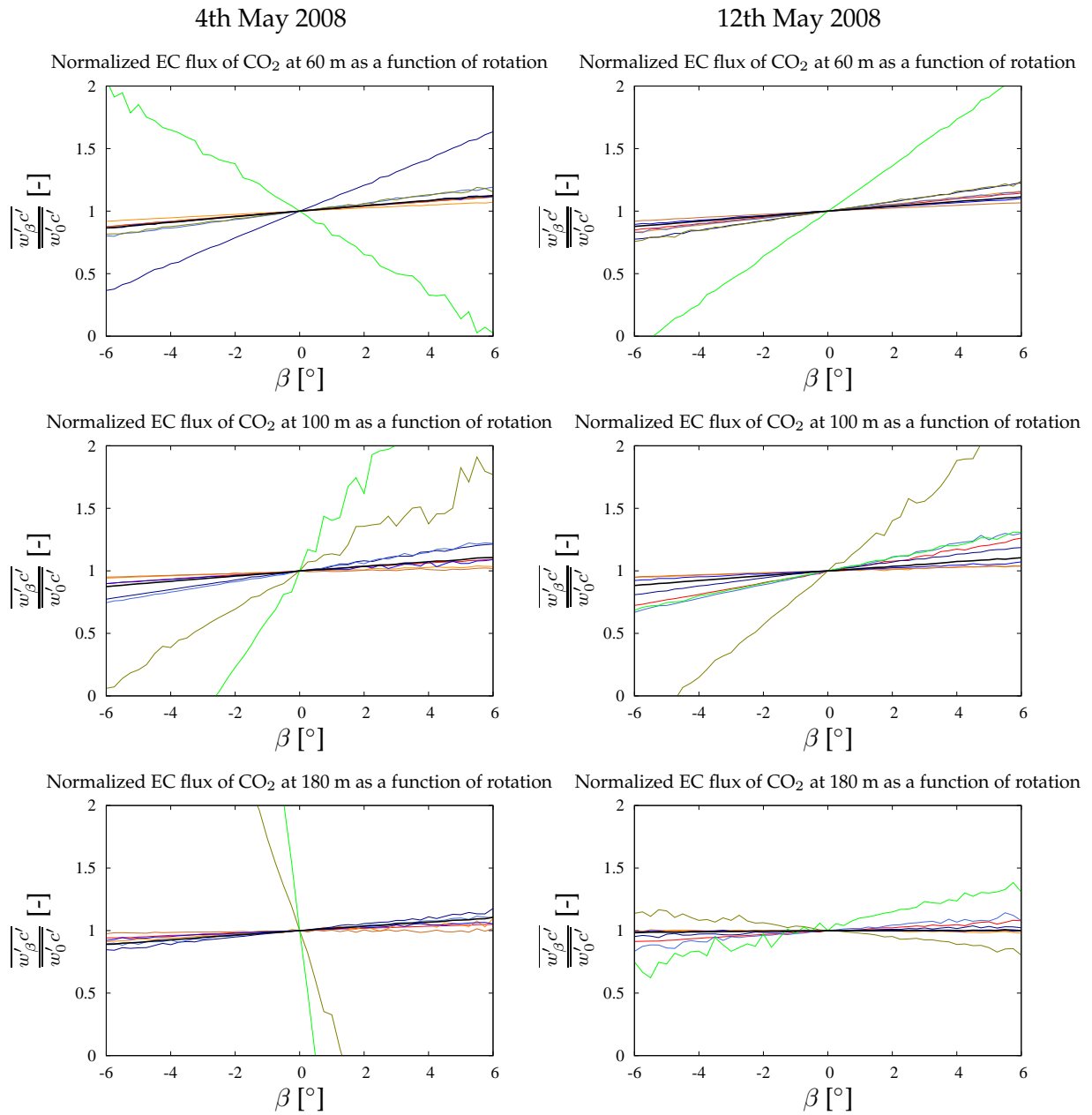
Figure 3.5: In these graphs, the EC fluxes of CO_2 are plotted as a function of the rotation angle, β, for different days and different heights. The left graphs are based on data obtained at 4th May 2008 and the right graphs are based on data obtained at 12th May 2008. The upper row of graphs is based on data measured at a height of 60 m, the middle row of graphs is based on data measured at a height of 100 m and the lower row of graphs is based on data measured at a height of 180 m. In every graph the EC fluxes for 8 succeeding periods, each with a measurement time of 30 minutes, are plotted in different colours. The first period starts at 12:00 h local time. Also the average of the EC fluxes of the 8 periods is plotted as a black line. All plotted data is normalized by the value it would have without rotation. The gradients of the average lines are used to determine the relative change in EC flux when changing the rotation angle of the wind tilt correction. This is the f of Equation (3.9).
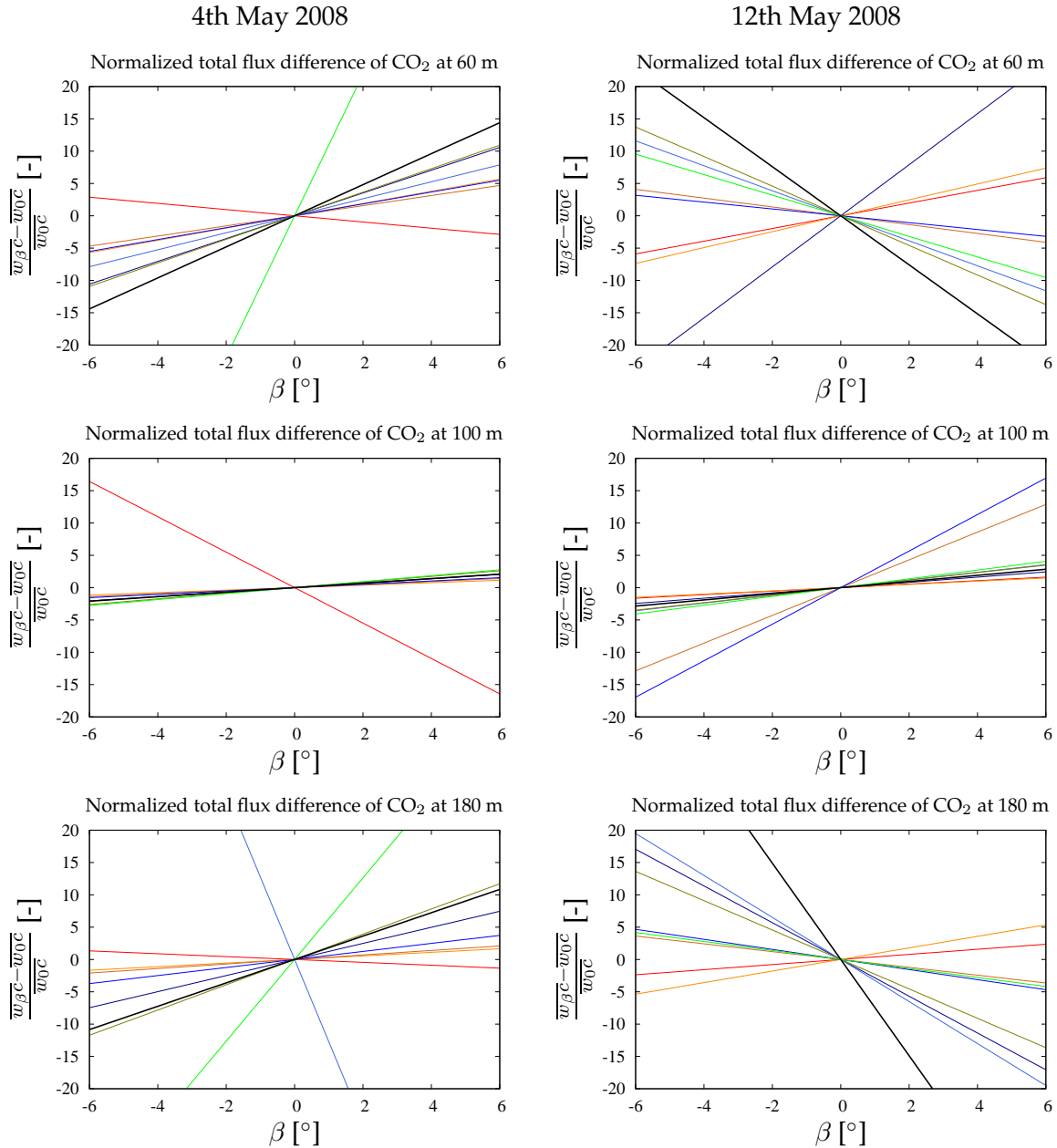
Figure 3.6: In these graphs, the difference between the total fluxes of CO_2 without rotation and with a rotation angle, β, are plotted for different days and different heights. The left graphs are based on data obtained at 4th May 2008 and the right graphs are based on data obtained at 12th May 2008. The upper row of graphs is based on data measured at a height of 60 m, the middle row of graphs is based on data measured at a height of 100 m and the lower row of graphs is based on data measured at a height of 180 m. In every graph the fluxes for 8 succeeding periods, each with a measurement time of 30 minutes, are plotted in different colours. The first period starts at 12:00 h local time. Also the average of the total fluxes of the 8 periods is plotted as a black line. All plotted data is normalized by the total flux without rotation. The gradients of the average lines are used to determine the relative change in total flux when changing the rotation angle of the wind tilt correction. This is the f of Equation (3.9).

Using equation (3.9), this can be rewritten to

$$\frac{F_{\text{EC},\beta}}{F_{\text{EC},0}} = 1 + f\beta \tag{3.11}$$

If the calculated average gradients, f, are used, the deviation of the EC-flux relative to the unrotated EC-flux can be found. The maximum deviation occurs for the maximum rotation angles, which are typically of the order of 2 °, as seen in Paragraph 3.2.4. This gives at 60 m height $\frac{F_{\text{EC},\beta}}{F_{\text{EC},0}} = 1.048$, at 100 m height $\frac{F_{\text{EC},\beta}}{F_{\text{EC},0}} = 1.038$ and at 180 m height $\frac{F_{\text{EC},\beta}}{F_{\text{EC},0}} = 1.020$. So the maximum difference in EC-flux between using a wind tilt correction and not using one is 4.8 % at 60 m height, 3.8 % at 100 m height and 2.0 % at 180 m height. This is only a small difference. Therefore, knowing the rotation angles very exact is not necessary in order to measure EC fluxes. Similar results are found by Lee et al. (2004), who state that for small tilt angles ($|\beta| < 2°$), the tilt error due to these angles is usually less than 5%. However, it should be noted that Lee et al. (2004) uses a planar fit method instead of a wind tilt correction. Twine et al. (2000) also do not perform any coordinate rotations, based on the statement that scalar fluxes are rarely altered by more than 5 % due to coordinate rotations.

The measured Eddy Covariance flux is not very dependent on the rotation angle, so measuring the EC flux with the current measurement setup is no problem. However the same recipe is applied to the total vertical flux. The total vertical flux changes by more than 100 % for every degree of wind tilt correction at every measurement height. As an indication, these dependencies are plotted for 4th May 2008 and 12th May 2008 in Figure 3.6. In these graphs the difference between the flux measured using a rotation angle and the flux measured without rotation, normalized by the latter, is plotted. Since the accuracy of the wind tilt correction angle is several tenths of degrees, the uncertainty of the total vertical flux measured with the current measurement setup is of the same order of magnitude as the total vertical flux itself. This indicates again that total vertical fluxes can not be measured using the current measurement setup.

3.3 The existence of the imbalance in practice

Like shown in the previous paragraph, the imbalance can not be measured with the current measurement setup. However, research can be performed on the behaviour of the vertical wind velocities. The LES results show that the local vertical wind velocities averaged over a long time still are not equal to 0 which causes the flux imbalance. If this behaviour is also present in the measured data, it is likely that the same effects happen in nature as numerical experiments predict. The results can be seen in Figures 3.7 and 3.8. These results are based on data set (2) of the KNMI (Paragraph 3.1). Data that is obtained between 8 h and 16.32 h UTC is selected. The correction angle needed to get the temporal average of all measured vertical wind velocities at a certain height to 0 is determined and applied to the data. Therefore the average vertical wind velocity of the data is forced to be 0 m s^{-1}. However that is not the case for individual measurement periods. The corrected vertical wind velocities are averaged in consecutive blocks of a certain averaging time. For every measurement height this results in a series of temporal averages for that averaging time. This process is repeated for several averaging times and the resulting series of temporal averaged vertical wind velocities are plotted in Figure 3.7. In order to get a clearer view of the spread in temporal averaged vertical wind velocities, the standard deviation of every series is calculated and plotted in Figure 3.8. At 60 m, 100 m and 180 m height, if the averaging time is an hour, the

Realizations of $\overline{w}$ as function of averaging time between 3 May and 13 May 2008
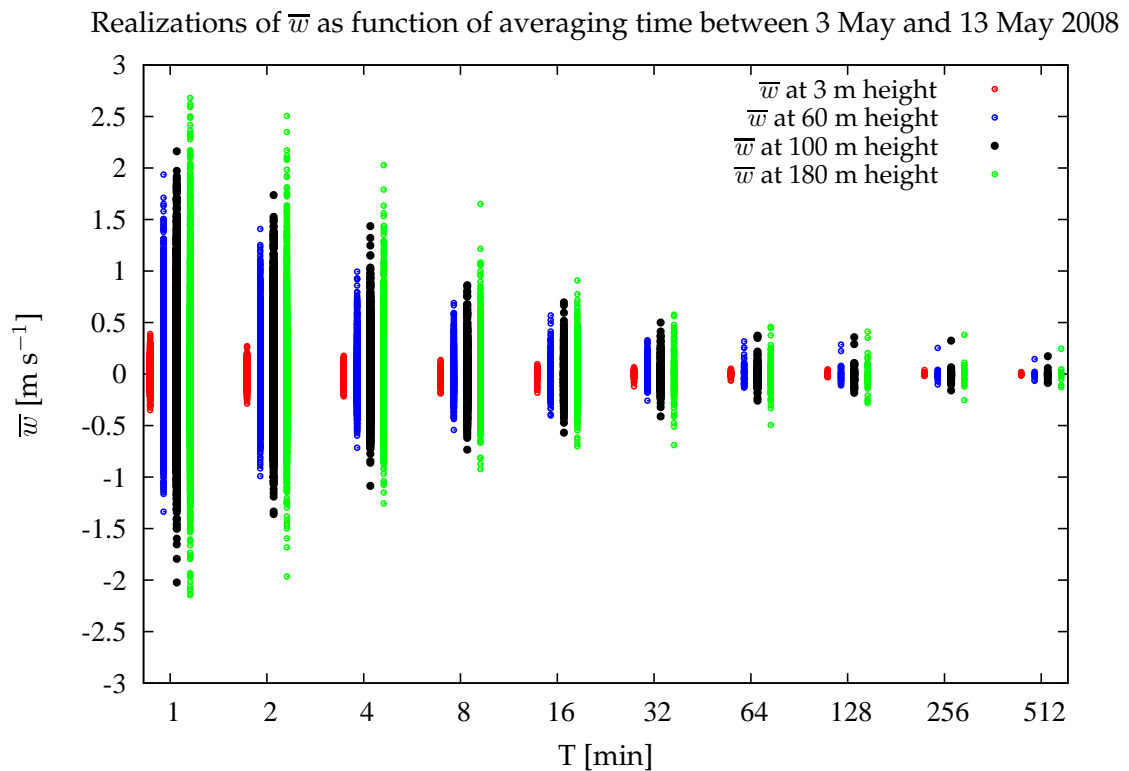
Figure 3.7: Temporal averaged vertical wind velocities plotted against the averaging time. This plot is based on the second data set from the KNMI (Paragraph 3.1) containing raw data sampled at 10 Hz. Only data between 10.00 h and 18.32 h local time is selected. Before calculating the sets of average vertical wind velocities and their standard deviations, a wind tilt correction is calculated using all selected data. This wind tilt correction is used to correct the vertical wind velocities after which they are averaged in consecutive blocks of a specific averaging time. For every measurement height this gives a series of time averaged vertical wind velocities, which is plotted. This is repeated for averaging times of 1 minute to 8 hours and 32 minutes. In present day data analysis averaging times of 30 minutes and 60 minutes are typically used. Therefore the behaviour of $\overline{w}$ at the averaging times of 32 minutes and 64 minutes are particularly interesting. Since all series of time averaged vertical wind velocities cover the complete data set and since the time averaged vertical wind velocity is forced to be 0 over the complete data set by using the wind tilt correction, the average of every series of time averaged vertical wind velocities is equal to 0.
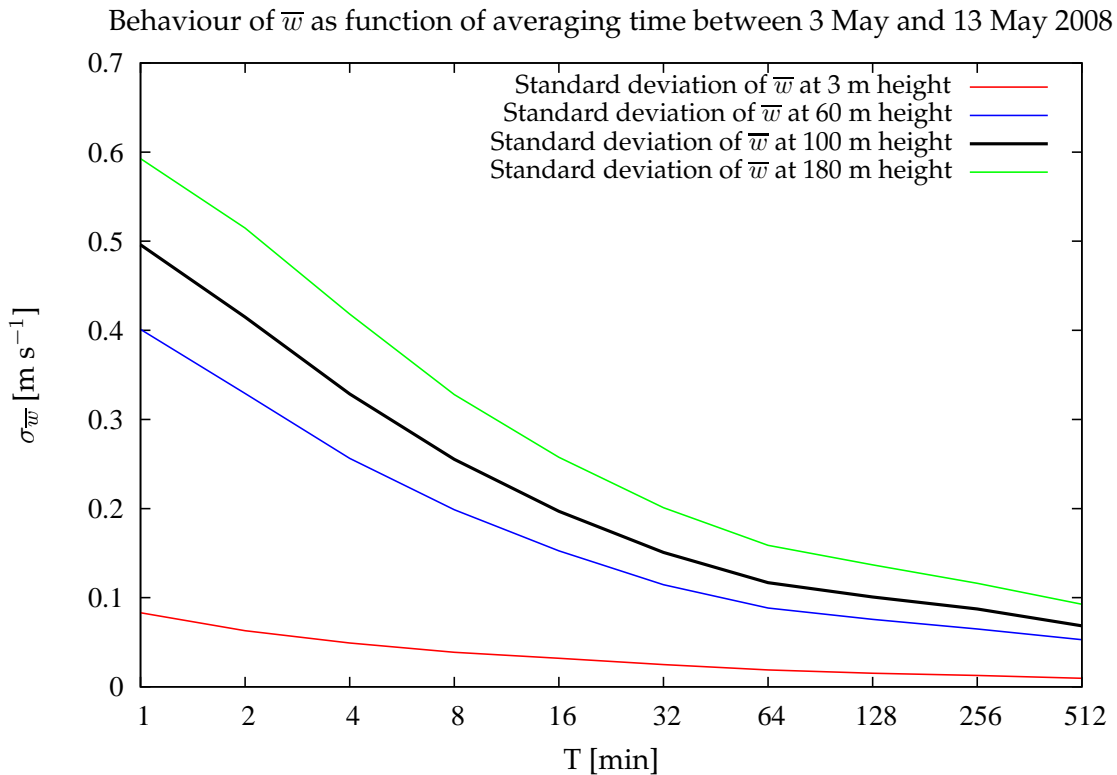
Figure 3.8: Standard deviations of the temporal averaged vertical wind velocities plotted against the averaging time. This plot is based on the second data set from the KNMI (Paragraph 3.1) containing raw data sampled at 10 Hz. Only data between 10.00 h and 18.32 h local time is selected. Before calculating the sets of average vertical wind velocities and their standard deviations, a wind tilt correction is calculated using all selected data. This wind tilt correction is used to correct the vertical wind velocities after which they are averaged in consecutive blocks of a specific averaging time. For every measurement height this gives a series of time averaged vertical wind velocities. The standard deviations of these series are plotted. This is repeated for averaging times of 1 minute to 8 hours and 32 minutes. Since all series of time averaged vertical wind velocities cover the complete data set and since the time averaged vertical wind velocity is forced to be 0 over the complete data set by using the wind tilt correction, the average of every series of time averaged vertical wind velocities is equal to 0.

Behaviour of $\overline{w}$ as function of averaging time between 3 May and 13 May 2008
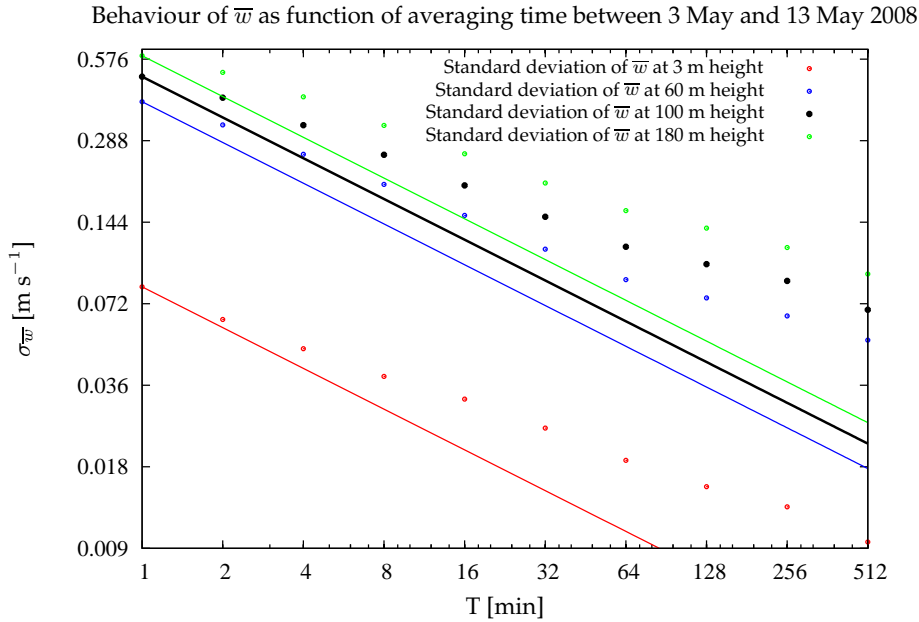

Figure 3.9: Standard deviations of the temporal averaged vertical wind velocities plotted against the averaging time on a log-log scale. This plot is based on the second data set from the KNMI (Paragraph 3.1) containing raw data sampled at 10 Hz. Only data between 10.00 h and 18.32 h local time is selected. The same procedure is used as for Figure 3.8. The lines show how the standard deviations would behave if no correlation would be present. In that case the standard deviation would decrease with the square root of the averaging time.

standard deviation of the collection of time averaged vertical wind velocities is of the order of a tenth m s^{-1}. This indicates that about a third of the measurement blocks has an average vertical wind velocity with a magnitude of 0.1 m s^{-1} or higher. If the averages are taken over a shorter measurement time, this effects gets worse. Figure 3.8 shows that after an hour longer measurements do not improve the standard deviation of the averages by much. The spread in temporal averaged vertical wind velocities is higher for higher measurement heights and decreases for longer averaging times. At 3 m height, the standard deviation is much lower and shorter time scales are visible. The imbalance effect at 3 m height is therefore small as well. Since most literature uses results obtained at a height of 3 m or lower, imbalance effects do not pose a big problem for general flux measurements. According to general statistics the standard deviation of a variable without correlation should decrease with the square root of the amount of samples used to determine its value. In this case the standard deviation should therefore decrease with the square root of the averaging time. In Figure 3.9 it is shown that for all measurement times the standard deviation of the temporal averaged vertical wind velocity decreases slower than that. This indicates that a correlation also exists at larger time scales. This behaviour of the vertical wind velocities is similar to that predicted by LES results. Therefore it is plausible that the imbalance effect witnessed in LES experiments is also present in nature.

Chapter 4

Effects of measurement time

The total vertical flux consists of an advective part and a turbulent part, which is measured using the EC technique. In Chapter 2 it is shown that the advective part of the flux has a non-zero value if the temporal average of the vertical wind velocity during a flux measurement is not 0 m s^{-1}. Since the results from Chapter 3 show that the temporal average of the vertical wind velocity is not 0 m s^{-1}, fluxes measured using the EC technique neglect the advective flux. This effect is small for 3 m height (the height at which most EC measurements are performed), but is important for higher heights (60 m and higher).

In this chapter the EC fluxes will be investigated. The question is: how long should a measurement take in order to get a good representation of the Eddy Covariance flux? An indication will be given about this. In Paragraph 4.1 similarity functions of the turbulent kinetic heat flux and the variance of the vertical wind velocity are compared with observations. Time scales for the turbulent kinetic heat flux are examined in Paragraph 4.2. Both the integral time scale as the time scale derived from Ogives are discussed. The accuracies of EC heat flux measurements over different averaging times are calculated in Paragraph 4.3 using an equation from Businger (1986).

4.1 Similarity functions

In the convective boundary layer, several similarity relations have been derived from observations. The relations for the variance of the vertical wind velocity and the turbulent kinetic heat flux are respectively (Stull, 1988)

$$\frac{\overline{w'^2}}{w_*^2} = 1.8 \left(\frac{z}{z_i} \right)^{\frac{2}{3}} \left(1 - 0.8 \frac{z}{z_i} \right)^2 \tag{4.1}$$

$$\frac{\overline{w'\theta'}}{\overline{w'\theta'}_s} = 1 - \alpha \frac{z}{z_i} \qquad , \qquad 1.2 \leq \alpha \leq 1.5 \tag{4.2}$$

$\overline{w'\theta'}_s$ is the Eddy Covariance heat flux near the surface, the convective velocity, w_*, is given by equation (2.54) and α is 1.2 for cases without precipitation. Equation (4.2) is actually valid for $\overline{w'\theta'_v}$, which is equal to $\overline{w'\theta'}$ if there is no moisture flux. The measurements of the boundary layer height, z_i, are kindly provided by Henk Klein Baltink of the KNMI. He used a wind profiler for his measurements at the Cabauw site. Other measurements originate from the second dataset mentioned in Paragraph 3.1.

The similarity functions of equations (4.1) and (4.2) are examined for different measurement
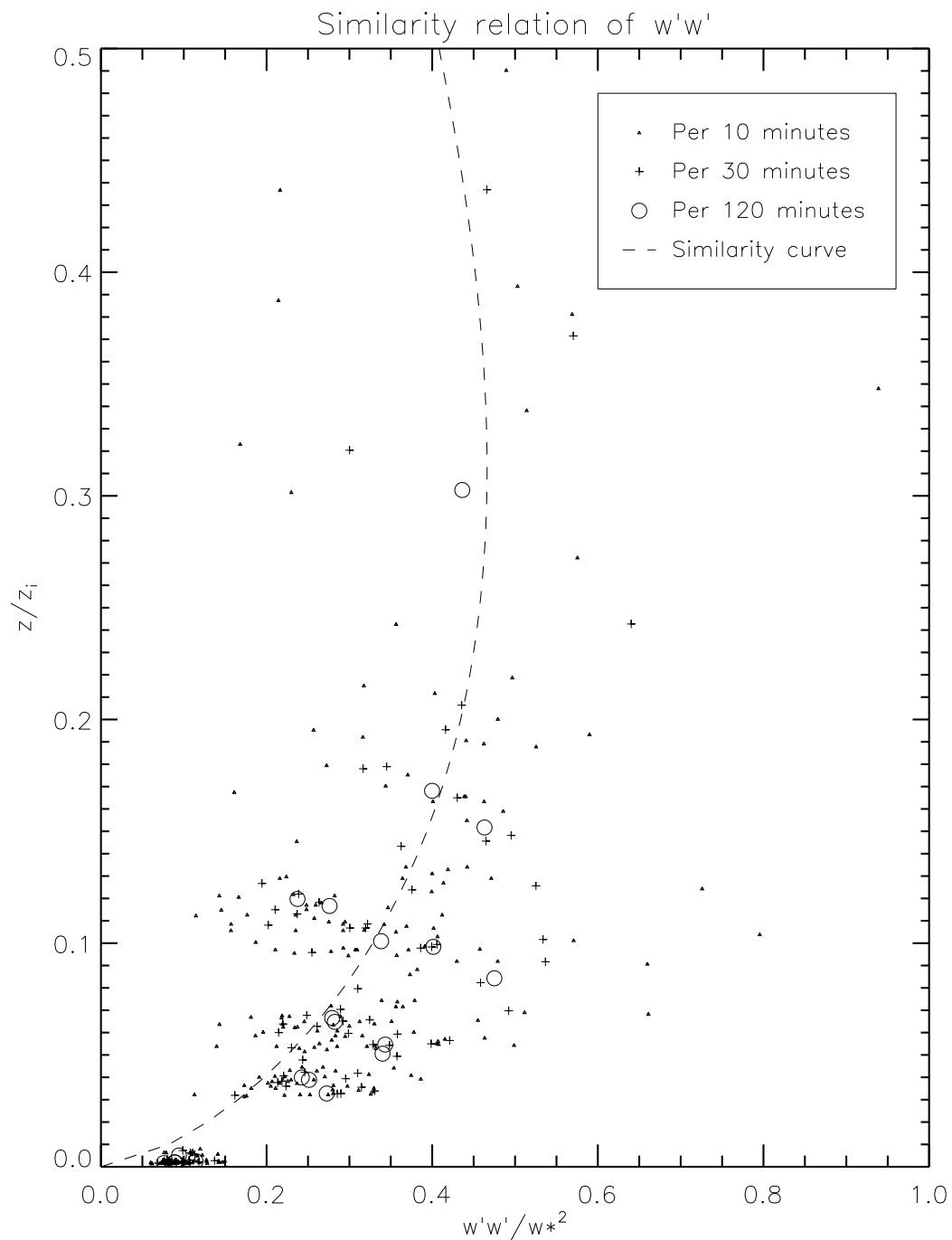
Figure 4.1: In this graph the similarity function of the variance of the vertical wind velocity, as given by equation (4.1), is plotted. Also data measured at 6 May 2008 between 10 h UTC and 14 h UTC, 7 May 2008 between 10 h and 12 h UTC and 8 May 2008 between 10 h UTC and 14 h UTC is plotted. Variables are calculated in blocks of 10 minutes, 30 minutes and 2 hours. The data measured originates from the Cabauw site. The local time is 2 hours later than UTC.
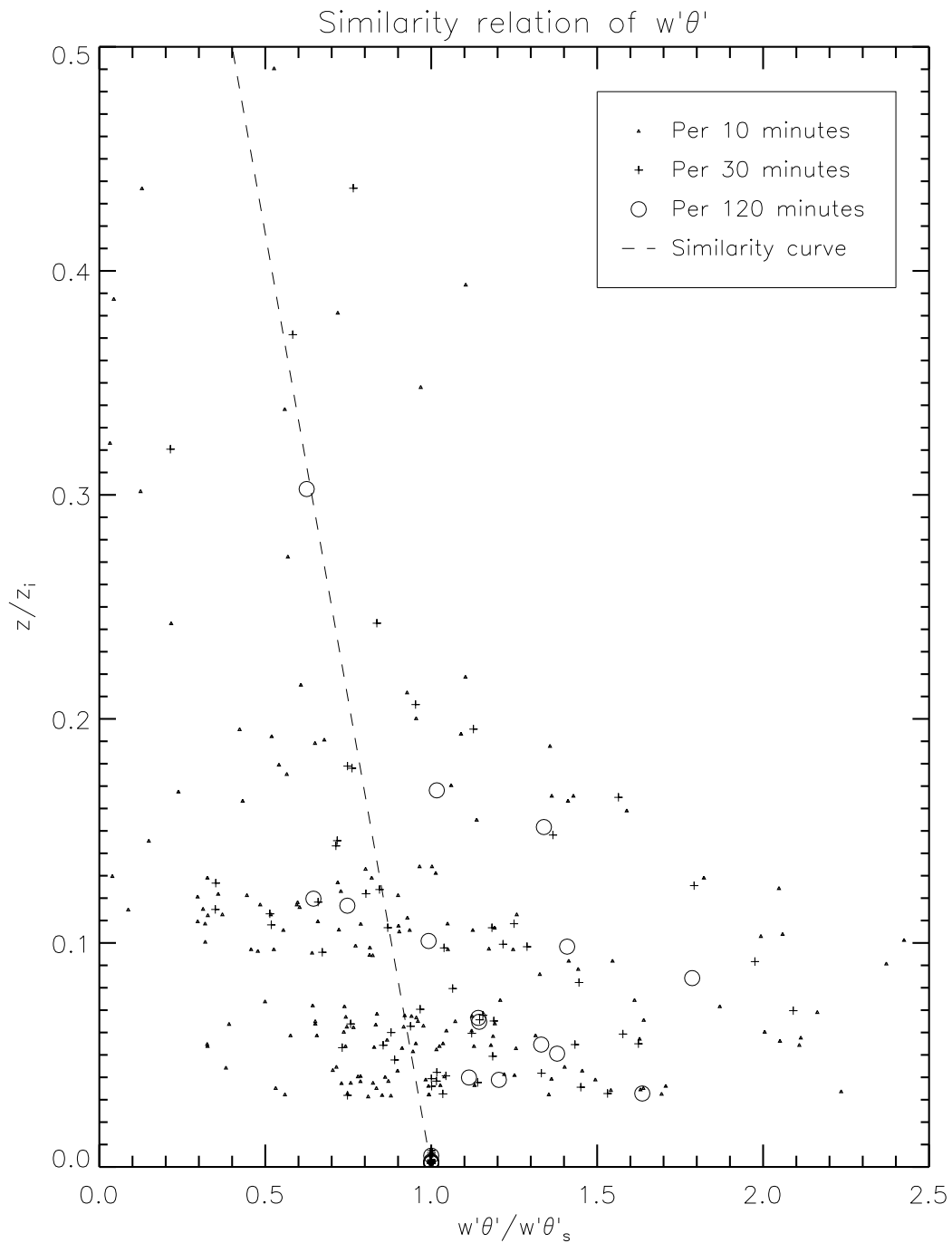
Figure 4.2: In this graph the similarity function of the vertical turbulent heat flux, as given by equation (4.2), is plotted. Also data measured at 6 May 2008 between 10 h UTC and 14 h UTC, 7 May 2008 between 10 h and 12 h UTC and 8 May 2008 between 10 h UTC and 14 h UTC is plotted. Variables are calculated in blocks of 10 minutes, 30 minutes and 2 hours. The data measured originates from the Cabauw site. The local time is 2 hours later than UTC.

times. During periods of 2 hours, variables are calculated and plotted per 10 minutes, per 30 minutes and per 2 hours. Cases with a high heat flux near the ground (higher than 60 W m^{-2}) were selected. The similarity functions are plotted in the same graphs to compare the measurements with the known relations. The data selected originates from:

6 May 2008: between 10 h UTC and 14 h UTC

7 May 2008: between 10 h UTC and 12 h UTC

8 May 2008: between 10 h UTC and 14 h UTC

In Figure 4.1 the variance of the vertical wind velocity plotted according to equation (4.1) can be seen. The values determined over 2 hours lay near the theoretical function. The values determined over 10 minutes have much more spread. This indicates that the values determined over 2 hours give a better representation of the true situation. Even values determined over 30 minutes have quite some spread, which indicates that in order to have good measurements one should measure longer than 30 minutes. The observations at 3 m height are biased to high variances of the vertical wind velocity. This is probably due to wind shear dominating the situation at low altitude. The average horizontal wind velocity at 3 m height is 1.9 m s^{-1}. In Figure 4.2 it can also be clearly seen that the spread for heat fluxes determined over 10 minutes is much higher than the spread for heat fluxes determined over 2 hours. In addition, it can be seen that the heat fluxes at the higher levels (60 m, 100 m and 180 m) do not correspond very well with the theoretical curve. This could be due to the fact that the terrain near the site of Cabauw is not very homogeneous. Near the ground, the only contribution to the heat flux is from the measurement site itself, however at higher levels the heat flux measured comes from a larger area. The general heat flux in the larger area can be different from the local heat flux, whereas the theory assumes homogeneous behaviour over the measured domain. Measuring at higher levels is therefore suited to measure an average heat flux over a large domain, but it is unsuited to measure a local heat flux.

4.2 Time scales

A few definitions of time scales exist. A time scale commonly used is the integral time scale, which will be discussed in Paragraph 4.2.1. Another definition can be the amount of time needed to measure a certain fraction of the total vertical kinematic turbulent flux. This method will be discussed in Paragraph 4.2.2.

4.2.1 Integral time scale

For $\overline{x'y'}$, in which x and y are two arbitrary variables, the integral time scale, $\tau_{x,y}$, is defined as (Lenschow and Kristensen, 1985; Businger, 1986; Lenschow et al., 1994)

$$\tau_{x,y} = \frac{1}{R_{x,y}(0)} \int_0^\infty R_{x,y}(\tau)\mathrm{d}\tau \tag{4.3}$$

in which $R_{x,y}(\tau)$ is the covariance function of variables x and y, dependent on the delay time, τ. The covariance function is given by

$$R_{x,y}(\tau) = \overline{x'(t)y'(t+\tau)} \tag{4.4}$$

The covariance function in equation (4.3) is expected to behave in such a way that for a large τ, $R_{x,y}(\tau)$ goes to 0. In that case, the integral to infinity of equation (4.3) can be calculated by integrating over a finite period. Also the negative correlations should not be too large, since

Table 4.1: The integral time scales for $\overline{T'^2}$, $\overline{w'^2}$ and $\overline{w'T'}$. These time scales are determined for data obtained at 3 May 2008 between 16.00 h and 16.30 h local time. The data comes from the second data set of the KNMI (Paragraph 3.1). The integral time scales are calculated with equation (4.3). The integration is performed from 0 s to 1800 s, since for that range the covariance function is determined.

Height	$\tau_{w,w}$	$\tau_{T,T}$	$\tau_{w,T}$	$\tau_{T,w}$
3 m	0.8 s	-10.5 s	-3.9 s	12.8 s
60 m	-35.5 s	-13.2 s	-45.2 s	6.7 s
100 m	-62.7 s	2.3 s	-169.9 s	83.3 s
180 m	-104.9 s	23.5 s	-337.7 s	41.5 s
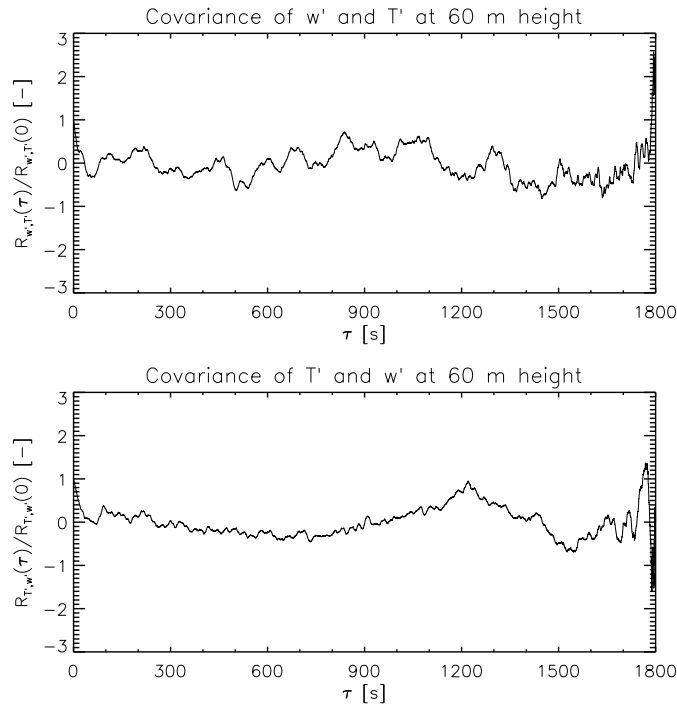
Figure 4.3: Plots of the covariance functions $R_{w,T}$ and $R_{T,w}$ at 60 m height. The covariance functions are calculated using equation (4.4). They are determined for data obtained at 3 May 2008 between 16.00 h and 16.30 h local time. The data comes from the raw data set of the KNMI (Paragraph 3.1).

that could even result in negative time scales. Finally, since $\overline{x'y'} = \overline{y'x'}$, $\tau_{x,y}$ should be equal to $\tau_{y,x}$. However, the integral time scale does not behave this way in practice. To illustrate this, the integral time scales of $\overline{w'T'}$ at 3 May 2008 between 14.00 h UTC and 14.30 UTC are calculated. In Table 4.1 these are given. It can be seen that $\tau_{w,T}$ is by far not equal to $\tau_{T,w}$ and some resulting time scales even become negative. This is caused because the covariance functions do not behave as nice as expected. This can be seen in Figures 4.3 , 4.4 and 4.5. For example, the covariance function can be smaller than 0 on average, as can be clearly seen in the upper graph in Figure 4.5. This is caused by the very negative covariance at a high τ. At a high τ, fewer values are present to determine the expected values in equation (4.4). Therefore the graphs are less certain for high τ values than they are for low τ values. These uncertain values of $R(\tau)$ should not be considered when determining the time scale.

In order to fix this problem it is common to integrate equation (4.3) until the first zero-crossing of the covariance function instead of infinity (e.g., Camp and Shin, 1995; Barrett and Hollingsworth, 2001). However, in this case this will only solve the occurrence of negative
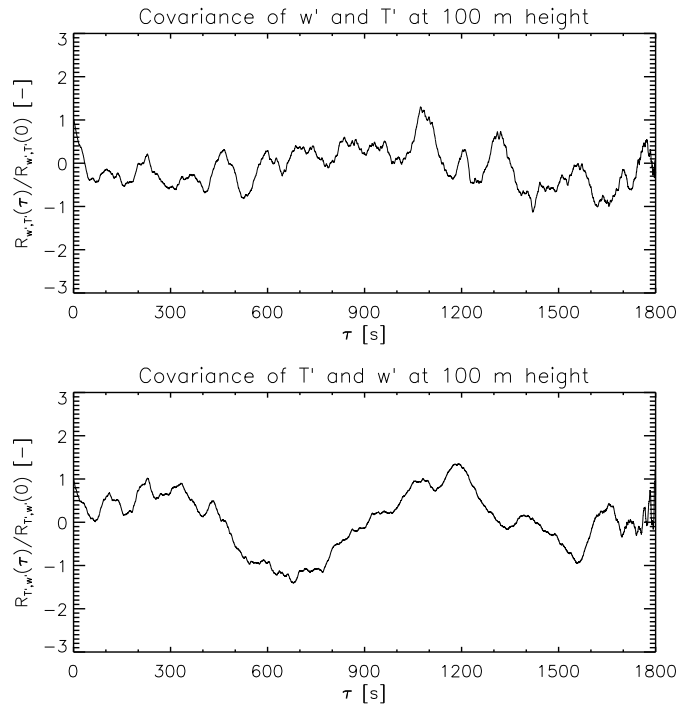
Figure 4.4: Plots of the covariance functions $R_{w,T}$ and $R_{T,w}$ at 100 m height. The covariance functions are calculated using equation (4.4). They are determined for data obtained at 3 May 2008 between 16.00 h and 16.30 h local time. The data comes from the raw data set of the KNMI (Paragraph 3.1).
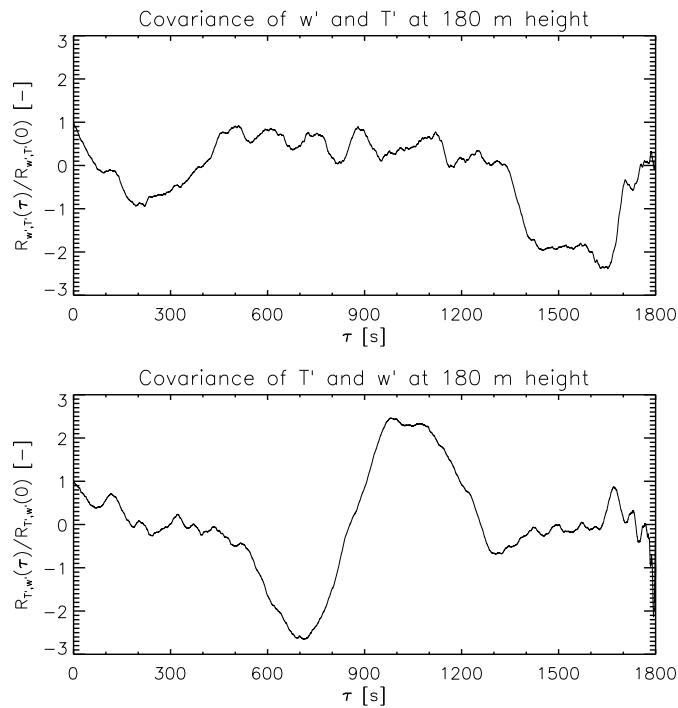
Figure 4.5: Plots of the covariance functions $R_{w,T}$ and $R_{T,w}$ at 180 m height. The covariance functions are calculated using equation (4.4). They are determined for data obtained at 3 May 2008 between 16.00 h and 16.30 h local time. The data comes from the raw data set of the KNMI (Paragraph 3.1).

time scales. It is not always very clear if a zero-crossing is present. In the bottom graph of Figure 4.3 a zero crossing is only just achieved before the covariance rises again. However in the bottom graph of Figure 4.4 the covariance only approaches 0 after about 60 seconds and goes up again before becoming 0. The first zero-crossing in this graph is after about 450 seconds. These just or just-not zero-crossings show that this method is not suited to determine an objective time scale. In addition to that, $\tau_{w,T}$ is still not equal to $\tau_{T,w}$ when integrating to the first zero-crossing. This can be clearly seen in the two graphs of Figure 4.5. Because of these problems, the integral time scale is not evaluated in this thesis.

4.2.2 Ogives

A possible definition of the time scale is the amount of time needed to measure a certain fraction of the total vertical kinematic turbulent flux. The total vertical kinematic turbulent flux has to be determined over quite a large period. The time scale that is researched in this Paragraph is called the Ogive time scale (Desjardins et al., 1989; Oncley et al., 1996). The Ogive time scale of $\overline{x'y'}$, in which both x and y can be any variable, is denoted by $T_{Ogive,x,y}$. It is based on a spectral analysis of the measured data. Detailed information about this technique is given by Stull (1988). A short summary wil be given in this thesis.
The time series of data are discrete and can be decomposed into a frequency spectrum using a fourier transform. This representation makes it possible to study the effects on different time scales and to see which time scales are dominant. The transform of time series $x[k]$, in which N samples of data are measured during time T with time intervals of Δt, is given by

$$F_x(n) = \sum_{k=0}^{N-1} \left(\frac{x[k]}{N} e^{\frac{-i2\pi nk}{N}} \right) \tag{4.5}$$

$$f(n) = \frac{n}{T} \tag{4.6}$$

$$N = \frac{T}{\Delta T} \tag{4.7}$$

$$n_f = \frac{N}{2} \tag{4.8}$$

In which n_f is called the Nyquist frequency and f is the frequency in Hz. The discrete spectral energy is defined by

$$\begin{aligned} E_x(0) &= |F_x(0)|^2 \\ E_x(n) &= 2 \cdot |F_x(n)|^2 & 1 \leq n < n_f \\ E_x(n_f) &= |F_x(n_f)|^2 & n_f \in \mathbb{N} \end{aligned} \tag{4.9}$$

This spectral energy is actually a special case of the cospectrum, $E_{x,y}$. It is composed out of the cross spectrum, $C_{x,y}$, which is defined by

$$C_{x,y}(n) = F_x^*(n) \cdot F_y(n) \tag{4.10}$$

The cospectrum is the real part of the cross spectrum. Since the cospectrum at n is equal to the cospectrum at $N - n$, $C_{x,y}(n)$ and $C_{x,y}(N - n)$ are added to each other. The resulting spectrum until the Nyquist frequency is a representation of the cospectrum. It is described

by

$$E_{x,y}(0) = \Re\left[C_{x,y}(0)\right] = \Re\left[F_x^*(0) \cdot F_y(0)\right]$$
$$E_{x,y}(n) = \Re\left[C_{x,y}(n) + C_{x,y}(N-n)\right] = 2 \cdot \Re\left[F_x^*(n) \cdot F_y(n)\right] \qquad 1 \le n < n_f$$

(4.11)

$$E_{x,y}(n_f) = \Re\left[C_{x,y}(n_f)\right] = \Re\left[F_x^*(n_f) \cdot F_y(n_f)\right]$$

The cospectrum describes the contribution to the covariance of two variables at all frequencies. The sum of all cospectral amplitudes is equal to the covariance.

$$\overline{x'y'} = \sum_{n=1}^{n_f} E_{x,y}(n) \tag{4.12}$$

Since n is related to the frequency by $f = \frac{n}{T}$, equation (4.12) can be rewritten to

$$\overline{x'y'} = \sum_{f=\frac{1}{T}}^{\frac{n_f}{T}} E_{x,y}(f) \tag{4.13}$$

in which f increases by $\frac{1}{T}$ for every step. The Ogive (Desjardins et al., 1989; Oncley et al., 1996) represents the summation of the cospectrum, starting at the frequency at which the Ogive is evaluated and ending at the Nyquist frequency. It is given by

$$Og(f) = \sum_{f'=f}^{\frac{n_f}{T}} E_{x,y}(f') \tag{4.14}$$

In integral form this is equal to

$$Og(f) = T \int_f^{\frac{n_f}{T}} E_{x,y}(f') \mathrm{d}f' \tag{4.15}$$

If the Ogive is normalized by the covariance, its value at a certain frequency shows the fraction of the covariance measured when taking into account the frequencies equal to or higher than that frequency (Desjardins et al., 1989). The time needed to measure contributions of that frequency and higher frequencies is equal to 1 divided by that frequency. This can be used to examine how long one should generally measure in order to measure a certain percentage of the covariance, assuming that the covariance converges for a certain averaging time. Since the frequencies are $\frac{1}{T}$ apart, the individual resulting data points all are $\frac{T}{n}$ in which T is the time over which the energy spectrum is calculated and n is an arbitrary integer. In this thesis the technique is used to examine the time needed to cover 90 % of $\overline{w'T'}$. If data is examined over a time that is not equal to 0.1 s times a power of 2, a subset is taken to fulfill that condition. This is necessary for the calculation of the fourier transform. A few resulting Ogives are shown in Figure 4.6. The aim of the measurements is to determine the flux without the interference of the diurnal cycle. Because of this diurnal cycle, the air heats or cools. The change in temperature is approximately linear with time if the time frame is not chosen too long. In order to obtain the undisturbed results, the data concerning the temperature is detrended. This technique consists of a linear regression of the temperature data during the time frame investigated. The linear regression is then subtracted from the data.
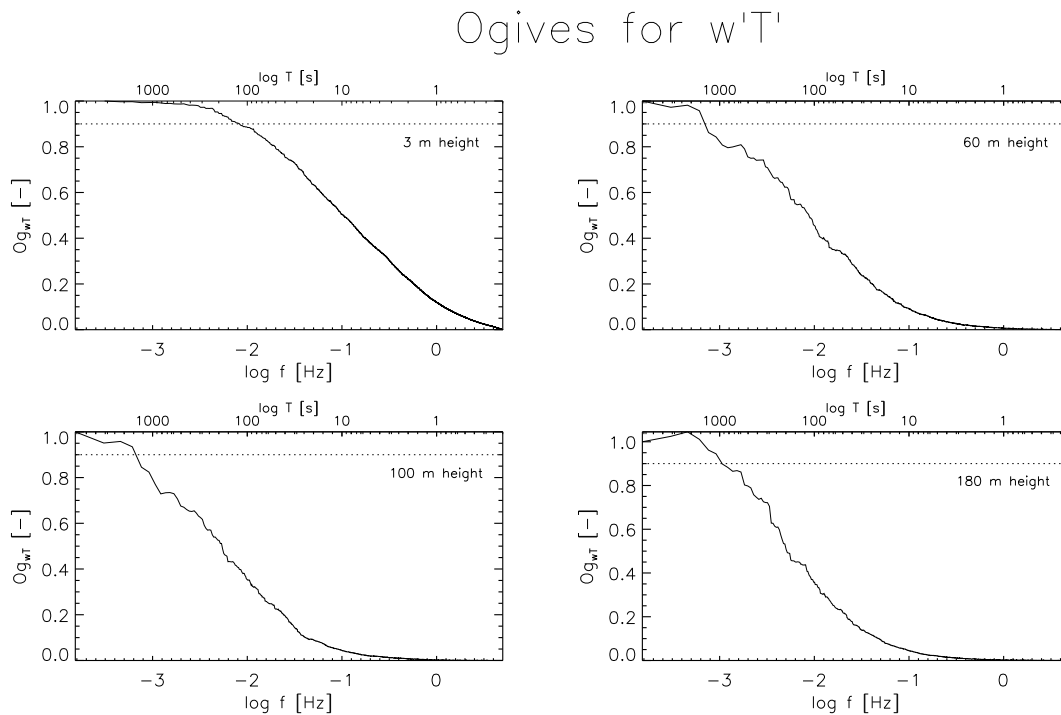
Figure 4.6: Ogives for $\overline{w'T'}$ at 6 May 2008 between 12 h and 14 h local time. The dotted line indicates 90 % of the total covariance. The frequency at the intersection between the dotted line and the Ogive is the lowest frequency that has to contribute in the measurement of the EC flux in order to measure at least 90 % of the total turbulent kinematic flux. These graphs are based on the raw data set of the KNMI (Paragraph 3.1) which contains data sampled at 10 Hz.

The investigated time scale needed to cover 90 % gives an indication how long one should measure to neglect on average only 10 % of the total turbulent flux. As can be seen in Figure 4.6, the covariance grows for lower frequencies and correspondingly longer measurement times. Therefore if measurements would be performed during time frames corresponding to the resulting time scales, the resulting turbulent fluxes should be corrected by a factor of $\frac{10}{9}$ to compensate for the fact that on average only 90 % is measured.

Resulting time scales can be found in Table 4.2. The results are based on the second dataset of the KNMI (Paragraph 3.1) which contains data from 3 May until 13 May 2008, sampled at 10 Hz. Data is evaluated in blocks of 1 hour and in blocks of 2 hours. Results for three conditions are selected and averaged. The three selections are:

(1) All data
(2) Data between 10 h and 16 h UTC
(3) Convective circumstances: a surface heat flux higher than 60 W m^{-2}

The time scales determined over 2 hours are generally larger than those determined over 1 hour. This is due to the fact that the data sets of 2 hours contain contributions of frequencies that are not present in the data sets with a length of 1 hour and generally the covariance grows when lower frequencies are also considered. The time scales at 3 m height indicate that flux measurements of 10 minutes cover all heat flux. However, at 60 m height flux measurements should be performed in blocks of at least 30 minutes. At 100 m and 180 m height, the time scale is even larger than 30 minutes. Therefore, flux measurements over an hour should be performed to cover the turbulent flux.

In addition to looking at the averages of the Ogive time scales, also the time scales of the average Ogives are examined. For every measurement height, the non-normalized Ogives are added to each other for data between 10 h and 16 h UTC. The Ogives are then normalized by dividing by the added covariances. Using these results, the time scales of the average Ogives are determined. These show how long EC flux measurements should take in order to neglect only 10 % of the total turbulent flux if all separate EC fluxes are averaged. These results are shown in Table 4.3. Once more, the time scales determined over blocks of 2 hours are larger than those determined over 1 hour. The time scale at 3 m, shows again that fluxes calculated over 10 minutes cover the total turbulent flux. However, even if averaging all the fluxes over 11 days between 10 h and 16 h UTC, measurements at 60 m and 100 m height should be performed in blocks of at least 20 minutes to measure 90 % of the total turbulent flux. At 180 m height one even has to perform measurements in blocks of at least half an hour to get that result.

In general, the results show that flux measurements over 10 minutes are adequate to determine the total turbulent flux at 3 m height. However, at 60 m, 100 m and 180 m height fluxes should be determined over at least half an hour in order to measure a big part of the total turbulent flux.

4.3   Accuracy

The accuracy with which an Eddy Covariance flux is measured is treated by Businger (1986). He assumes that the ensemble average can be represented by the Eulerian point average. This might not be true, since temporal averages are not necessary equal to spatial averages as shown in Chapter 2. Still, since only the accuracy of the Eddy Covariance flux is investigated, their result should be a good indication. The accuracy of an Eddy Covariance flux measurement, a, is given by

$$a = \sqrt{2 \frac{\tau_{w,T}}{T_{\mathrm{meas}}} \frac{\overline{(w'T')^2} - \overline{w'T'}^2}{\overline{w'T'}^2}} \tag{4.16}$$

in which T is the temperature and T_{meas} is the measurement time. $\tau_{w,T}$ is the integral time scale as discussed in Paragraph 4.2.1. Businger (1986) estimates the integral time scale as the time it takes for the dominant eddy to pass over the point of observation. This results in

$$\tau_{w,T} = \frac{l_e}{\overline{u}} \tag{4.17}$$

Table 4.2: Averaged Ogive time scales at all four measurement heights for different selections of data. Ogive time scales are calculated over blocks of 1 hour length and over blocks of 2 hours length. The three selections are: all data, data between 10 h and 16 h UTC and convective circumstances. Convective circumstances are assumed for situations in which the surface heat flux is at least 60 W m^{-2}. The results are based on the second dataset of the KNMI (Paragraph 3.1) which contains data from 3 May until 13 May 2008, sampled at 10 Hz.

Height	Time scale over 1 hour			Time scale over 2 hours		
	All data	10 h - 16 h UTC	Convective	All data	10 h - 16 h UTC	Convective
3 m	229 s	173 s	171 s	549 s	170 s	168 s
60 m	650 s	1010 s	1171 s	1521 s	1697 s	1704 s
100 m	1150 s	1221 s	1258 s	2642 s	2082 s	2016 s
180 m	1434 s	1346 s	1263 s	3473 s	2357 s	1977 s

Table 4.3: Ogive time scales of averaged flux measurements at all four measurement heights. Data measured between 10 h and 16 h UTC is selected. The data originates from the second dataset of the KNMI (Paragraph 3.1) which contains data from 3 May until 13 May 2008, sampled at 10 Hz. Ogives are calcuated over blocks of 1 hour length and over blocks of 2 hours length. At every height all Ogives are added to each other and normalized by dividing by the added covariances.

Height	Time scale over 1 hour blocks	Time scale over 2 hour blocks
3 m	148 s	159 s
60 m	819 s	1092 s
100 m	1092 s	1310 s
180 m	1092 s	1638

Table 4.4: The accuracies of a single Eddy Covariance flux measurement. The accuracies are determined according to equation (4.19) using the second dataset of the KNMI (Paragraph 3.1). The accuracies are determined for flux measurements with a length of 10 minutes, half an hour and an hour.

Height	$a_{10\,\text{minute fluxes}}$	$a_{\text{half hour fluxes}}$	$a_{\text{hour fluxes}}$
3 m	47.7 %	27.5 %	19.5 %
60 m	165.9 %	95.8 %	67.7 %
100 m	237.6 %	137.2 %	97.0 %
180 m	346.2 %	199.9 %	141.3 %

in which l_e is the size of the dominant eddy. He concludes from the dimensionless spectra given by Kaimal et al. (1972) that typically

$$l_e \approx 10z \tag{4.18}$$

Equations (4.16), (4.17) and (4.18) result in

$$a = \sqrt{\frac{20z}{T_{\text{meas}}\overline{u}} \frac{\overline{(w'T')^2} - \overline{w'T'}^2}{\overline{w'T'}^2}} \tag{4.19}$$

The accuracy expresses the relative uncertainty of a single Eddy Covariance flux measurement. Using the second dataset of the KNMI (Paragraph 3.1), accuracies are calculated for fluxes determined over different averaging times. The averaging times investigated are 10 minutes, half an hour and an hour. For every averaging time this is done by calculating the factor $\frac{20z}{T_{\text{meas}}\overline{u}} \frac{\overline{(w'T')^2} - \overline{w'T'}^2}{\overline{w'T'}^2}$ for consecutive blocks during an hour. This is done for every hour in which convective circumstances are present. In this case this means a turbulent kinetic surface heat flux determined over an hour of at least 50 K m s^{-1}. After the calculation of all factors, the outliers are removed and the remaining factors are averaged. These averaged factors are used to calculate the accuracies. Results are shown in Table 4.4. The same technique is used using flux measurements of two hours. In that case the accuracies become slightly better.

According to these results a single flux measurement is not very trustworthy, even if it concerns a flux measured over an hour. However, the accuracy does not predict a bias, so if one averages over many fluxes the accuracy will improve. Another remark could be made about the substitution for the integral time scale. At higher heights, Businger's approximation that $l_e \approx 10z$, could be an overestimation for the eddy size. Another approximation that is used often is $l_e \approx z$. If the eddy size at higher measurement points would be equal to z, the accuracies would improve by a factor larger than 3.

Chapter 5

Conclusions and Recommendations

5.1 Conclusions

Emissions of heat and scalars are determined by measuring fluxes. The total flux consists of an advective part and a turbulent part. The Eddy Covariance technique measures only the turbulent flux. The advective flux is assumed to be zero due to a temporal averaged vertical wind velocity of 0 m s^{-1}. However, in literature it is found that locally the temporal averages of the vertical wind velocity is non-zero, which leads to a bias in the determined fluxes. This is called the flux imbalance. The flux imbalance is investigated both theoretically and from observations. In the observations data from 3 m, 60 m, 100m and 180 m height are evaluated.

Using the assumption that vertical wind velocities and scalar concentrations are distributed periodically, a theoretical imbalance effect is calculated for a specific case. The functions of both quantities are described by only one sinusoid and both periodicities are equal. Like the imbalance from LES results, the average value of this imbalance is negative, which indicates an underestimation of the total vertical flux if Eddy Covariance fluxes are measured. This theoretically derived imbalance suggests that the flux imbalance effect is not an artifact of the LES models.

In observations, the sonic anemometer may have a slight tilt and the wind is disturbed due to the sonic anemometer and the platform on which it is standing. The wind tilt correction angles used to correct measured wind velocity data for these effects, are determined over some period. It is shown that if these correction angles are determined over a month, the calculated correction angles vary much from month to month. On the basis of these findings, wind tilt correction angles are now calculated using data obtained over a year.

The spread in monthly calculated wind tilt correction angles is of the order of a degree. This indicates that the wind tilt correction calculated over a year might not be entirely correct, but be off with a few tenths $^{\circ}$. Results show that this barely influences the EC fluxes. Therefore EC flux measurements can be determined without a problem with the current measurement setup. However, a small change in wind tilt correction angles causes a large change in the measured advective flux and therefore also in the measured total flux. This is due to the fact that the horizontal wind velocity partly goes into the rotated vertical wind velocity. The uncertainty in the wind tilt correction results in an uncertainty of the flux which is of the same order of magnitude as the determined value of the flux. Therefore the total vertical flux can not be measured using the current measurement setup and research on the flux imbalance in practice can not be performed.

Even if the wind tilt correction angles determined over a year would be determined perfectly, the flux imbalance can not be determined, because after correction with those wind tilt correction angles the vertical wind velocities averaged over a month are not near 0. These averaged velocities are of the same order of magnitude as the temporal deviations of the vertical wind velocity with respect to the mean. The temporal averages of the scalars are much higher than the temporal deviations of the scalars. Because of this the measured advective part of the flux is much larger in magnitude than the Eddy Covariance flux and the measured imbalance will be near -1. Because of these problems the imbalance in observations can not be determined.

Although the imbalance can not be determined directly, research is performed on the behaviour of the vertical wind velocities. The fact that locally the temporal averaged vertical wind velocities is not 0, as shown in LES results, is the basis for the imbalance effect. For observations it is shown that the vertical wind velocity behaves this way too. The spread of the vertical wind velocities is determined for different heights and averaging times. The standard deviation decreases with the averaging time, but slower than expected for uncorrelated data. Since the vertical wind velocities behave the way LES results predict, it is likely that for observations the imbalance also exists as predicted. The spread in vertical wind velocities increases with the measurement height. At 3 m height, the effect is relatively small compared to the results at 60 m height and higher. This indicates that although the flux imbalance is important for higher measurement heights, observations at lower heights (below 5 m) are not influenced much by it.

Using Eddy Covariance measurements, the advective kinematic flux can not be measured since the mean vertical wind velocity can not be determined precise enough. Therefore, the imbalance can not be prevented. However, the deviation from the actual spatially averaged vertical turbulent flux can be diminished by measuring the Eddy Covariance fluxes over longer periods. The longer the averaging period, the larger the time scales that are included in the measurements. Results show that flux measurements over 10 minutes are adequate at 3 m height. However at 60 m height and higher, measurements should be performed over longer periods. Fluxes should be determined over at least 30 minutes, but an hour would give noticeable better results. A possible problem with long measurement times is the non-stationary situation due to mean trends caused by the diurnal cycle.

5.2   Recommendations

Since the vertical kinematic advective flux can not be measured in the field by using the current measurement setup, it would be best to just measure the Eddy Covariance flux, $\overline{w'\phi'}$. This flux can then possibly be corrected using the expected spatially averaged imbalance, $\langle I \rangle$, from equation (2.51). The averaged imbalance is used because it is not known which exact imbalance occurred at a specific location. The constants in equations (2.52) and (2.53), which are used in this imbalance predicting function, should be determined using a LES model representing the circumstances present at the observation site. Knowing that $F_{\mathrm{EC}} = \overline{w'\phi'}$, equation (2.31) can be rewritten such that

$$\langle \overline{F} \rangle = \frac{F_{\mathrm{EC}}}{1 + I} \tag{5.1}$$

From the measured EC flux, F_{EC}, the spatially averaged total flux, $\langle \overline{F} \rangle$, should be determined. Since the local imbalance, I, is not known, an estimation for the total flux is made

using the spatially averaged imbalance, $\langle I \rangle$, calculated from equation (2.51). Using this, a corrected flux, $F_{\text{corrected}}$, is calculated according to

$$F_{\text{corrected}} = \frac{F_{\text{EC}}}{1 + \langle I \rangle} \tag{5.2}$$

The theoretical derived equation (A.28) in Appendix A, the published figures derived from simulated data (Huang et al., 2008; Schalkwijk, 2008) and equation (2.51), which was derived by Huang et al. (2008), all indicate that $-1 < \langle I \rangle < 0$. Because of this $F_{\text{corrected}}$ will always be of the same sign but of greater magnitude than F_{EC}. This correction method should be tested to verify whether it works adequately.

Another recommendation concerns measuring the total emission at a location if the advective part of the flux could be measured as well. In addition to the vertical flux measurements, one would have to measure the horizontal fluxes at additional separate locations. These measurements could be used to determine the horizontal gradient of those horizontal fluxes at the main location. Using those values, the vertical flux can be corrected. The big problem would be to get a representative horizontal flux for the entire measurement height at every additional location.

In order to directly measure the total emission over a large area, it would be best to use the same principle as LES use. One would have to use many measurement towers that measure the total vertical flux at their location and are spread over a large area. However, this is practically impossible. The area would have to be large enough to neglect the difference in horizontal fluxes at the boundaries. A big problem with this measurement setup is that nobody can afford to buy it.

More research could be performed on the time scales needed for representative measurements of the turbulent kinematic flux at higher measurement heights (of the order of 60 m and higher). For example, using data obtained for varying parameters, like stability, wind velocities and convective velocity. The effects of these parameters on the time scales could then be researched. Since the integral time scale does not really work, Ogive time scales should be used for this research.

Acknowledgements

First of all, I would like to thank the readers of this thesis. After all, if no one would read it or use the results , a years work would be for nothing. Thank you for reading!

After the readers I immediately want to thank my supervisors. Without them the result would not be the same. Fred Bosveld was always very helpful, providing me with all the data and information I needed. The visits to the KNMI were always nice and educative. Stephan de Roode taught me a lot about the boundary layer. His enthusiasm is inspiring and it is a pleasure to hear him talk. Since he was most present in Delft, I could always show hem results or ask for advice. Because of this he performed a large part of the supervision. Petra Kroon helped me a lot, too. Her sharp eye, sincerity and her willingness to make the time to review the thesis contributed much to the quality of this report. Her experience in field experiments was important for the framework of the research. Also my supervising professor Harm Jonker contributed much. Under his supervision some initial research was done on the imbalance problem and he introduced me to the project. I found his confidence very important, especially when I temporarily lost some of my own. All four were very friendly which contributed to a nice work environment. Thank you all very much!

Another person who I owe my gratitude is Henk Klein Baltink of the KNMI. He provided me with the necessary data on the boundary layer heights. I also would like to thank all people at the MSP department in the Physics building. Erwin de Beus was always willing and able to help if something was wrong with our hardware. He, the PhD Students, the various Bachelor students and the other Master students contributed much to the fact that I really enjoyed working at the project. Thank you Adriaan Schuitmaker, Daniel Abrahams, Ernst Oldenhof, Johan van der Dussen, Melchior van Wessem, Robert van Driel, Steef Böing, Steven de Boer and Susan Pesman. I really liked your company.

The project described in this thesis is the final part of my studies Applied Physics at the Delft University of Technology. Now I would like to thank all the people who supported me all these years. First of all I mention my parents and my three sisters. Thank you all for the support you have given me the last six years and for the patience to wait for the end. My girlfriend, Astrid, was also very important. Thank you for your support when things were going tough. And finally, I would like to thank all my friends. Thank you all for the moments of relaxation.

Bibliography

M.J. Barrett and D.K. Hollingsworth. On the calculation of length scales for turbulent heat transfer correlation. *Journal of Heat Transfer*, 123:878 – 883, 2001.

F. Bosveld, 2008 - 2009. URL `http://www.knmi.nl/~bosveld/`.

F. Bosveld. Personal communication. 2008.

J.A. Businger. Evaluation of the accuracy with which dry deposition can be measured with current micrometeorological techniques. *Journal of climate and applied meteorology*, 25:1100–1124, 1986.

T.R. Camp and H.-W. Shin. Turbulence intensity and length scale measurements in multi-stage compressors. *Journal of Turbomachinery*, 117:38–46, 1995.

J.W.M. Cuijpers and P.G. Duynkerke. Large eddy simulation of trade wind cumulus clouds. *Journal of the Atmospheric Sciences*, 50:3894 – 3907, 1993.

R.L. Desjardins, J.I. Macpherson, P.H. Schuepp, and F. Karanja. An evaluation of aircraft flux measurements of CO_2, water vapor and sensible heat. *Boundary-Layer Meteorology*, 47:55 – 69, 1989.

J.J. Finnigan. A re-evaluation of long-term flux measurement techniques part II: Coordinate systems. *Boundary-Layer Meteorology*, 113:1–41, 2004.

J.R. Garratt. *The atmospheric boundary layer*. Cambridge University Press, 1992.

T. Heus. *On the edge of a cloud*. PhD thesis, Delft University of Technology, 2008.

J. Huang, X. Lee, and E.G. Patton. A modelling study of flux imbalance and the inuence of entrainment in the convective boundary layer. *Boundary-Layer Meteorology*, 127:273–292, 2008.

A. Inagaki, M. O. Letzel, S. Raasch, and M. Kanda. Abstract of: The impact of the surface heterogeneity on the energy imbalance problem using LES. *Journal of the Meteorological Society of Japan*, 84:187–198, 2006.

H.J.J. Jonker, P.G. Duynkerke, and J.W. Cuijpers. Mesoscale fluctuations in scalars generated by boundary layer convection. *Journal of the Atmospheric Sciences*, 56:801–808, 1999.

J.C. Kaimal, J.C. Wyngaard, Y. Izumi, and O.R. Coté. Spectral characteristics of surface-layer turbulence. *The Quarterly Journal of the Royal Meteorological Society*, 98:563–589, 1972.

J.J. Kaimal, J.C. Finnigan. *Atmospheric Boundary Layer Flows: Their Structure and Measurement*. Oxford university press, 1993.

M. Kanda, A. Inagaki, M.O. Letzel, S. Raasch, and T. Watanabe. LES study of the energy imbalance problem with eddy covariance fluxes. *Boundary-Layer Meteorology*, 110:381–404, 2004.

P.S. Kroon, A. Hensen, H.J.J. Jonker, M.S. Zahniser, W.H. van 't Veen, and A.T. Vermeulen. Suitability of quantum cascade laser spectroscopy for CH_4 and N_2O eddy covariance flux measurements. *Biogeosciences*, 4:715–728, 2007.

X. Lee. On micrometeorological observations of surface-air exchange over tall vegetation. *Agricultural and Forest Meteorology*, 91:39–49, 1998.

X. Lee, J.J. Finnigan, and K.T. Paw U. *Handbook of Micrometeorology: A guide for Surface Flux Measurement and Analysis Series*, volume 29, chapter 3: Coordinate Systems and Flux Bias Error, pages 33–66. Atmospheric and Oceanic Sciences Library, 2004.

D.H. Lenschow and L. Kristensen. Uncorrelated noise in turbulence measurements. *Journal of Atmospheric and Oceanic Technology*, 2:68–81, 1985.

D.H. Lenschow, J. Mann, and L. Kristensen. How long is long enough when measuring fluxes and other turbulence statistics. *Journal of Atmospheric and Oceanic Technology*, 11: 661–673, 1994.

C. Liebethal and T. Foken. On the significance of the webb correction to fluxes. *Boundary-Layer Meteorology*, 109:99–106, 2003.

D.K. Lilly. The representation of small-scale turbulence in numerical simulation experiments. In H. Goldstine, editor, *IBM Scientific Computing Symp. on Environmental Sciences*, pages 195–210, 1967.

L. Mahrt. Flux sampling errors for aircraft and towers. *Journal of Atmospheric and Oceanic Technology*, 15:416–429, 1998.

F.T.M. Nieuwstadt. *Turbulentie*. Epsilon Uitgaven, 1992.

F.T.M. Nieuwstadt and R.A. Brost. The decay of convective turbulence. *Journal of the Atmospheric Sciences*, 43:532 – 545, 1986.

S.P. Oncley, C.A. Friehe, J.C. Larue, J.A. Businger, E.C. Itsweire, and S.S. Chang. Surface-layer fluxes, profiles, and turbulence measurements over uniform terrain under near-neutral conditions. *Journal of the Atmospheric Sciences*, 53:1029 – 1044, 1996.

H.A. Panofsky and J.A. Dutton. *Atmospheric Turbulence*. Wiley, 1984.

K.T. Paw U, D.D. Baldocchi, T.P. Meyers, and K.B. Wilson. Correction of eddy-covariance measurements incorporating both advective effects and density fluxes. *Boundary-Layer Meteorology*, 97:487–511, 2000.

J. Schalkwijk. LES study on the flux imbalance in the convective boundary layer. *Bachelor's thesis, Delft Institute of Technology*, 2008.

J. Slager. Measuring the viscous dissipation of turbulent kinetic energy with a hotwire and sonic anemometer. Master's thesis, Institute for Marine and Atmospheric Research, Utrecht University, 2001.

G. Steinfeld, M.O. Letzel, S. Raasch, M. Kanda, and A. Inagaki. Spatial representativeness of single tower measurements and the imbalance problem with eddy-covariance fluxes: results of a large-eddy simulation study. *Boundary-Layer Meteorology*, 123:77–98, 2007.

R.B. Stull. *An Introduction to Boundary Layer Meteorology*. Kluwer Academic Publishers, 1988.

T.E. Twine, W.P. Kustas, J.M. Norman, D.R. Cook, P.R. Houser, T.P. Meyers, J.H. Prueger, P.J. Starks, and M.L. Wesely. Correcting eddy-covariance flux underestimates over a grassland. *Agricultural and Forest Meteorology*, 103:279–300, 2000.

M. van Zanten. *Entrainment processes in stratocumulus*. PhD thesis, Utrecht University, 2000.

D. Vickers and L. Mahrt. The cospectral gap and turbulent flux calculations. *Journal of the Atmospheric Sciences*, 20:660–672, 2003.

E.K. Webb, G.I. Pearman, and R. Leuning. Correction of flux measurements for density effects due to heat and water vapour transfer. *The Quarterly Journal of the Royal Meteorological Society*, 106:85–100, 1980.

J.M. Wilczak, S.P. Oncley, and S.A. Stage. Sonic anemometer tilt correction algorithms. *Boundary-Layer Meteorology*, 99:127–150, 2001.

J.C. Wyngaard. *Workshop on Micrometeorology*, chapter 3: On Surface-Layer Turbulence, pages 101–149. American Meteorological Society, 1973.

J.C. Wyngaard and R.A. Brost. Top-down and bottom-up diffusion of a scalar in the convective boundary layer. *Journal of the Atmospheric Sciences*, 41:102–112, 1984.

BIBLIOGRAPHY

Appendix A

Analytical derivation of the imbalance

A.1 Used equations

In this appendix a few sine and cosine functions are used. These are

$$\sin(a + b) = \sin(a)\cos(b) + \cos(a)\sin(b) \tag{A.1}$$
$$\cos(a + b) = \cos(a)\cos(b) - \sin(a)\sin(b) \tag{A.2}$$
$$\cos(-a) = \cos(a) \tag{A.3}$$
$$\sin(-a) = -\sin(a) \tag{A.4}$$

From these equations, it is easy to derive

$$\sin(2a) = 2\sin(a)\cos(a) \tag{A.5}$$
$$\sin^2(a) = \frac{1}{2} - \frac{1}{2}\cos(2a) \tag{A.6}$$
$$\cos^2(a) = \frac{1}{2} + \frac{1}{2}\cos(2a) \tag{A.7}$$

It is assumed that the vertical wind speed and the magnitude of a scalar are periodic and given by

$$w = w_0 \sin\left(2\pi\frac{x - \overline{u}t}{L} + \theta_1\right) \tag{A.8}$$
$$\phi = \phi_0 \sin\left(2\pi\frac{x - \overline{u}t}{L} + \theta_1 + \theta_2\right) + \phi_1 \tag{A.9}$$

in which w and ϕ are the vertical wind speed and scalar respectively. w_0 and ϕ_0 are their respective amplitudes. The coordinate system is chosen such that the horizontal wind points to the positive x-direction. The average value of the horizontal wind speed is $\overline{u}$. The vertical wind velocity and magnitude of the scalar are periodic with distance L, which is of the order of a kilometre according to Figure 2.3. θ_1 and θ_2 are phase shifts.

A.2 Derivation of the spatial averaged imbalance

Using equation, (A.1), equation (A.9) can be written as

$$\phi = \phi_0 \sin\left(2\pi\frac{x - \overline{u}t}{L} + \theta_1\right)\cos(\theta_2) + \phi_0 \cos\left(2\pi\frac{x - \overline{u}t}{L} + \theta_1\right)\sin(\theta_2) + \phi_1 \tag{A.10}$$

so

$$w\phi = w_o\phi_1 \sin\left(2\pi\frac{x - \overline{u}t}{L} + \theta_1\right) + w_0\phi_0\left[\sin^2\left(2\pi\frac{x - \overline{u}t}{L} + \theta_1\right)\cos(\theta_2)\right.$$
$$\left. + \cos\left(2\pi\frac{x - \overline{u}t}{L} + \theta_1\right)\sin\left(2\pi\frac{x - \overline{u}t}{L} + \theta_1\right)\sin(\theta_2)\right] \tag{A.11}$$
$$= w_0\phi_0\left[\sin^2\left(2\pi\frac{x - \overline{u}t}{L} + \theta_1\right)\cos(\theta_2) + \frac{1}{2}\sin\left(4\pi\frac{x - \overline{u}t}{L} + 2\theta_1\right)\sin(\theta_2)\right]$$
$$+ w_o\phi_1 \sin\left(2\pi\frac{x - \overline{u}t}{L} + \theta_1\right) \tag{A.12}$$

Assuming that the prescribed profiles are valid for a region far larger than L

$$\langle\chi\rangle = \frac{1}{L}\int_0^L \chi\mathrm{d}x \tag{A.13}$$

for every variable χ. The reason for this will be explained here. Assume that the length of the region is L_{tot} in which $L_{tot} = nL + l$ with n an integer. When the profiles are valid for a region far larger than L, $n \gg 1$ and therefore $\frac{l}{L_{tot}} \approx 0$ and $L_{tot} \approx nL$. This results in

$$\langle\chi\rangle = \frac{1}{L_{tot}}\int_0^{L_{tot}}\chi\mathrm{d}x$$
$$= \frac{\sum_{k=0}^{n-1}\left(\int_{kL}^{(k+1)L}\chi\mathrm{d}x\right) + \int_{nL}^{L_{tot}}\chi\mathrm{d}x}{L_{tot}}$$
$$\approx \frac{\sum_{k=0}^{n-1}\left(\int_0^L\chi\mathrm{d}x\right)}{nL} + \frac{\int_0^l\chi\mathrm{d}x}{nL}$$
$$\approx \frac{1}{L}\int_0^L\chi\mathrm{d}x$$

Using equation (A.13)

$$\langle w\phi_1\rangle = \frac{1}{L}\int_0^L w_0 \sin\left(2\pi\frac{x - \overline{u}t}{L} + \theta_1\right)\mathrm{d}x = 0 \tag{A.14}$$

so, according to equation (A.10)

$$\langle w\phi\rangle = \left\langle w\phi_0 \sin\left(2\pi\frac{x - \overline{u}t}{L} + \theta_1 + \theta_2\right)\right\rangle + \langle w\phi_1\rangle \tag{A.15}$$
$$= 0 + \frac{1}{L}\int_0^L\left\{w_0\phi_0 \sin\left(2\pi\frac{x - \overline{u}t}{L} + \theta_1\right)\left[\sin\left(2\pi\frac{x - \overline{u}t}{L} + \theta_1\right)\cos(\theta_2)\right.\right.$$
$$\left.\left. + \cos\left(2\pi\frac{x - \overline{u}t}{L} + \theta_1\right)\sin(\theta_2)\right]\right\}\mathrm{d}x \tag{A.16}$$

Using equations (A.5) and (A.6), equation (A.16) becomes

$$\langle w\phi \rangle = \frac{w_0 \phi_0}{L} \int_0^L \left\{ \left[\frac{1}{2} - \frac{1}{2} \cos\left(4\pi \frac{x - \overline{u}t}{L} + 2\theta_1 \right) \right] \cos(\theta_2) \right.$$
$$\left. + \frac{1}{2} \sin\left(4\pi \frac{x - \overline{u}t}{L} + 2\theta_1 \right) \sin(\theta_2) \right\} dx \qquad (A.17)$$

$$\langle w\phi \rangle = \frac{w_o \phi_0}{2} \cos(\theta_2) \qquad (A.18)$$

Equation (A.18) is independent of the time. Therefore automatically

$$\overline{\langle w\phi \rangle} = \frac{w_o \phi_0}{2} \cos(\theta_2) \qquad (A.19)$$

The measurement time, T, can be expressed as

$$T = n\frac{L}{\overline{u}} + \alpha \qquad \text{in which} \qquad n \in \mathbb{N} \qquad \text{and} \qquad 0 \leq \alpha < \frac{L}{\overline{u}} \qquad (A.20)$$

Using this, expressions for $\overline{w}$ and $\overline{\phi}$ can be determined. The time average of equation (A.8) is

$$\overline{w} = \frac{1}{T} \int_0^T w_0 \sin\left(2\pi \frac{x - \overline{u}t}{L} + \theta_1 \right) dt$$
$$= -\frac{w_0}{T} \int_0^T \sin\left(2\pi \frac{\overline{u}t}{L} - 2\pi \frac{x}{L} - \theta_1 \right) dt$$
$$= \frac{w_0}{T} \left[\frac{L}{2\pi \overline{u}} \cos\left(2\pi \frac{\overline{u}t}{L} - 2\pi \frac{x}{L} - \theta_1 \right) \right]_0^T$$
$$= \frac{w_0 L}{2\pi \overline{u} T} \left[\cos\left(2\pi \frac{\overline{u}\alpha}{L} + 2\pi m - 2\pi \frac{x}{L} - \theta_1 \right) - \cos\left(-2\pi \frac{x}{L} - \theta_1 \right) \right]$$

so the time averaged value of the vertical wind velocity is given by

$$\overline{w} = \frac{w_0 L}{2\pi \overline{u} T} \left[\cos\left(2\pi \frac{\overline{u}\alpha}{L} - 2\pi \frac{x}{L} - \theta_1 \right) - \cos\left(-2\pi \frac{x}{L} - \theta_1 \right) \right] \qquad (A.21)$$

ϕ shows the same behaviour as w except for an constant term, ϕ_1, and a different phase angle, $\theta_1 + \theta_2$ instead of just θ_1. In analogy with equation (A.21) it is thus clear that the time averaged value of the magnitude of the scalar is given by

$$\overline{\phi} = \frac{\phi_0 L}{2\pi \overline{u} T} \left[\cos\left(2\pi \frac{\overline{u}\alpha}{L} - 2\pi \frac{x}{L} - \theta_1 - \theta_2 \right) - \cos\left(-2\pi \frac{x}{L} - \theta_1 - \theta_2 \right) \right] + \phi_1 \qquad (A.22)$$

A.2 Derivation of the spatial averaged imbalance

Now the spatial average of $\overline{w}\,\overline{\phi}$ is calculated.

$$\langle \overline{w}\,\overline{\phi} \rangle = \frac{w_0 \phi_0 L^2}{4\pi^2 \overline{u}^2 T^2}\left[\left\langle \cos\left(2\pi\frac{\overline{u}\alpha}{L} - 2\pi\frac{x}{L} - \theta_1\right)\cos\left(2\pi\frac{\overline{u}\alpha}{L} - 2\pi\frac{x}{L} - \theta_1 - \theta_2\right)\right\rangle \right.$$

$$- \left\langle \cos\left(2\pi\frac{\overline{u}\alpha}{L} - 2\pi\frac{x}{L} - \theta_1\right)\cos\left(-2\pi\frac{x}{L} - \theta_1 - \theta_2\right)\right\rangle$$

$$- \left\langle \cos\left(-2\pi\frac{x}{L} - \theta_1\right)\cos\left(2\pi\frac{\overline{u}\alpha}{L} - 2\pi\frac{x}{L} - \theta_1 - \theta_2\right)\right\rangle$$

$$\left. + \left\langle \cos\left(-2\pi\frac{x}{L} - \theta_1\right)\cos\left(-2\pi\frac{x}{L} - \theta_1 - \theta_2\right)\right\rangle \right]$$

$$+ \frac{w_0 \phi_1 L}{2\pi \overline{u} T}\left[\left\langle \cos\left(2\pi\frac{\overline{u}\alpha}{L} - 2\pi\frac{x}{L} - \theta_1\right)\right\rangle \right.$$

$$\left. - \left\langle \cos\left(-2\pi\frac{x}{L} - \theta_1\right)\right\rangle \right] \tag{A.23}$$

This long equation can be calculated by evaluating all separate spatial averages. Using equations (A.2), (A.3), (A.4), (A.5), (A.6), (A.7) and (A.13), these averages are given by

$$\left\langle \cos\left(2\pi\frac{\overline{u}\alpha}{L} - 2\pi\frac{x}{L} - \theta_1\right)\cos\left(2\pi\frac{\overline{u}\alpha}{L} - 2\pi\frac{x}{L} - \theta_1 - \theta_2\right)\right\rangle$$

$$= \frac{1}{L}\int_0^L \cos\left(2\pi\frac{\overline{u}\alpha}{L} - 2\pi\frac{x}{L} - \theta_1\right)\cos\left(2\pi\frac{\overline{u}\alpha}{L} - 2\pi\frac{x}{L} - \theta_1 - \theta_2\right)\mathrm{d}x$$

$$= \frac{1}{L}\int_0^L \cos\left(2\pi\frac{x}{L} + \tilde{\theta}\right)\cos\left(2\pi\frac{x}{L} + \tilde{\theta}\right)\cos\left(\theta_2\right)\mathrm{d}x$$

$$- \frac{1}{L}\int_0^L \cos\left(2\pi\frac{x}{L} + \tilde{\theta}\right)\sin\left(2\pi\frac{x}{L} + \tilde{\theta}\right)\sin\left(\theta_2\right)\mathrm{d}x$$

$$= \frac{1}{L}\int_0^L \left\{ \frac{1}{2}\cos\left(\theta_2\right) + \frac{1}{2}\cos\left(4\pi\frac{x}{L} + 2\tilde{\theta}\right)\cos\left(\theta_2\right)\mathrm{d}x \right.$$

$$\left. - \int_0^L \frac{1}{2}\sin\left(4\pi\frac{x}{L} + 2\tilde{\theta}\right)\sin\left(\theta_2\right)\right\}\mathrm{d}x$$

$$= \frac{1}{2}\cos(\theta_2)$$

in which $\tilde{\theta} = \theta_1 - 2\pi\frac{\overline{u}\alpha}{L}$.

$$\left\langle \cos\left(2\pi\frac{\overline{u}\alpha}{L} - 2\pi\frac{x}{L} - \theta_1\right)\cos\left(-2\pi\frac{x}{L} - \theta_1 - \theta_2\right)\right\rangle$$

$$= \frac{1}{L}\int_0^L \cos\left(2\pi\frac{\overline{u}\alpha}{L} - 2\pi\frac{x}{L} - \theta_1\right)\cos\left(-2\pi\frac{x}{L} - \theta_1 - \theta_2\right)\mathrm{d}x$$

$$= \frac{1}{L} \int_0^L \left\{ \left[\cos\left(2\pi\frac{\overline{u}\alpha}{L}\right) \cos\left(2\pi\frac{x}{L} + \theta_1\right) + \sin\left(2\pi\frac{\overline{u}\alpha}{L}\right) \sin\left(2\pi\frac{x}{L} + \theta_1\right) \right] \right.$$
$$\left. \left[\cos\left(\theta_2\right) \cos\left(2\pi\frac{x}{L} + \theta_1\right) - \sin\left(\theta_2\right) \sin\left(2\pi\frac{x}{L} + \theta_1\right) \right] \right\} \mathrm{d}x$$

$$= \frac{1}{L} \int_0^L \left\{ \cos\left(\theta_2\right) \cos\left(2\pi\frac{\overline{u}\alpha}{L}\right) \cos^2\left(2\pi\frac{x}{L} + \theta_1\right) \right.$$
$$+ \left[\cos\left(\theta_2\right) \sin\left(2\pi\frac{\overline{u}\alpha}{L}\right) - \sin\left(\theta_2\right) \cos\left(2\pi\frac{\overline{u}\alpha}{L}\right) \right]$$
$$\cos\left(2\pi\frac{x}{L} + \theta_1\right) \sin\left(2\pi\frac{x}{L} + \theta_1\right)$$
$$\left. - \sin\left(\theta_2\right) \sin\left(2\pi\frac{\overline{u}\alpha}{L}\right) \sin^2\left(2\pi\frac{x}{L} + \theta_1\right) \right\} \mathrm{d}x$$

$$= \frac{1}{L} \int_0^L \left\{ \frac{1}{2} \cos\left(\theta_2\right) \cos\left(2\pi\frac{\overline{u}\alpha}{L}\right) + \frac{1}{2} \cos\left(\theta_2\right) \cos\left(2\pi\frac{\overline{u}\alpha}{L}\right) \cos\left(4\pi\frac{x}{L} + 2\theta_1\right) \right.$$
$$+ \left[\cos\left(\theta_2\right) \sin\left(2\pi\frac{\overline{u}\alpha}{L}\right) - \sin\left(\theta_2\right) \cos\left(2\pi\frac{\overline{u}\alpha}{L}\right) \right] \frac{1}{2} \sin\left(4\pi\frac{x}{L} + 2\theta_1\right)$$
$$\left. - \frac{1}{2} \sin\left(\theta_2\right) \sin\left(2\pi\frac{\overline{u}\alpha}{L}\right) + \frac{1}{2} \sin\left(\theta_2\right) \sin\left(2\pi\frac{\overline{u}\alpha}{L}\right) \cos\left(4\pi\frac{x}{L} + 2\theta_1\right) \right\} \mathrm{d}x$$

$$= \frac{1}{2} \cos\left(\theta_2\right) \cos\left(2\pi\frac{\overline{u}\alpha}{L}\right) - \frac{1}{2} \sin\left(\theta_2\right) \sin\left(2\pi\frac{\overline{u}\alpha}{L}\right)$$

$$\left\langle \cos\left(-2\pi\frac{x}{L} - \theta_1\right) \cos\left(2\pi\frac{\overline{u}\alpha}{L} - 2\pi\frac{x}{L} - \theta_1 - \theta_2\right) \right\rangle$$

$$= \frac{1}{L} \int_0^L \cos\left(-2\pi\frac{x}{L} - \theta_1\right) \cos\left(2\pi\frac{\overline{u}\alpha}{L} - 2\pi\frac{x}{L} - \theta_1 - \theta_2\right) \mathrm{d}x$$

$$= \frac{1}{L} \int_0^L \left\{ \cos\left(2\pi\frac{x}{L} + \theta_1\right) \cos\left(2\pi\frac{x}{L} + \theta_1\right) \cos\left(\theta_2 - 2\pi\frac{\overline{u}\alpha}{L}\right) \mathrm{d}x \right.$$
$$\left. - \frac{1}{L} \int_0^L \cos\left(2\pi\frac{x}{L} + \theta_1\right) \sin\left(2\pi\frac{x}{L} + \theta_1\right) \sin\left(\theta_2 - 2\pi\frac{\overline{u}\alpha}{L}\right) \right\} \mathrm{d}x$$

$$= \frac{1}{L} \int_0^L \frac{1}{2} \cos\left(\theta_2 - 2\pi\frac{\overline{u}\alpha}{L}\right) + \frac{1}{2} \cos\left(4\pi\frac{x}{L} + 2\theta_1\right) \cos\left(\theta_2 - 2\pi\frac{\overline{u}\alpha}{L}\right) \mathrm{d}x$$
$$- \int_0^L \frac{1}{2} \sin\left(4\pi\frac{x}{L} + 2\theta_1\right) \sin\left(\theta_2 - 2\pi\frac{\overline{u}\alpha}{L}\right) \mathrm{d}x$$

$$= \frac{1}{2} \cos\left(\theta_2 - 2\pi\frac{\overline{u}\alpha}{L}\right)$$

$$= \frac{1}{2} \cos{(\theta_2)} \cos{\left(2\pi\frac{\overline{u}\alpha}{L}\right)} + \frac{1}{2} \sin{(\theta_2)} \sin{\left(2\pi\frac{\overline{u}\alpha}{L}\right)}$$

$$\left\langle \cos{\left(-2\pi\frac{x}{L} - \theta_1\right)} \cos{\left(-2\pi\frac{x}{L} - \theta_1 - \theta_2\right)} \right\rangle$$

$$= \frac{1}{L} \int_0^L \cos{\left(-2\pi\frac{x}{L} - \theta_1\right)} \cos{\left(-2\pi\frac{x}{L} - \theta_1 - \theta_2\right)} \, \mathrm{d}x$$

$$= \frac{1}{L} \int_0^L \cos{\left(2\pi\frac{x}{L} + \theta_1\right)} \cos{\left(2\pi\frac{x}{L} + \theta_1\right)} \cos{(\theta_2)} \, \mathrm{d}x$$

$$- \frac{1}{L} \int_0^L \cos{\left(2\pi\frac{x}{L} + \theta_1\right)} \sin{\left(2\pi\frac{x}{L} + \theta_1\right)} \sin{(\theta_2)} \, \mathrm{d}x$$

$$= \frac{1}{L} \int_0^L \left\{ \frac{1}{2} \cos{(\theta_2)} + \frac{1}{2} \cos{\left(4\pi\frac{x}{L} + 2\theta_1\right)} \cos{(\theta_2)} \, \mathrm{d}x \right.$$

$$\left. - \int_0^L \frac{1}{2} \sin{\left(4\pi\frac{x}{L} + 2\theta_1\right)} \sin{(\theta_2)} \right\} \mathrm{d}x$$

$$= \frac{1}{2} \cos(\theta_2)$$

$$\left\langle \cos{\left(2\pi\frac{\overline{u}\alpha}{L} - 2\pi\frac{x}{L} - \theta_1\right)} \right\rangle = \frac{1}{L} \int_0^L \cos{\left(2\pi\frac{\overline{u}\alpha}{L} - 2\pi\frac{x}{L} - \theta_1\right)} \, \mathrm{d}x$$

$$= \frac{1}{L} \int_0^L \cos{\left(2\pi\frac{x}{L} + \tilde{\theta}\right)} \, \mathrm{d}x$$

$$= 0$$

in which again $\tilde{\theta} = \theta_1 - 2\pi\frac{\overline{u}\alpha}{L}$

$$\left\langle \cos{\left(-2\pi\frac{x}{L} - \theta_1\right)} \right\rangle = \frac{1}{L} \int_0^L \cos{\left(-2\pi\frac{x}{L} - \theta_1\right)} \, \mathrm{d}x$$

$$= \frac{1}{L} \int_0^L \cos{\left(2\pi\frac{x}{L} + \theta_1\right)} \, \mathrm{d}x$$

$$= 0$$

If the results of the partial averages are used in equation (A.23), the total spatial average of the temporal averaged scalar amount and vertical wind velocity is given by

$$\langle \overline{w}\,\overline{\phi} \rangle = \frac{L^2 w_0 \phi_0}{4\pi^2 \overline{u}^2 T^2} \cos{(\theta_2)} \left[1 - \cos{\left(2\pi\frac{\overline{u}\alpha}{L}\right)} \right] \tag{A.24}$$

The spatial average of the imbalance is given by equation (2.33), which is, according to equation (2.15), equal to

$$\langle I \rangle = \frac{-\left\langle \overline{w}\,\overline{\phi} \right\rangle}{\left\langle \overline{w\phi} \right\rangle} \tag{A.25}$$

Combining equations (A.19), (A.24) and (A.25) results in

$$\langle I \rangle = -\frac{L^2}{2\pi^2 \overline{u}^2 T^2}\left[1 - \cos\left(2\pi \frac{\overline{u}\alpha}{L}\right)\right] \tag{A.26}$$

A.3   Implications of the theoretical spatial averaged imbalance

Since the cosine has a maximum of 1, equation (A.26) will always give a negative result, unless $\langle I \rangle = 0$. The equation is plotted in Maple as a function of T for $\overline{u} = 0.1$ m s^{-1} and $\overline{u} = 1$ m s^{-1}. In both cases, $L = 1000$ m. Figure A.1 shows the case in which $\overline{u} = 0.1$ m s^{-1}. In this figure it can be seen that for very low wind speeds, the spatial averaged imbalance is negative and has a large value. Figure A.2 shows the case in which $\overline{u} = 1$ m s^{-1}. In this figure the general behaviour of the spatial averaged imbalance function is clearly visible. It is always negative, but it oscillates and the amplitude of the oscillation decreases. For these values, measuring a quarter of an hour would be enough to get a spatial averaged imbalance that is less than 0.05. The higher the horizontal wind velocity, the less measurement time is needed to get a small imbalance.

When the dimensionless variable $T^\dagger$ is defined as

$$T^\dagger = \frac{\overline{u}T}{L} \tag{A.27}$$

the behaviour of the theoretical $\langle I \rangle$ according to equation (A.26) can be expressed as a function of $T^\dagger$.

$$\langle I \rangle = \frac{\cos\left(2\pi T^\dagger\right) - 1}{2\pi^2 T^{\dagger 2}} \tag{A.28}$$

Equation (A.28) is plotted in Figure A.3. In contradiction to Figures A.1 and A.2, no assumptions have been made about the values of variables in order to plot this graph. In Table A.1 values of $T^\dagger$ are given for several values of $\langle I \rangle$. Please notice that for $T^\dagger > 1$, $\langle I \rangle$ is always higher than -0.0472. Therefore, as long as $T^\dagger \geq 0.813$, $\langle I \rangle > -0.0472$.

A few things are remarkable about equation (A.26).

The derived spatial averaged imbalance in this appendix is theoretical and not the result of instrumentation. Therefore it can not be prevented by "good measurements" when Eddy-Correlation fluxes are calculated. Corrections are possible, but in order to perform them, the average horizontal wind speed, the length with which the profiles are periodic and the time scale with which the profiles are periodic have to be known. Another problem with this is that in practice the profiles of both w as ϕ will consist of the summation of sines or cosines with different periods. Therefore the product of both quantities will also be a summation of sines or cosines with different periods. Every period will have its own contribution. Therefore the separate contributions from sines with different periods to the total eddy-covariance flux would have to be determined and then corrected.
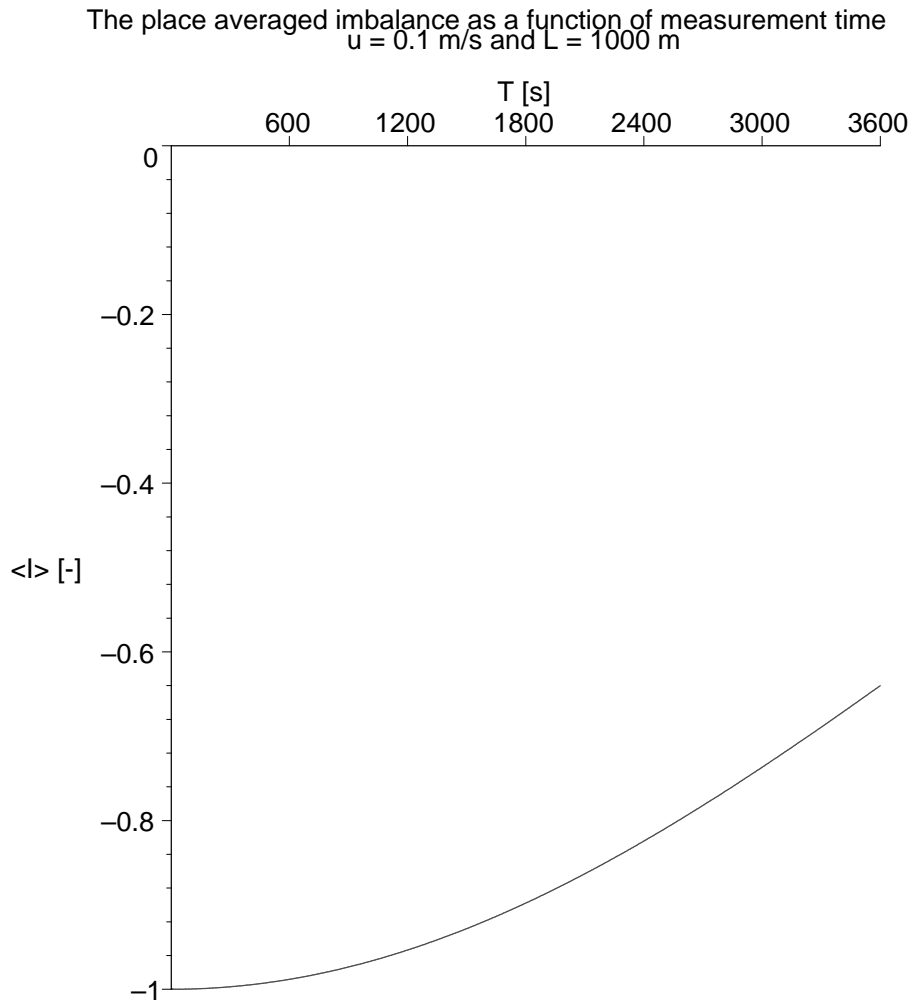
Figure A.1: Plot of the spatial averaged imbalance, $\langle I \rangle$, according to equation (A.26) for the case in which $L = 1000$ m and $\overline{u} = 0.1$ m s^{-1}. In this case measuring an hour still gives $\langle I \rangle < -0.6$.

Table A.1: The values of $T^\dagger$ needed to get a specific $\langle I \rangle$ according to equation (A.28) and as shown in Figure A.3. The equation is solved for different values of $\langle I \rangle$ with the help of Maple. Although the spatial averaged imbalance has an oscillating term, $\langle I \rangle > -0.0472$ when $T^\dagger \geq 0.813$

$\langle I \rangle$	$T^\dagger$
-1.00	0.000
-0.90	0.178
-0.80	0.258
-0.70	0.323
-0.60	0.384
-0.50	0.443
-0.40	0.503
-0.30	0.568
-0.20	0.642
-0.10	0.738
-0.05	0.808
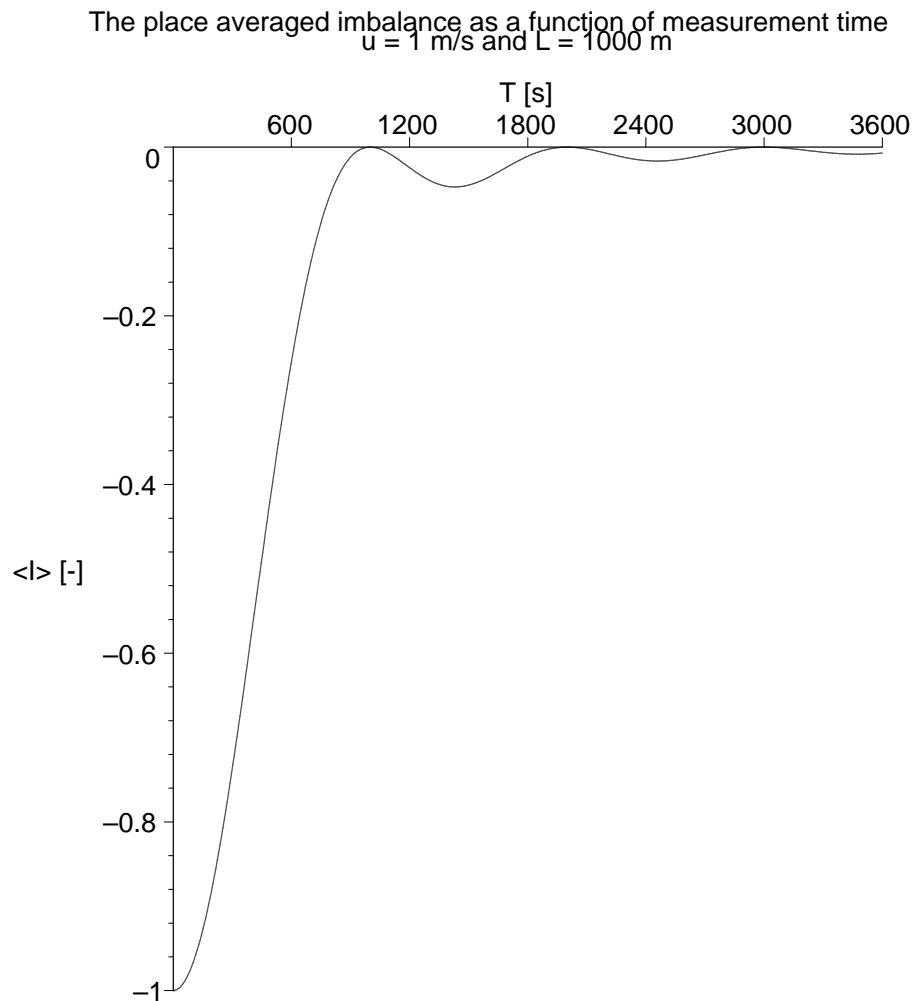
Figure A.2: Plot of the spatial averaged imbalance, $\langle I \rangle$, according to equation (A.26) for the case in which $L = 1000$ m and $\overline{u} = 1$ m s^{-1}. In this case measuring a quarter of an hour already gives $\langle I \rangle > -0.1$.

Place averaged imbalance versus the dimensionless measurement time
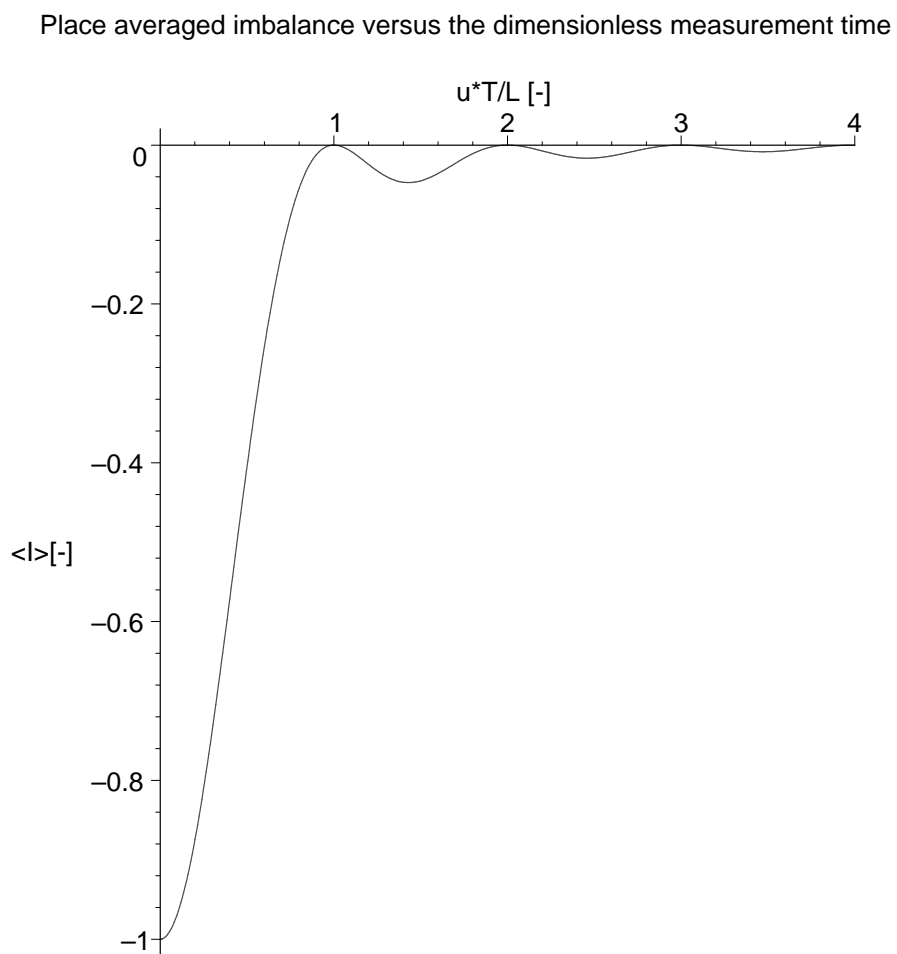
Figure A.3: Plot of the spatial averaged imbalance, $\langle I \rangle$, versus the dimensionless time, $T^{\dagger}$, according to equation (A.28).

Furthermore, because of these sines with different time scales, it is theoretically impossible to have a non-zero α for all contributions. Since no contributions to the spatial averaged imbalance are positive, the total spatial averaged imbalance will always exist and be negative. However, for high horizontal wind velocities, small length scales or long measurement times, the theoretical imbalance will rapidly decrease.

The theoretical imbalance is independent of the actual magnitudes of the vertical wind velocity and the scalar. The only parameters of importance are the measurement time, T, the average horizontal wind speed $\overline{u}$, the length with which the profiles are periodic, L and the time that is measured in an uncompleted cycle, α. Since α can be deducted from the other parameters, the imbalance becomes dependent on only one dimensionless variable, $T^{\dagger}$.

However, the derived negative imbalance is not necessarily real. In the derivation the assumption is made that w and ϕ both are periodic with the same period. However each quantity can described by more than one sinusoid.

$$w = \sum_k w_k \sin\left(2\pi \frac{x - \overline{u}t}{L_k} + \theta_{1,k}\right) \tag{A.29}$$

$$\phi = \phi_0 + \sum_k \phi_k \sin\left(2\pi \frac{x - \overline{u}t}{L_k} + \theta_{1,k} + \theta_{2,k}\right) \tag{A.30}$$

The $\theta_{1,k}$ does not matter for spatial averaged values, since it only determines the phase at which the integration starts. If the integral is taken over an integer amount of periods, this phase angle is irrelevant. With equation (A.25) and neglecting $\theta_{1,k}$ this results in

$$\langle I \rangle = \frac{-\left\langle \overline{\sum_k w_k \sin\left(2\pi \frac{x - \overline{u}t}{L_k}\right) \cdot \sum_k \phi_k \sin\left(2\pi \frac{x - \overline{u}t}{L_k} + \theta_{2,k}\right)} \right\rangle}{\left\langle \left[\sum_k w_k \sin\left(2\pi \frac{x - \overline{u}t}{L_k}\right)\right] \cdot \left[\sum_k \phi_k \sin\left(2\pi \frac{x - \overline{u}t}{L_k} + \theta_{2,k}\right)\right] \right\rangle} \tag{A.31}$$

The contribution to $\langle I \rangle$ from a w-term times a ϕ-term with another periodicity can not be predicted by equation (A.28) and could even be positive. However, figure 2.3 indicates that this problem most likely does not influence the imbalance very much, since the contrast between rising air and descending air would be less sharp if a large spread in periodicities would be present.

A.4   The theoretical imbalance

Equation (2.31) can be used for equations (A.8) and (A.9). However, the resulting solution for I is very long. Even when θ_1 and θ_2 are assumed to be 0, it would take many pages to only show the result. Therefore the found equation is not shown.

The solution is calculated by Maple and its probability density function is plotted for different values of the average horizontal wind speed, $\overline{u}$, and the phase difference, θ_2. This probability density function (pdf) is calculated by determining the function of the imbalance and by evaluating this at many positions. Plotting the imbalance for several different combinations of variable values showed that θ_1 has no influence on the probability density

function. L is assumed to be 1000 m and θ_1 is assumed to be 0. The graphs show that the higher the value of $\overline{u}$, the lower $\langle I \rangle$ (which is consistent with equation (A.26)) and also the smaller the range in which I lies. The phase angle θ_2 also has influence on the range in which I lies. This effect is periodic with π. When $\theta_2 = \frac{\pi}{2}$ or $\theta_2 = \frac{3\pi}{2}$, the minimum and maximum values of I will be $-\infty$ and ∞ respectively. This means that the measured flux can be any value at a certain point, even when there is no spatial averaged flux present. When $\theta_2 = 0$ or $\theta_2 = \pi$, the spread in I will be at its minimum. However, like shown in paragraph A.2 and in contradiction to $\overline{u}$, θ_2 does not influence the spatial averaged imbalance, $\langle I \rangle$.

The typical shape of the probability density function of I can be seen in Figure A.4. According to Figure 3 of Huang et al. (2008) and Figures 4.8 and 4.9 of Schalkwijk (2008), simulations indicate that the true probability density function is highest for I in the neighbourhood of $\langle I \rangle$ and decreases for values further away from $\langle I \rangle$. This difference is probably due to the fact that in this case only the imbalance is shown that is caused by a w-term and a ϕ-term of the same period. The product of a w-term and a ϕ-term with a different periodicity does not necessarily go to 0 when averaging, because the averages are not taken over a complete period. This could change the appearance of the pdf.
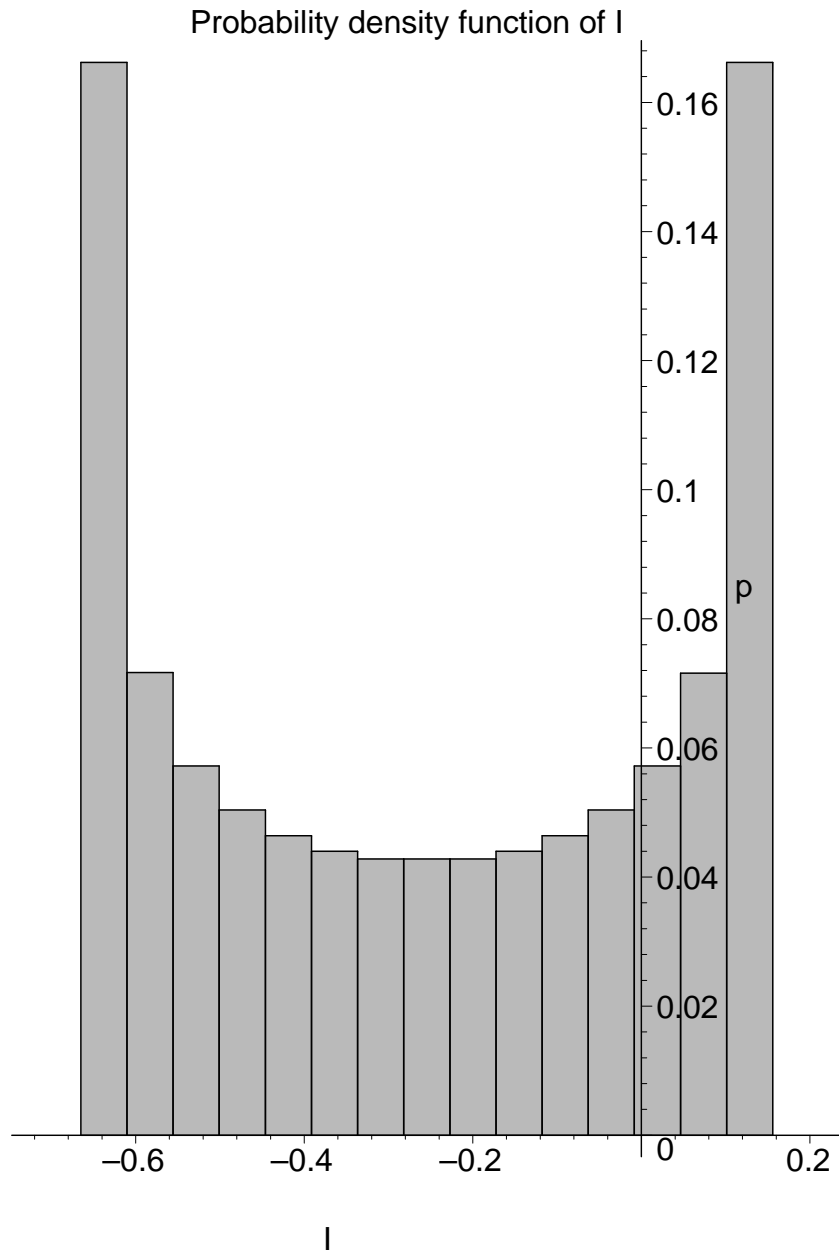
Figure A.4: Plot of the probability density function of the imbalance as given by Maple. This pdf is calculated by evaluating the imbalance function as given by equation (2.31) at 1001 equidistant positions for $x \in [0, L]$. Both θ_1 and θ_2 are chosen to be equal to 0. $u = 1 \text{ m s}^{-1}$, $L = 1000$ m and $T = 600$ s.

Appendix B

Dependence of the variance of w on the rotation angle

According to equation (3.6)

$$w_r = \cos(\beta(\theta)) w_m - \sin(\beta(\theta)) u_m \tag{B.1}$$

in which w_r is the vertical wind velocity after rotation, w_m is the measured vertical wind velocity and u_m is the measured horizontal wind velocity. Since the rotation angle, β, is not dependent on time when using the wind tilt correction method, the time average of equation (B.1) is given by

$$\overline{w}_r = \cos(\beta(\theta)) \overline{w}_m - \sin(\beta(\theta)) \overline{u}_m \tag{B.2}$$

And according to equation (2.3)

$$w_r = \overline{w}_r + w_r' \tag{B.3}$$
$$w_m = \overline{w}_m + w_m' \tag{B.4}$$
$$u_m = \overline{u}_m + u_m' \tag{B.5}$$

After substracting equation (B.2) from equation (B.1) and using the equations (B.3), (B.4) and (B.5) it is found that

$$w_r' = \cos(\beta(\theta)) w_m' - \sin(\beta(\theta)) u_m' \tag{B.6}$$

The variance of w, σ_w^2, is found by squaring equation (B.6).

$$w_r'^2 = \cos(\beta(\theta))^2 w_m'^2 + \sin(\beta(\theta))^2 u_m'^2 - 2\cos(\beta(\theta))\sin(\beta(\theta)) u_m' w_m' \tag{B.7}$$

which can be rewritten into

$$w_r'^2 = w_m'^2 + \left[u_m'^2 - w_m'^2 \right] \sin(\beta(\theta))^2 - u_m' w_m' \sin(2\beta(\theta)) \tag{B.8}$$

and thus

$$\overline{w_r'^2} = \overline{w_m'^2} + \left[\overline{u_m'^2} - \overline{w_m'^2} \right] \sin(\beta(\theta))^2 - \overline{u_m' w_m'} \sin(2\beta(\theta)) \tag{B.9}$$

which can be normalized by dividing by $\overline{{w'_{\mathrm{m}}}^{2}}$.

$$\frac{\overline{{w'_{\mathrm{r}}}^{2}}}{\overline{{w'_{\mathrm{m}}}^{2}}} = 1 + \frac{\overline{{u'_{\mathrm{m}}}^{2}} - \overline{{w'_{\mathrm{m}}}^{2}}}{\overline{{w'_{\mathrm{m}}}^{2}}} \sin\left(\beta\left(\theta\right)\right)^{2} - \frac{\overline{u'_{\mathrm{m}} w'_{\mathrm{m}}}}{\overline{{w'_{\mathrm{m}}}^{2}}} \sin\left(2\beta\left(\theta\right)\right) \tag{B.10}$$

Now assume that $\beta\left(\theta\right) = \beta$. For small angles β, the previous equation can be simplified to

$$\frac{\overline{{w'_{\mathrm{r}}}^{2}}}{\overline{{w'_{\mathrm{m}}}^{2}}} = 1 + 2\frac{-\overline{u'_{\mathrm{m}} w'_{\mathrm{m}}}}{\overline{{w'_{\mathrm{m}}}^{2}}}\beta + \frac{\overline{{u'_{\mathrm{m}}}^{2}} - \overline{{w'_{\mathrm{m}}}^{2}}}{\overline{{w'_{\mathrm{m}}}^{2}}}\beta^{2} \tag{B.11}$$

Since $\overline{{u'_{\mathrm{m}}}^{2}} > \overline{{w'_{\mathrm{m}}}^{2}}$ and $\overline{u'_{\mathrm{m}} w'_{\mathrm{m}}}$ is negative if assumed that the deviation with respect to the true coordinate system is small (Stull, 1988; Nieuwstadt, 1992), $\frac{\overline{{w'_{\mathrm{r}}}^{2}}}{\overline{{w'_{\mathrm{m}}}^{2}}}$ will increase for increasing β when $\beta > 0$. Also, as long as β is small enough, $\frac{\overline{{w'_{\mathrm{r}}}^{2}}}{\overline{{w'_{\mathrm{m}}}^{2}}}$ will decrease for decreasing β when $\beta < 0$. This can be seen in Figure B.1.

It is known that the rotation that should be applied, is of the order of tenths of degrees. From Figure B.1 it is clear that looking at the variance of the vertical wind velocity for different rotation angles is not helpful in determining the needed rotation, since the behaviour of the graphs remains the same in the whole domain.

Figure B.1: In these graphs, the variances of the vertical wind velocities are plotted in red as a function of the rotation angle, β, for different days and different heights. The left graphs are based on data obtained at 4th May 2008 and the right graphs are based on data obtained at 9th May 2008. The upper row of graphs is based on data measured at a height of 60 m, the middle row of graphs is based on data measured at a height of 100 m and the lower row of graphs is based on data measured at a height of 180 m. In every graph the variances for 8 succeeding periods, each with a length of 30 minutes, are plotted. The first period starts at 12:00 h local time. Also the average of the variances of the 8 periods is plotted as a black line. All plotted data is normalized by the value it would have without rotation.

Appendix C

Overview of used symbols

C.1 Latin symbols

Symbol	Description	Value	Unit
a	Accuracy	-	-
$a(\theta)$	Wind direction dependent coefficient	-	m s^{-1}
A_{av}	Averaging area	-	m^2
$b(\theta)$	Wind direction dependent coefficient	-	-
c	Concentration of a scalar	-	kg m^{-3}
c_b	Concentration of a bottom-up tracer	-	kg m^{-3}
c_{joined}	Superposition of c_b and c_t	-	kg m^{-3}
c_p	Specific heat of air	-	$\text{J kg}^{-1}\,\text{K}^{-1}$
c_{pd}	Specific heat of dry air	1004.67	$\text{J kg}^{-1}\,\text{K}^{-1}$
c_t	Concentration of a top-down tracer	-	kg m^{-3}
$C_{x,y}$	Cross spectrum of variables x and y	-	Various
d_i	Constants in an Imbalance equation	-	-
E	Emission	-	Various
E_x	Spectral energy density of variable x	-	Various
$E_{x,y}$	Cospectrum of variables x and y	-	Various
f	Relative flux change per radian rotation and	-	Rad^{-1}
	Frequency	-	s^{-1}
F	Flux	-	Various
F_b	Flux of the bottom-up tracer	-	$\text{kg m}^{-2}\,\text{s}^{-1}$
F_{EC}	Eddy-Covariance Flux	-	Various
F_t	Flux of the top-down tracer	-	$\text{kg m}^{-2}\,\text{s}^{-1}$
F_x	Fourier transform of x	-	Various
g	Gravitational acceleration	9.81	m s^{-2}

Continued from previous page

Symbol	Description	Value	Unit
I	Flux imbalance	-	-
I_S	Alternative definition of flux imbalance	-	Various
L	Length by which w and ϕ are periodic	-	m
	and		
	Monin-Obukhov length	-	m
L_{av}	Averaging length	-	m
n_f	Nyquist frequency	-	-
Og	Ogive	-	Various
p	Pressure	-	bar or N m^{-2}
p_0	Standard pressure	1	bar
q	Specific humidity	-	-
Q_0	Virtual heat flux near the ground	-	W m^{-2}
Q_H	Sensible heat flux	-	W m^{-2}
$\tilde{Q}_H$	Turbulent sensible heat flux	-	W m^{-2}
r	Linear correlation coefficient	-	-
	and		
	Mixing ratio of water in air	-	-
R	Gas constant for dry air	287.04	J K^{-1} kg^{-1}
s	Source or sink	-	Various
T	Period of measurement	-	s
	and		
	Temperature	-	K
$T^{\dagger}$	Dimensionless measurement time	-	-
t_a	Averaging time	-	h
T_{av}	Averaging time	-	s
$T_{Ogive,x,y}$	Ogive time scale of $\overline{x'y'}$	-	s
u	Horizontal wind velocity (x-direction)	-	m s^{-1}
	and		
	Uncertainty	-	Various
u_*	Friction velocity	-	m s^{-1}
U_g	Geostrophic wind	-	m s^{-1}
u_m	Measured u	-	m s^{-1}
$\overline{u}_N$	Time averaged u for different sectors of wind directions	-	m s^{-1}
u_r	u after rotation	-	m s^{-1}
v	Horizontal wind velocity (y-direction)	-	m s^{-1}
w	Vertical wind velocity	-	m s^{-1}
w_*	Convective velocity	-	m s^{-1}
w_0	Amplitude of a sinusoid function describing w	-	m s^{-1}
w_m	Measured w	-	m s^{-1}
$\overline{w}_N$	Time averaged w for different sectors of wind directions	-	m s^{-1}
w_r	w after rotation	-	m s^{-1}

Continued from previous page

Symbol	Description	Value	Unit
w_{WTC}	w after wind tilt correction	-	m s^{-1}
w_{ZR}	w after rotation per averaging block	-	m s^{-1}
x	Indiciation of horizontal position	-	m
y	Indiciation of horizontal position	-	m
z	Indiciation of height	-	m
z_i	Inversion height	-	m

C.2   Greek symbols

Symbol	Description	Value	Unit
α	Rotation angle to correct measured wind velocities	-	Rad
β	Rotation angle to correct measured wind velocities	-	Rad
β_N	Angle β for different sectors of wind directions	-	Rad
γ	Rotation angle to correct measured wind velocities	-	Rad
γ_d	Adiabatic temperature gradient	0.01	$K\,m^{-1}$
θ	Potential temperature	-	K
	and		
	Wind direction	-	$^\circ$
θ_0	Potential temperature at the surface	-	K
θ_i	Phase shift i	-	Rad
θ_v	Virtual potential temperature	-	K
κ	Von Kármán's constant	0.4	-
μ	Average	-	Various
ρ	Density of air	-	$kg\,m^{-3}$
σ	Standard deviation	-	Various
τ	Delay time	-	s
$\tau_{x,y}$	Integral time scale of $\overline{x'y'}$	-	s
ϕ	A scalar	-	Various
ϕ_0	Amplitude of a sinusoid function describing ϕ	-	Various
χ	A scalar	-	Various

Appendix D

Spirit level measurements

Spirit levels are placed at the measurement site described in Paragraph 3.1. In Figures D.1, D.2 and D.3 the measurements at the spirit levels are shown at respectively 3 m, 60 m and 180 m height for 2007 and 2008. The period of interest is June 2007, denoted by 200706, until May 2008, denoted by 200805. It can be seen that the spirit levels are quite constant. The deviations of the spirit level angles are of the order of a tenth °. As shown in Paragraph 3.2.5 this results in a relative uncertainty far smaller than 1 %. The outliers in the measurements are caused by displacements over a short time due to maintenance to the anemometers. After maintenance, the anemometers are set back to their original positions.
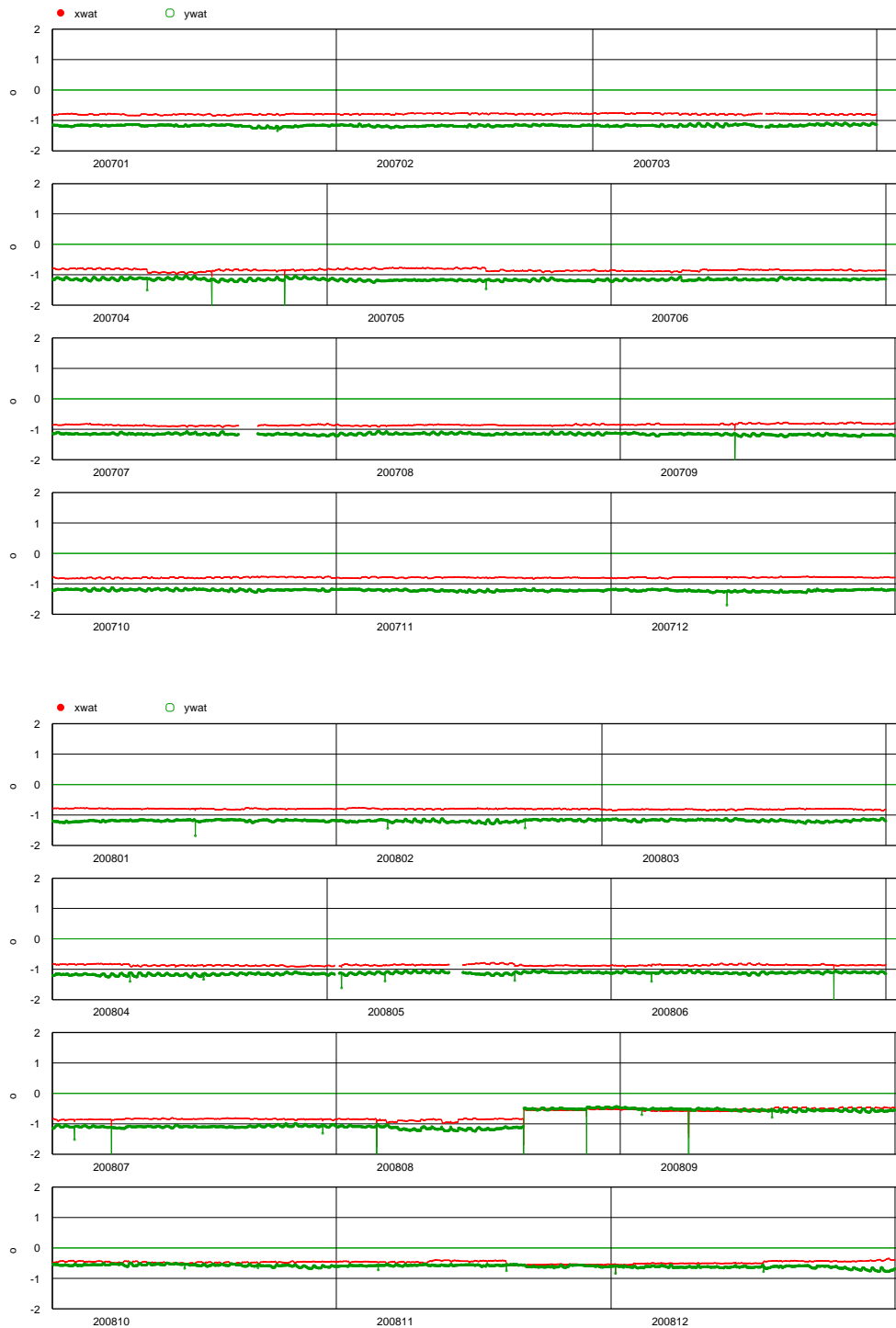
Figure D.1: Measurements at the spirit levels at 3 m height. The red line shows the angle with respect to the surface normal in one direction and the green line shows that angle in the direction perpendicular to the first direction. The period of interest is June 2007, denoted by 200706, until May 2008, denoted by 200805. The spirit levels are quite constant; the deviations are of the order of a tenth °. The peaks in the measurements are caused by maintenance. These graphs are provided by Bosveld (2008)
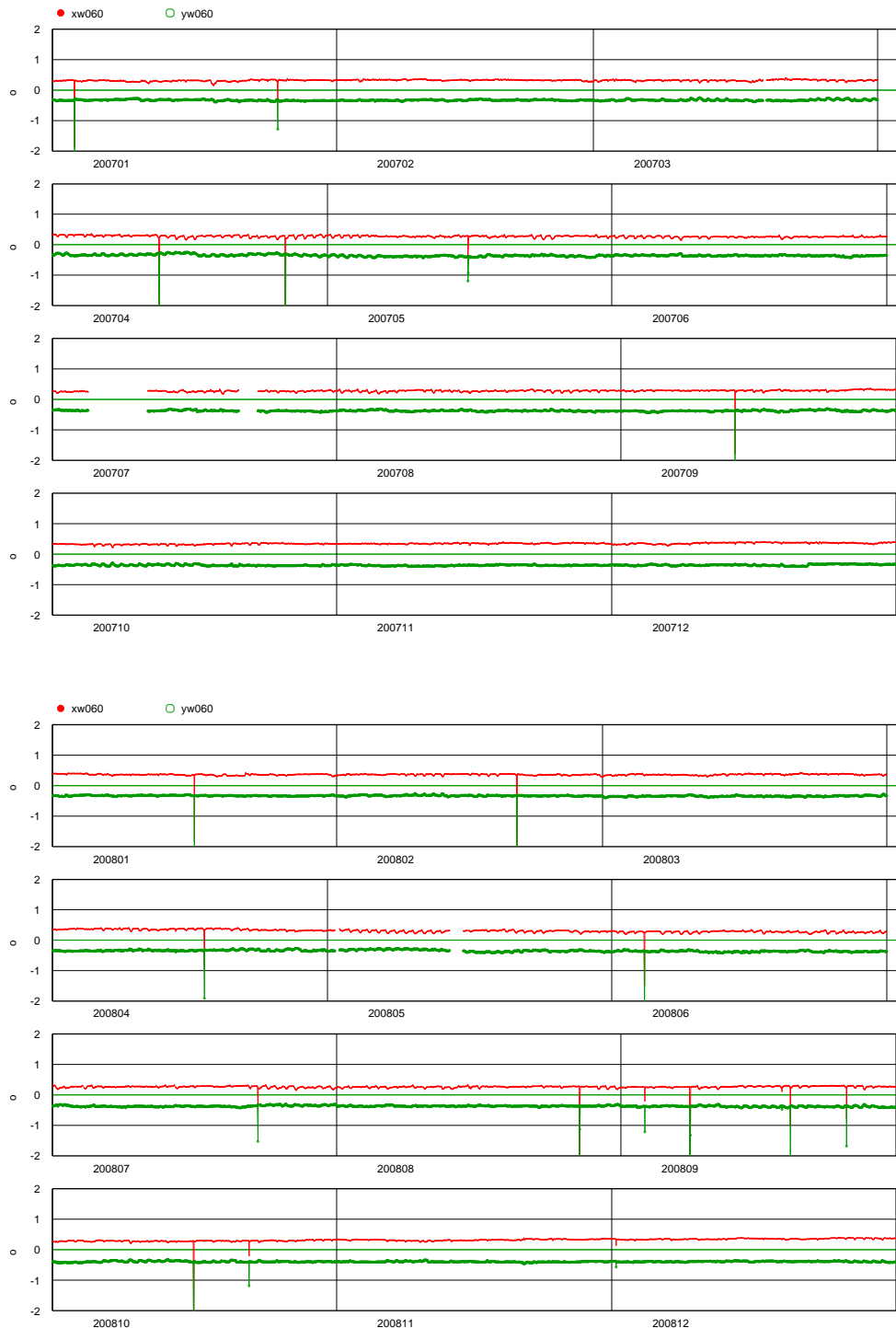
Figure D.2: Measurements at the spirit levels at 60 m height. The red line shows the angle with respect to the surface normal in one direction and the green line shows that angle in the direction perpendicular to the first direction. The period of interest is June 2007, denoted by 200706, until May 2008, denoted by 200805. The spirit levels are quite constant; the deviations are of the order of a tenth $^\circ$. The peaks in the measurements are caused by maintenance. These graphs are provided by Bosveld (2008)
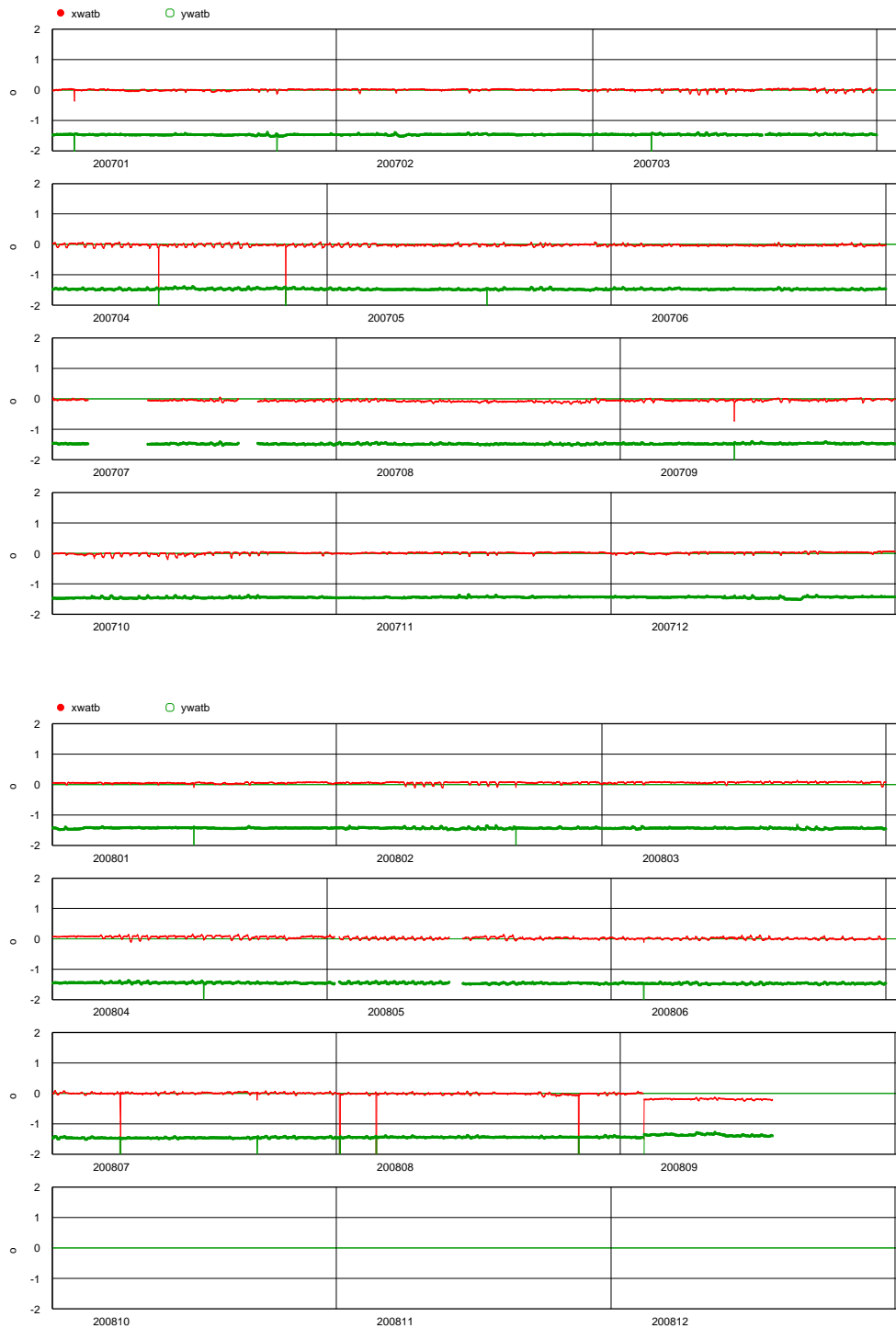
Figure D.3: Measurements at the spirit levels at 180 m height. The red line shows the angle with respect to the surface normal in one direction and the green line shows that angle in the direction perpendicular to the first direction. The period of interest is June 2007, denoted by 200706, until May 2008, denoted by 200805. The spirit levels are quite constant; the deviations are of the order of a tenth °. The peaks in the measurements are caused by maintenance. These graphs are provided by Bosveld (2008)

Appendix E

Wind tilt corrections

The wind tilt corrections for the sonic anemometers placed at 3 m, 60 m, 100 m and 180 m height are displayed in Tables E.1, E.2, E.3 and E.4, respectively. The data is plotted in Figure E.1. The wind tilt corrections are calculated over a year, from 1 June 2007 until 31 May 2008, by Bosveld (2008). Data points contain measurements averaged over 10 minutes. Data points are only selected if the horizontal wind velocity is higher than 3 m s^{-1}. After calculation of the wind tilt corrections, outliers are neglected and the final wind tilt corrections are calculated. This is done for 18 wind direction sectors, covering 20° each. The rotations for the 18 wind direction sectors are used to correct further measurement data for the wind tilt and possible tilt of the sonic anemometer.

The measurement setup is described in Paragraph 3.1. Wind coming from the (north)west is distorted at 60 m, 100 m and 180 m height due to the presence of the big tower, which results in the anomalous dips near a wind direction of 290° that are visible in Figure E.1. To check whether the sonic anemometers are aligned with a fixed angle with respect to the earth's surface, spirit levels are placed at the anemometers at 3 m, 60 m and 180 m height. Measurements at these spirit levels are shown in Appendix D.

Table E.1: The wind tilt corrections at 3 m height as calculated by Bosveld (2008). Each data point contains measurement data averaged over 10 minutes. Data points are selected for calculations if the horizontal wind velocity is higher than 3 m s^{-1}. After initial rotation calculations, the outliers of the data points are deleted. The remaining data points are the cleaned data points. With these cleaned data points, the rotation for wind tilt correction is calculated.

Wind direction	Selected data points	Cleaned data points	Rotation [rad]	Rotation [°]
0° - 20°	681	665	0.01053	0.6033
20° - 40°	456	444	0.00818	0.4687
40° - 60°	395	382	0.00328	0.1879
60° - 80°	1281	1241	0.00229	0.1312
80° - 100°	945	907	0.00288	0.1650
100° - 120°	1036	1011	0.00394	0.2257
120° - 140°	540	523	0.00041	0.0235
140° - 160°	553	524	0.00060	0.0344
160° - 180°	1343	1253	0.00465	0.2664
180° - 200°	3047	2878	0.00767	0.4395
200° - 220°	3577	3457	0.01290	0.7391
220° - 240°	3563	3457	0.01679	0.9620
240° - 260°	2405	2325	0.01637	0.9379
260° - 280°	1710	1657	0.01822	1.0439
280° - 300°	1049	1007	0.02262	1.2960
300° - 320°	1253	1183	0.02125	1.2175
320° - 340°	1078	1054	0.01919	1.0995
340° - 360°	760	744	0.01732	0.9924
All	25672	25233	0.01294	0.7414

Table E.2: The wind tilt corrections at 60 m height as calculated by Bosveld (2008). Each data point contains measurement data averaged over 10 minutes. Data points are selected for calculations if the horizontal wind velocity is higher than 3 m s^{-1}. After initial rotation calculations, the outliers of the data points are deleted. The remaining data points are the cleaned data points. With these cleaned data points, the rotation for wind tilt correction is calculated.

Wind direction	Selected data points	Cleaned data points	Rotation [rad]	Rotation [°]
0° - 20°	1690	1583	0.03605	2.0655
20° - 40°	1573	1485	0.02688	1.5401
40° - 60°	1741	1604	0.02693	1.5430
60° - 80°	2946	2788	0.01705	0.9769
80° - 100°	2478	2279	0.00694	0.3976
100° - 120°	1836	1723	0.00407	0.2332

Wind tilt corrections at 60 m height. Continued from previous page

Wind direction	Selected data points	Cleaned data points	Rotation [rad]	Rotation [°]
120° - 140°	1112	1052	0.00352	0.2017
140° - 160°	1249	1215	0.00399	0.2286
160° - 180°	1915	1776	0.00287	0.1644
180° - 200°	3625	3375	-0.00196	-0.1123
200° - 220°	5175	4896	-0.00402	-0.2303
220° - 240°	5251	4996	-0.00027	-0.0155
240° - 260°	3403	3206	0.00671	0.3845
260° - 280°	2721	2531	-0.00085	-0.0487
280° - 300°	1883	1857	-0.02694	-1.5435
300° - 320°	1503	1475	0.00181	0.1037
320° - 340°	2185	2067	0.01844	1.0565
340° - 360°	1657	1542	0.03352	1.9206
All	43943	42997	0.00467	0.2676

Table E.3: The wind tilt corrections at 100 m height as calculated by Bosveld (2008). Each data point contains measurement data averaged over 10 minutes. Data points are selected for calculations if the horizontal wind velocity is higher than 3 m s^{-1}. After initial rotation calculations, the outliers of the data points are deleted. The remaining data points are the cleaned data points. With these cleaned data points, the rotation for wind tilt correction is calculated.

| Wind direction	Selected data points	Cleaned data points	Rotation [rad]	Rotation [°]
0° - 20°	1698	1493	-0.00212	-0.1215
20° - 40°	1618	1418	-0.00780	-0.4469
40° - 60°	1645	1498	-0.02156	-1.2353
60° - 80°	2818	2690	-0.02632	-1.5080
80° - 100°	2895	2662	-0.03090	-1.7704
100° - 120°	1828	1683	-0.03483	-1.9956
120° - 140°	1225	1154	-0.02841	-1.6278
140° - 160°	1195	1169	-0.00370	-0.2120
160° - 180°	1853	1805	0.00900	0.5157
180° - 200°	3504	3436	0.02813	1.6117
200° - 220°	5490	5150	0.03286	1.8827
220° - 240°	5677	5274	0.03954	2.2655
240° - 260°	4084	3792	0.03672	2.1039
260° - 280°	2962	2780	0.03641	2.0861

Wind tilt corrections at 100 m height. Continued from previous page

Wind direction	Selected data points	Cleaned data points	Rotation [rad]	Rotation [°]
280° - 300°	2193	2166	0.00979	0.5609
300° - 320°	1740	1730	0.01702	0.9752
320° - 340°	2337	2102	0.01830	1.0485
340° - 360°	1994	1812	0.01461	0.8371
All	46706	46593	0.01964	1.1253

Table E.4: The wind tilt corrections at 180 m height as calculated by Bosveld (2008). Each data point contains measurement data averaged over 10 minutes. Data points are selected for calculations if the horizontal wind velocity is higher than $3 \, \text{m s}^{-1}$. After initial rotation calculations, the outliers of the data points are deleted. The remaining data points are the cleaned data points. With these cleaned data points, the rotation for wind tilt correction is calculated.

Wind direction	Selected data points	Cleaned data points	Rotation [rad]	Rotation [°]
0° - 20°	1677	1445	0.04557	2.6110
20° - 40°	1707	1590	0.03676	2.1062
40° - 60°	1503	1371	0.02714	1.5550
60° - 80°	2829	2575	0.02043	1.1706
80° - 100°	2936	2659	0.01272	0.7288
100° - 120°	1875	1539	0.00807	0.4624
120° - 140°	1131	1037	0.00800	0.4584
140° - 160°	1077	1031	0.00705	0.4039
160° - 180°	1552	1475	0.00836	0.4790
180° - 200°	2462	2256	0.00459	0.2630
200° - 220°	5297	4952	0.00497	0.2848
220° - 240°	6126	5796	0.00746	0.4274
240° - 260°	4231	4018	0.01152	0.6600
260° - 280°	2947	2798	0.00282	0.1616
280° - 300°	2035	1984	-0.03334	-1.9102
300° - 320°	1790	1768	-0.00159	-0.0911
320° - 340°	2230	2087	0.02429	1.3917
340° - 360°	2184	2016	0.03984	2.2827
All	45589	44358	0.01085	0.6217
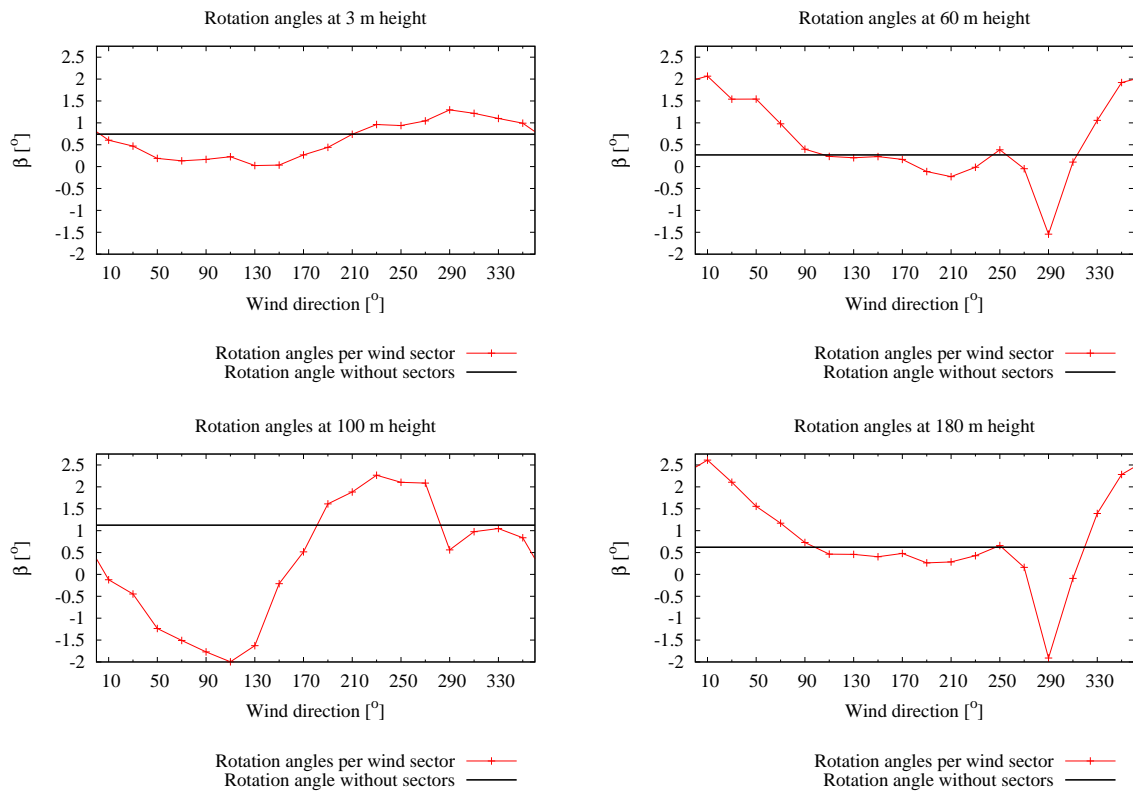
Figure E.1: In these graphs, the rotation angles for the wind tilt corrections are plotted for all heights. The data is given in Tables E.1, E.2, E.3 and E.4 and originates from Bosveld (2008) of the KNMI. It is visible that at 60 m, 100 m and 180 m height, the rotation angles have a dip near a wind direction of 290°. This is caused by the fact that the tall measurement tower stands north west in comparison to the anemometers. The wind coming from that direction is distorted because of this.